

©Copyright 2024

Greta E. M. Shum

Last Updated 2024-04-22.

Adventures in Wonder of Land:
How Biophysical and Biogeochemical Responses between Land and
Climate Determine Habitability in Two Extreme Worlds

Greta E. M. Shum

A dissertation
submitted in partial fulfillment of the
requirements for the degree of

Doctor of Philosophy

University of Washington

2024

Reading Committee:

Abigail L. S. Swann, Chair

Cecilia M. Bitz

Dargan M. W. Frierson

Program Authorized to Offer Degree:
UW Atmospheric Sciences

University of Washington

Abstract

Adventures in Wonder of Land:
How Biophysical and Biogeochemical Responses between Land and Climate Determine
Habitability in Two Extreme Worlds

Greta E. M. Shum

Chair of the Supervisory Committee:
Dr. Abigail L. S. Swann
Departments of Atmospheric Sciences & Biology

Properties and processes that regulate the exchange of water, energy, and carbon dioxide between the atmosphere, land, and ocean, have a strong influence on Earth's overall climate state. As a result, the assumptions made that influence the coupling between the atmosphere and land/ocean play an important role in determining Earth's climate stability. In two very different climate settings, we examine the choices we make about properties at the interface that influence the coupling between those two systems, and how they influence the habitability of those climates.

These "surface-level" choices may not seem dramatic compared to the direct influence of other model choices, such as radiative properties of the atmosphere, but their ability to engage multiple systems (land, atmosphere, and ocean) acts to compound the influence of any change.

In this dissertation, we use habitability as a temperature threshold specific to each climate setting. The concept of habitability can be thought of as an application of climate sensitivity, and allows us to connect two very different climate states through their relevance to other disciplines.

In Chapter 2, we examine the influence of land surface albedo on habitability as it concerns eukaryotic, photosynthetic algae. We find that by regulating the flux of energy to the Earth system and critically by extension regulating the potential flux of water to

the atmosphere, bare land surface albedo exerts a stronger control on habitability of likely refugia than the radiative influence of CO₂ concentration. In Chapters 3 and 4, we directly investigate how the cycling of carbon between atmosphere, land, and ocean, as determined explicitly by carbon cycle model structure and implicit assumptions about how carbon is fluxed between carbon pools, influences the habitability of future Earth for human populations. We find that differences in model structure lead to persistent differences in the long-term climate state given the same decarbonization scenario. These differences stem from differences in carbon sink rates, or how carbon moves across Earth systems in a coupled model configuration.

Quantifying the sensitivity Earth's climate to assumptions about properties and processes of Earth system coupling, especially in domains that are relevant in adjacent disciplines (applications for astrobiology and climate policy) yields important takeaways for the state of our understanding of those processes, leading to opportunities for future research.

TABLE OF CONTENTS

	Page
List of Figures	iii
List of Tables	vi
Chapter 1: Introduction	1
1.1 Climate models as tools and methodologies	1
1.2 Habitability as a theme and a metric	2
1.3 Influence of biogeophysical coupling on habitability of Snowball Earth	3
1.4 Influence of biogeochemical coupling on future habitability with decarbonization	4
Chapter 2: Ocean bays surrounded by desert land could support photosynthetic life on Snowball Earth	6
2.1 Introduction	7
2.2 Investigation of the narrow bay refugium	10
2.3 Methods	14
2.4 Results	20
2.5 Discussion and conclusion	26
Chapter 3: The Identifying the Influence of Carbon Cycle Representation on Sink Sensitivity, Total Warming, and Global Carbon Budgets in Simple Climate Models	29
3.1 Introduction	29
3.2 Methods	34
3.3 Results	40
3.4 Discussion & Conclusions	51
Chapter 4: Characterizing Carbon Sink Responses to Decarbonization across Model Structures	54
4.1 Motivation and Introduction	54
4.2 Research Questions	56

4.3	Methods	57
4.4	Results	65
4.5	Conclusion	78
4.6	Discussion	78
	Chapter 5: Conclusions and Future Work	83
	Appendix A: Penetration of a sea glacier down a narrow bay	84

LIST OF FIGURES

Figure Number	Page
2.1 Spectral albedos of representative surface types. Cold fine-grained snow was measured at Dome C on the East Antarctic Plateau (Figure 6 of Hudson et al., 2006). Firn was measured just upstream of the Allan Hills blue-ice field in East Antarctica (Site R9 of Dadic et al., 2013). Glacier ice is from the Allan Hills blue-ice field (Site R1 of Dadic et al., 2013). These firn and ice sites can represent sea-glacier surfaces on Snowball Earth because they were originally formed by snow accumulation and exposed by sublimation, never having experienced melting. The "polar desert" site is an unvegetated surface of soil and stones in northeast Greenland (photograph shown in Figure 6 of Bøggild et al., 2010). For the "polar desert" surface, albedo measurements were not possible from 1.35 to 1.45 μm , and from 1.75 to 2.05 μm , because the incident solar radiation flux was near zero at these wavelengths due to atmospheric water-vapor absorption; the dashed lines interpolate across these regions.	12
2.2 Habitability of the simulated snowball climate. (a, b, c) Surface temperature of the warmest month in the coldest simulated case (10 ppm CO ₂ , bare-land albedo 0.4), the midpoint simulation (50 ppm CO ₂ , bare-land albedo 0.3) and the warmest case (200 ppm CO ₂ , bare-land albedo 0.1), respectively. Red areas indicate locations with seasonal melting, suggesting the possibility of ice-surface refugia. (d, e, f) Annual minimum snow depth (monthly mean) from the same cases, given as mm snow water equivalent (SWE), which is equivalent to kg/m ² . Brown areas indicate places where snow depth drops below the threshold for surface-albedo change at some point during the year. Note that ocean areas without snow accumulation would nonetheless be covered by sea glaciers. (g, h, i) Annual mean potential evaporation (PE) minus precipitation (P) for the same cases.	21
2.3 (a) Area of land (per 1.9 degrees of latitude increment) with temperature above freezing in the warmest month. Total land area is shown in grey. (b) Change in percent land area above freezing in the warmest month, per unit radiative forcing, relative to the coldest case (10 ppm CO ₂ , albedo 0.4).	23

2.4 Percent of land area capable of hosting refugia, were an arm of the sea to reach it, for several combinations of CO ₂ mixing ratio and bare-land albedo. Relative to the coldest case (albedo=0.4 and CO ₂ =10 ppm), the change in suitable land area is shown as a function of the radiative forcing, caused either by darkening the surface or by increasing CO ₂ . (a) Percent of land area with temperature of the warmest month $T_{max} > -2^{\circ}\text{C}$. (b) Percent of land area with mean annual PE _i P. (c) Percent of land area with $T_{max} > -2^{\circ}\text{C}$ and PE>P. (d) Percent of <i>ocean</i> area with temperature of the warmest month $T_{max} > -2^{\circ}\text{C}$. (e) Percent of land area with temperature of the warmest month $T_{max} > -2^{\circ}\text{C}$ relative to the warmest case (albedo=0.2 and CO ₂ =200 ppm).	25
3.1 Carbon cycle structures for each SCM. In each schematic, a pink horizontal rectangles at the top represents the SCM's atmosphere carbon pool. HECTOR, Swann/Deutsch and MAGICC represent land and ocean carbon cycles separately and explicitly and have been colored green and blue to indicate terrestrial and ocean carbon representations, respectively. HECTOR and Swann/Deutch contain representations of ocean circulation, which influences carbon draw-down from the atmosphere to the ocean.	35
3.2 Emissions scenarios	39
3.3 Historical CO ₂ concentration for all models.	42
3.4 GCP to net-zero	43
3.5 500 PgC Pulse CO ₂ and temperature	45
3.6 ESM Bell [CO ₂] and temperature	46
3.7 Flat10-ZEC [CO ₂] and global temperature anomaly.	47
3.8 Flat10 ZEC TCRe and ZEC50 for all models and ESMs.	49
3.9 Flat10-ZEC [CO ₂] and global temperature anomaly.	49
3.10 Flat10-ZEC Carbon pools. For FaIR_SD (green), HECTOR (blue), and MAGICC (purple), time evolution of carbon pools for the flat10_zec experiment. Solid lines in the ocean pools indicate the sum of the non-surface pools, while the dashed lines represent the total ocean pool size. MAGICC's total ocean carbon is plotted as the purple dash-dot line.	50
4.1 Parameters vs. CO ₂ , GR, and T (TK: will replace with wider beta range, higher figsize and resolution)	59
4.2 FaIR and FaIR_SD CO ₂ , GR, and T as constraints	60
4.3 GCP Historical CO ₂ concentration as a constraint for FaIR, FaIR_SD and HECTOR	62
4.4 GCP Historical CO ₂ growth rate as a constraint for FaIR, FaIR_SD and HECTOR	62

4.5	GCP Historical temperature change as a constraint for FaIR, FaIR_SD and HECTOR	63
4.6	Flat10 CO ₂ and T for FaIR & ZEC. (TK: add HECTOR)	64
4.7	GCB Historical carbon fluxes	66
4.8	Distributions of Flat10_ZEC TCRe1000 for FaIR, FaIR_SD, HECTOR	67
4.9	Histogram of ZEC20, ZEC50, ZEC100 for all FaIR, FaIR_SD, HECTOR	68
4.10	Flat10_ZEC carbon fluxes of sink and atmosphere pools for 100 ensemble members constrained by CO ₂	70
4.11	FaIR_SD Land C Fluxes, Single Exponential fit using emissions and land sink response over 100 years of emissions	71
4.12	FaIR_SD Land C Fluxes, Single Exponential fit using emissions and land sink response over entire simulation time period	72
4.13	FaIR_SD Land C Fluxes, Double Exponential fit using emissions and land sink response over entire simulation time period	72
4.14	FaIR_SD Ocean C Fluxes, Single Exponential fit using emissions and ocean sink response over 100 years of emissions	73
4.15	FaIR_SD Ocean C Fluxes, Single Exponential fit using emissions and ocean sink response over entire simulation time period	73
4.16	FaIR_SD Ocean C Fluxes, Single Exponential fit using emissions and ocean sink response over entire simulation time period	74
4.17	FaIR_SD Total Sink C Fluxes, Single Exponential fit using emissions and sink response over 100 years of emissions	74
4.18	FaIR_SD Total Sink C Fluxes, Single Exponential fit using emissions and sink response over entire simulation time period	75
4.19	FaIR_SD Total Sink C Fluxes, Double Exponential fit using emissions and sink response over 100 years of emissions	75
4.20	FaIR_SD Total Sink C Fluxes, Double Exponential fit using emissions and sink response over entire simulation time period	76
4.21	Distribution of timescales in single exponential curves.	79
4.22	Distribution of timescales in double exponential curves.	80
4.23	Distribution of timescales in triple exponential curves.	81
4.24	Carbon budgets using different constraints for FaIR_SD	82

LIST OF TABLES

Table Number	Page
2.1 Band-albedos of representative snow, ice, and land surfaces. The spectral albedos for four of these surface types are shown in Figure 3.1.	13
2.2 Characteristics of the model runs. The consequences of radiative forcing shown for combinations of changes to the bare-land albedo and the CO ₂ level are relative to the coldest case of CO ₂ = 10 ppm and bare-land albedo = 0.4 broadband (0.3 visible / 0.5 near-IR). Land is “net-evaporative” if potential evaporation (PE) exceeds precipitation (P).	18
3.1 Carbon Cycle Approach by Model	34
4.1 FaIR_SD timescales for each memory function and sink. These are calculated from the to 100 ensemble members constrained from CO ₂	76
4.2 FaIR_SD timescales for each memory function and sink. These are calculated from the to 100 ensemble members constrained from CO ₂	77

ACKNOWLEDGMENTS

Acknowledgments TK.

DEDICATION

To my parents.

Chapter 1

INTRODUCTION

1.1 Climate models as tools and methodologies

Global climate models are critical class of tools for exploring unobservable climate states, including paleoclimate and future climate, based on our knowledge of the Earth system. By modeling these unobservable states, we can also identify fundamental behaviors of the Earth system. This effort allows us to demarcate the limits of our knowledge of the Earth system by identifying which elements of the observable Earth system exert the strongest influence over the predictability of key climate metrics, such as habitability. We can gain insight not only from identifying those elements and describing how further observations of those elements could increase our total understanding but also by building an awareness of how our characterization of the Earth system functionality in models reflects how we interact and ultimately interact with the climate system. This can be done by using different kinds of models or different configurations in our simulations of different climate settings to identify which aspects of the Earth system (and their connections) have the greatest impact.

In this dissertation, I examine habitability as the climate state of interest, and define two thresholds of habitability, one for past climate and one for future climate. The first has a direct implications for understanding the history of life on Earth as well as understanding the possibility of Earth-like life elsewhere in the universe, and the second has direct immediate implications for human decisions in response to anthropogenic climate change. Both studies reveal limitations in our knowledge of the *observable* world, which, if pursued, would close the gap in what we can and cannot say about these unobservable worlds. In short, the dialectic of models and observations can be used to build knowledge about climates removed by time and space.

In both of our climate settings, Snowball Earth and future climate, the behavior of processes at the interface between Earth systems – atmosphere, ocean, and land – that is,

processes at the surface, where water, energy, and carbon are exchanged and where biogeochemical and biophysical feedbacks take place, exert a strong influence on their habitability. This “surface-level” weakness may reflect real-world obstacles that disciplinary boundaries impose as well as the potential leaps that intentionally cross-disciplinary research projects promise.

1.2 Habitability as a theme and a metric

In the context of Snowball Earth, we ask whether early photosynthetic life could survive on the surface and what influences the answer the most. Our definition of habitability is based on known characteristics of life on Earth and partially motivated by the search for life on other planets, which requires liquid water to be present and on the surface (since any potential of life could only be made at the surface). Since evidence exists of surface-dwelling photosynthetic, eukaryotic algae prior to Snowball Earth, the mystery arises: how could life have survived a period when global mean surface temperature was significantly below zero, and what is the mechanism by which local temperature could have exceeded this threshold.

In the context of future climate, we can define habitability of the Earth system through the lens of the risks to global ecosystems and human health and well-being that anthropogenic climate change poses. In its Special Report on Global Warming of 1.5°C, the IPCC found that limiting global warming to below 1.5°C above pre-Industrial levels is critical because of the risks this level of warming poses to a host of natural and human systems including species disruption and loss in terrestrial, wetland, and ocean ecosystems, as well as loss of the environmental services those systems provide, extreme weather risk such as drought, extreme precipitation, and extreme heat, increased vulnerability food insecurity, vector-borne diseases, poverty, and climate-driven displacement due to sea level rise and other climate change-driven impacts (Hoegh-Guldberg et al., 2018).

While in each climate setting we define habitability differently, in both cases, “habitability” serves as we way to apply our understanding of the Earth system to wider disciplinary question. In the case of Snowball Earth, understanding the habitability of the Snowball Earth climate not only expands our understanding of life on Earth, but it also allows us to expand our definition of habitability for exoplanets. In the case of future climate, un-

derstanding which processes determine total warming from anthropogenic climate change allow us to set informed mitigation targets.

1.3 Influence of biogeophysical coupling on habitability of Snowball Earth

The biogeophysical coupling between land and climate can cause changes in land properties such as surface albedo, evaporative resistance, surface roughness and other aspects of modern vegetation that influence water and energy fluxes, to be affected by and influence climate Laguë et al. (2019); Bonan (2015). The importance of interactivity between surface properties has been shown in simple conceptual models such as Daisyworld (Watson and Lovelock, 1983), which was used to demonstrate the plausibility of the Gaia Hypothesis (Lovelock, 1986; Wood et al., 2008). The importance of biogeophysical feedbacks has also been shown in global climate models: coupling a land surface model with an interactive atmosphere yields larger temperature changes in response to changes in land surface properties, as well as different patterns in the climate response, than the same change in an uncoupled configuration, in which feedbacks are suppressed (Laguë et al., 2019). Boreal ecosystems in particular exhibit sensitivities to this coupling because of differences between the boreal forest and tundra in surface albedo, surface roughness (which alters the effect of snow), and the partitioning of energy between latent and sensible heat. For this reason, the spatial distribution of boreal forest is an important regulator of global climate (Bonan et al., 1995; Swann et al., 2010). In Master's work, I showed that biogeophysical feedbacks in the boreal region can alter habitats and ecosystems over time by modeling the emergence of a new biome can influence neighboring ecosystems through their influence on regional climate (Shum et al., 2023). As a result, while they are a challenge to characterize given the uncertainty of past land surface types, biophysical feedbacks are key to include when assessing local climate in a paleoclimate context.

Models like CESM offer exciting opportunities to study worlds that would be greatly influenced by the inclusion of biogeophysical coupling between land and atmosphere, such as Snowball Earth. As in the modern boreal region, the contrast between snow-covered and snow-free land is stark.

In Chapter 2, we use an idealized land surface model called the Simple Land Interface

Model (SLIM) (Laguë et al., 2019), which allows us to test the influence of land surface albedo on habitability. Using SLIM allows us to modify properties of the land surface in isolation, whereas modifying a land cover type in a more realistic land model might change two properties at the same time. By modifying land surface albedo in isolation, we can attribute any changes in climate directly to the radiative changes and accompanying biogeophysical feedbacks it kicks off.

Moreover, modeling Snowball Earth habitability not only adds context to early life on Earth, but also enhances our understanding of exoplanet habitability. In this context, habitability can be defined as hosting liquid water on the surface. In the case of the TRAPPIST-1 system for example, which is composed of a cool red dwarf star hosting seven approximately Earth-sized and Earth-density planets (Agol et al., 2021). Several of planets lie within or just outside of the habitable zone; TRAPPIST-1e in particular has the strongest likelihood of hosting liquid water despite having a equilibrium temperature several degrees below Earth's. Due to a lack of knowledge of their surface, modeling studies that have been conducted to assess the TRAPPIST planets' habitability use exclusively aquaplanet climates and are unable to include any representations of land or land-atmosphere feedbacks (Wolf, 2017; Sergeev et al., 2022). While the changes we make through atmospheric CO² and bare land albedo do not drastically shift global mean surface temperature, they do alter local climate in ways that could drastically shift habitability of the planets, suggesting that even the planets with very cold global mean surface temperatures could possibly host life.

1.4 Influence of biogeochemical coupling on future habitability with decarbonization

TK: General introduction to **biogeochemical** response of land to climate, with implications for (1) what we predict about climate change and (2) what we predict about potential mitigation of climate change through uptake of carbon by natural and artificial land sink enhancement.

Motivate with general background on how biogeochemical feedback processes in ESMs are increasing in complexity while poorly constrained. (Essentially no carbon cycle PPEs, heavy implicit reliance on simple models of the carbon cycle).

Contrast accessibility of SCMs to ESMs, which elevates SCMs and intermediate-complexity models as tools for climate policy and as well as research direction scoping for ESMs and MIPs.

Chapter 2

OCEAN BAYS SURROUNDED BY DESERT LAND COULD SUPPORT PHOTOSYNTHETIC LIFE ON SNOWBALL EARTH

(This chapter has been submitted for publication to AGU Advances as Shum, G. E. M., M. M. Laguë, A. L. S. Swann, C. M. Bitz, E. D. Waddington, S. G. Warren (2024). Ocean bays surrounded by desert land could support life on Snowball Earth.)

Abstract

Photosynthetic eukaryotic algae survived the Neoproterozoic Snowball Earth events, indicating that liquid-water refugia existed somewhere on the surface. We examine the potential for refugia at the coldest time of a snowball event, before CO₂ had risen and with high-albedo ice on the frozen ocean, before it became darkened by dust deposition. We use the Community Earth System Model to simulate a “modern” Snowball Earth (i.e., with continents in their current configuration), in which the ocean surface has frozen to the equator as “sea glaciers”, hundreds of meters thick, flowing like ice shelves. Despite global mean surface temperatures below -60°C, some areas of the land surface reach above-freezing temperatures because they are darker than the ice-covered ocean. With low CO₂ (10 ppm) and land-surface albedo 0.4 (characteristic of bright sand-deserts), 0.1 percent of the land surface could host liquid water seasonally; this increases to 12 percent for darker land of albedo 0.2, characteristic of polar deserts. Narrow bays intruding from the ocean to these locations (such as the modern Red Sea) could provide a water source protected from sea-glacier invasion, where photosynthetic life could survive. The abundance of potential refugia increases more strongly in response to reducing the land albedo than to increasing the CO₂, for the same global radiative forcing.

2.1 Introduction

On Earth and Earth-like worlds, a large negative radiative forcing can initiate a positive ice-albedo feedback and ultimately lead to global glaciation (Budyko, 1969; Sellers, 1969). Geologic evidence indicates that the Earth has experienced several such events since the emergence of life (Harland, 1964; Kirschvink, 1992; Hoffman et al., 2017; Evans, 2000). These events were likely caused by a reduction of the atmospheric greenhouse effect, resulting from disturbance of the global carbon cycle (Hoffman et al., 2017). During the Neoproterozoic era (600-800 Ma), two “Snowball Earth” events occurred: the Sturtian, with a duration of 58 million years, and the Marinoan, with a duration of 10 million years (Macdonald et al., 2010). The oceans would likely have been covered by ice hundreds of meters thick, but photosynthetic eukaryotic algae were able to survive (Porter, 2004; Knoll, 2011, 2014), indicating that some liquid water was maintained at or near the surface where light was available for photosynthesis.

In this paper, we focus on the “hard” Snowball Earth, in which the equatorial ocean would be covered by thick ice. That ice differed in several ways from sea ice on the polar oceans of modern Earth. Modern sea-ice thickness is limited to a few meters by summertime melting and by a heat flux F_0 of several watts per square meter from the ocean water below, which originally gained its heat by absorption of solar energy at lower latitudes.

But at the onset of a snowball event, when sea ice reached the equator it would shut off solar heating of the ocean water below. After a few thousand years, the ocean would have lost its reservoir of heat, leaving only geothermal heat, $F_0 \approx 0.08 \text{ W m}^{-2}$ (about one-hundredth that of the modern oceanic flux F_0 to the ice bottom), increasing the equilibrium ice thickness from a few meters to a few hundred meters (Warren et al., 2002).

The geothermal flux is essentially independent of latitude, but the ice surface on the snowball ocean would be colder at high latitude than at low latitude, resulting in thicker ice at higher latitude. The latitudinal thickness gradient would cause the ice to flow (Goodman and Pierrehumbert, 2003). In this state, the thick ice on the frozen ocean would be growing from above by snowfall (the original sea ice having melted off the bottom), and therefore can be classified as glacier ice rather than sea ice. This ice, flowing like the modern Antarctic ice

shelves but not dependent on continental glaciation, is called a sea glacier (Warren et al., 2002). Sea glaciers are computed to flow as much as 7-50 meters per year even when they cover the entire ocean (Goodman, 2006; Li and Pierrehumbert, 2011). If a small area of the ocean were to open up, it would be quickly filled by inflow of the sea glacier. How, then, could liquid water be maintained at the surface? Several hypotheses for refugia have been proposed, which we now list.

2.1.1 Types of proposed refugia

Five ideas have been proposed for liquid-water refugia at the ocean surface.

- (a) **Hotspots.** Hoffman and Schrag (2000, 2002) noted that geological hotspots at the ocean floor under shallow water, as occur near the coasts of Hawaii and Iceland, would melt inflowing ice fast enough to maintain pools of liquid seawater. These pools would be small in area, and would not be stable for millions of years, so any life would have to survive many long and deep migrations.
- (b) **Thin ice.** McKay (2000), using a broadband model for solar radiation, proposed that absorption of sunlight within the ice might be able to limit the tropical ice thickness to 10 m. Warren et al. (2002) pointed out that the visible and ultraviolet wavelengths, which penetrate deeply, are not absorbed but eventually are scattered back out to space, whereas the near-infrared wavelengths, which are indeed absorbed, are absorbed in the top few millimeters, so their heat is easily conducted up to the atmosphere. By modifying McKay's model to compute the radiation spectrally, Warren et al. found that the equilibrium ice thickness in a typical example grew from 1 m to 800 m. McKay joined as a coauthor on that paper, agreeing that the thin-ice solution was not viable. Pollard and Kasting (2005) tried to find a thin-ice solution that would even hold off sea glaciers, and succeeded only when three parameters were pushed beyond their acceptable limits (Warren and Brandt, 2006). An improved model (Pollard et al., 2017) convincingly rejected the thin-ice solution.
- (c) **Waterbelt.** Some models of snowball initiation have found that sea ice could reach

the outer tropics but still leave a wide belt of open water centered on the equator, spanning tens of degrees of latitude and circling the globe, if the sea-ice (or sea-glacier) albedo is low enough. Abbot, Voigt, and Koll (2011) found that this “waterbelt” state could exist with sea-glacier albedo of 0.45 but is inaccessible for sea-glacier albedo > 0.55 . Dadic et al.’s (2013) measurements of modern surrogates for sea-glacier surfaces found albedos 0.57 – 0.80 under clear sky, and even higher under cloudy sky, arguing against the waterbelt idea. A follow-on investigation by Voigt’s group (Braun et al., 2022) found the waterbelt to be unviable, even with sea-glacier albedo as low as 0.45. Most recently, Hörner and Voigt (2023) showed that the waterbelt in earlier models resulted from inadequate vertical resolution in the sea ice.

- (d) **Ice surface.** Vincent and Howard-Williams (2000) and Vincent et al. (2000) suggested that microbial life could survive on the ice surface of Snowball Earth, pointing to the widespread microbial communities that thrive both in surface meltwater pools and in brine pockets, on modern Arctic and Antarctic sea ice and ice shelves. These communities can persist even if only a few days per year have temperatures above freezing. Such communities could indeed have been active during the rapid advance of sea ice at the onset of Snowball Earth. But after the ice reaches the equator, the strong positive albedo-temperature feedback causes dramatic cooling. An early general circulation model (GCM) of the hard snowball by Pollard and Kasting (2004) obtained a global average surface temperature of -49°C . The warmest temperature on the ocean surface was found on a summer afternoon in the subtropics, $\sim -30^{\circ}\text{C}$, which seemed to rule out any surface life. However, we will see below that Vincent’s proposal can be resurrected if it is considered in combination with the next proposed refugium *e*.

- (e) **Narrow bay.** One place where ocean water could be safe from sea-glacier inflow is at the innermost end of a narrow bay resulting from continental rifting, like the modern Red Sea. When flowing into a narrow bay, nearly enclosed by dry land, ice flow can be slowed by resistive shear stresses from the side-walls, and by obstacles such as

islands, shoals, or narrows in the bay. If the bay is long enough and the sublimation rate is high enough, the ice thickness can taper down to zero before the end of the bay is reached (Campbell et al., 2011, 2014). To illuminate these concepts, in the Appendix we derive a characteristic penetration distance based on a simplified sea glacier in a simplified bay, in the absence of geometric complexities. If ocean-sourced water flowing under the ice can find its way to the end of the narrow bay, it could provide a refugium safe from sea glaciers. If the surrounding land is net-evaporative (i.e., potential sublimation outpaces precipitation, as in deserts), this place would be safe from land glaciers as well.

Refugia in narrow bays would be larger than the isolated geothermal hotspots around volcanic islands, and would have long lifetimes, similar to timescales of continental drift. But even if the end of the bay is safe from sea-glacier inflow, there is the risk that the climate might still be so cold that thick sea ice would grow locally. Such a refugium would be feasible only if local temperatures reach above freezing, which could occur because the albedo of nearby bare land surfaces would be lower than that of the ice-covered ocean. Land surfaces during the Snowball Earth events were not vegetated: possible snow-free surfaces would be bare rock, bare soil, and sand. Most of them are brighter than vegetated land, but with albedos 0.1-0.4 they are much darker than ice or snow. To evaluate the feasibility of this refugium, climate modeling is needed, and that is the subject of this paper.

2.2 *Investigation of the narrow bay refugium*

Given the high uncertainty of Neoproterozoic paleocontinental reconstructions, for this investigation we apply an earth-system model to the modern continental configuration. This approach has been used in prior investigations, called “modern Snowball Earth” (Voigt and Marotzke, 2010; Liu et al., 2018). It has the advantage of familiar geography, allowing comparisons of atmospheric circulation and climate with the familiar regional climates of the present. We take the modern continental configuration as a representative arrangement of continents of various size and shape, scattered across a range of latitudes.

As potential refugia, in addition to nearly-enclosed seas such as the Red Sea and Mediterranean, we also seek locations on land where the local temperature exceeds the freezing point of seawater at least once during the year; i.e. $T_{\max} > -2^{\circ}\text{C}$. With the right coastline geometry in a paleocontinental configuration (to allow for ocean-water access), these locations would be potential oases for photosynthetic eukaryotes.

Continental positioning itself is uncertain, and coastline geometry of the Neoproterozoic is even more uncertain. The period was tectonically active, and thus we make an explicit assumption that narrow bays are likely to have occurred and therefore seasonally above-freezing temperatures on land in our “modern Snowball Earth” allow for potential refugia even if these areas are not currently near a modern narrow bay. Additionally, many narrow bays would be smaller than the resolution of a typical global Earth System Model; thus, we focus on land surface temperatures as an indicator of possible refugia. To investigate whether life could survive the harshest conditions of the Snowball climate, in this paper we test the hypothesis that above-freezing land temperatures can exist in an Earth System Model in the “hard” Snowball Earth limit, in which even the tropical oceans are covered by ice hundreds of meters thick (no waterbelt).

The name “snowball” is somewhat misleading, in that the ocean was not entirely snow-covered. On the modern Earth, evaporation (E) exceeds precipitation (P) over nearly half the ocean, mostly in the subtropics. A large region of negative P E would also have existed on the Snowball Earth, according to general circulation models, although the hydrological cycle was probably weakened by a factor of ~ 30 (Pollard and Kasting, 2004). At high and middle latitudes the sea glaciers would have been covered by thick snow. But as sea glaciers flowed equatorward into the tropical region of net sublimation, their surface snow (albedo ~ 0.8) would sublimate away, exposing old snow (“firn”, albedo ~ 0.7). Then the firn would likewise sublimate away, exposing bare glacier ice (albedo ~ 0.6) to the atmosphere and to solar radiation. These albedos were measured on modern surrogates in the Allan Hills of East Antarctica: firn and glacier ice exposed by sublimation, which have never experienced melting (Figure 3.1 and Table 2.1) (Dadic et al., 2013).

In our modeling we do not attempt to simulate the regional evolution of ocean surfaces from snow, through firn, to glacier ice, as the sea glaciers flow equatorward. Instead,

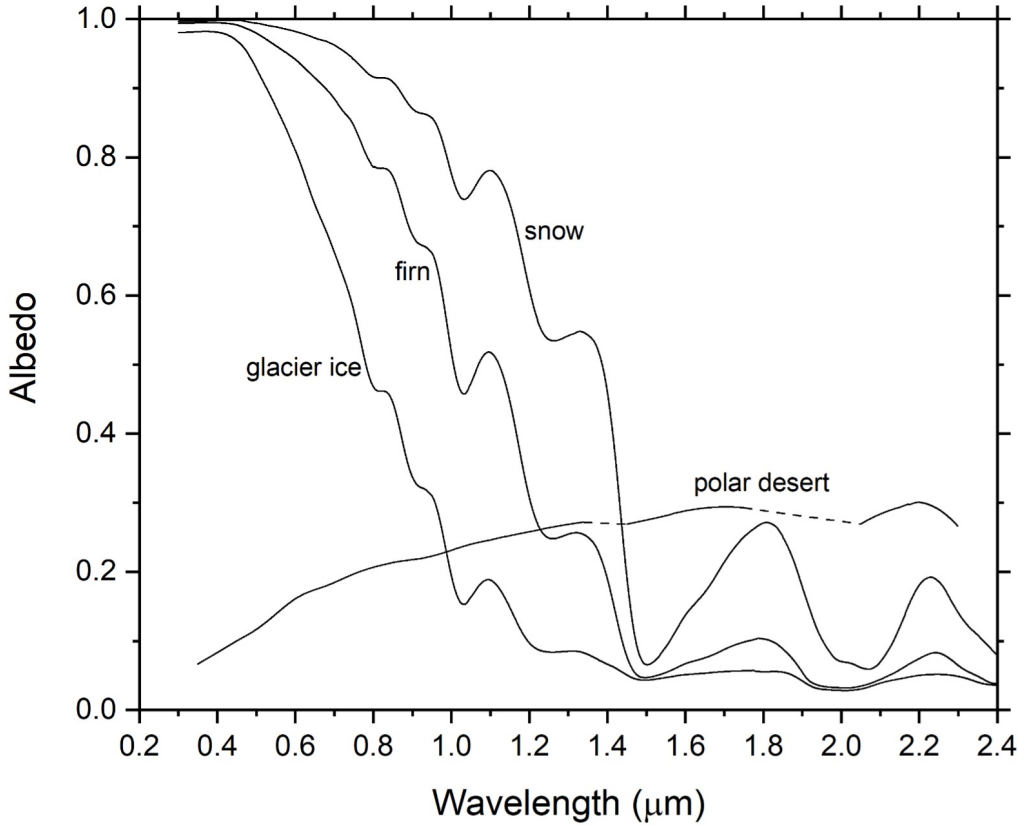


Figure 2.1: Spectral albedos of representative surface types. Cold fine-grained snow was measured at Dome C on the East Antarctic Plateau (Figure 6 of Hudson et al., 2006). Firn was measured just upstream of the Allan Hills blue-ice field in East Antarctica (Site R9 of Dadic et al., 2013). Glacier ice is from the Allan Hills blue-ice field (Site R1 of Dadic et al., 2013). These firn and ice sites can represent sea-glacier surfaces on Snowball Earth because they were originally formed by snow accumulation and exposed by sublimation, never having experienced melting. The "polar desert" site is an unvegetated surface of soil and stones in northeast Greenland (photograph shown in Figure 6 of Bøggild et al., 2010). For the "polar desert" surface, albedo measurements were not possible from 1.35 to 1.45 μm , and from 1.75 to 2.05 μm , because the incident solar radiation flux was near zero at these wavelengths due to atmospheric water-vapor absorption; the dashed lines interpolate across these regions.

Surface type	Albedo			Reference
	0.3-0.7 μm (UV, Visible)	0.7-3.0 μm (near-IR)	0.3-3.0 μm (total solar; broadband)	
Snow	0.98	0.68	0.83	Hudson et al. (2006), Grenfell et al. (1994)
Firn	0.94	0.44	0.69	Dadic et al. (2013)
Glacier ice	0.89	0.26	0.58	Dadic et al. (2013)
Polar desert (gravel and soil of northeast Greenland)	0.13	0.21	0.17	Bøggild et al. (2010)
Sand desert (Arabia)			0.40	Smith (1986)
Stony desert (Gobi)			0.10-0.15	Abell et al. (2020a,b)

Table 2.1: Band-albedos of representative snow, ice, and land surfaces. The spectral albedos for four of these surface types are shown in Figure 3.1.

everywhere that the ocean is not snow-covered, we assign its albedo to that of firn, thus biasing the global climate to a cold extreme and exaggerating the difficulty of maintaining refugia. We then investigate how the albedo of bare land surfaces, and the atmospheric CO₂ level, influence the potential habitability of a snowball climate. We test a range of CO₂ levels from 10 to 200 ppm and a range of uniform surface albedos for bare land from 0.2 to 0.4, using a climate model with the modern continental configuration.

During a snowball event, volcanic CO₂ accumulates in the atmosphere because its removal mechanisms (dissolving in rainwater and reacting with surface rocks) are suppressed. As the climate warmed with rising atmospheric CO₂ during the progression of a snowball event, refugia would have become more widespread. In addition, wind-erosion of bare land would have lifted dust that could accumulate on the ice, lowering its albedo, leading to additional potential mechanisms for refugia. Here we instead focus on the most extreme bottleneck of the cold early phase of a snowball event, the most critical time for survival of surface life.

2.3 Methods

2.3.1 Experimental Design

We use a modified version of the Community Earth System Model, version 2.1.0 (Danabasoglu et al., 2020), with the Simple Land Interface Model (SLIM) (Laguë et al., 2019) coupled to the Community Atmosphere Model, version 4 (CAM4) (Neale et al., 2010), the Los Alamos sea ice model CICE5 Hunke et al. (2015) in its thermodynamic-only mode (Bitz and Lipscomb, 1999), and a slab ocean model (SOM) (Bitz et al., 2012). Ocean heat flux convergence is set to zero everywhere, and sea surface temperatures are allowed to evolve. Simulations are run at a nominal 2° resolution.

SLIM is an idealized land model, designed for assessing the interactive roles of discrete land properties (e.g. bare-ground albedo, evaporative resistance, heat capacity of the soil, etc.); using it allows us to directly assess the climate response of specified land-surface albedos. Heat diffusion in the model is represented on a vertical soil grid that is separate from the water budget. Hydrology is represented using a simple bucket model that combines

a user-specified “lid” resistance with a resistance related to the fill level of the water bucket. Snow can accumulate on the surface, and can be removed by sublimation to the atmosphere or melting into the land. The model solves a linearized surface energy budget to calculate surface temperature, surface fluxes of radiation, turbulent heat fluxes, and ground heat storage.

When snow falls on the surface of land or sea ice, it masks the albedo of the underlying surface. On land, snow masks the albedo of bare ground when it exceeds a mass of 10 kg/m² liquid-equivalent (about 3 to 10 cm of snow, for typical snow densities 0.1-0.3 g cm⁻³). Land-surface models for the modern Earth normally use a larger snow-masking depth because of the presence of grass, bushes, and trees, but these plants did not appear until long after the Neoproterozoic snowball events.

In the midlatitudes and polar regions of a snowball climate, kilometer-thick ice sheets covering the oceans would accumulate, thicken, and flow like modern ice shelves towards thinner regions of net-sublimation as “sea glaciers” (Goodman and Pierrehumbert, 2003). It would therefore be glacier ice, not sea ice, that would cover the ocean surface in a snowball climate after the initial global freezing had taken place, and would have albedos ranging from that of snow in areas of snow accumulation to exposed firn and finally bare glacier ice in regions of net sublimation (Figure 3.1 and Table 2.1). Rather than predicting the detailed state of ice surface conditions, which is typical in CICE5, for simplicity we revert back to the CCSM3 shortwave radiative transfer formulation. This option allows us to prescribe “sea-ice” surface albedos. For bare (snow-free) ice we set visible and near-infrared band albedos to values appropriate for firn, so as to bias the global climate to its cold extreme. As snow accumulates, snow masks the bare ice, and the band albedos transition to values appropriate for snow (Table 2.1).

In all simulations, sea ice is initialized with 100% concentration and 20 m thick in all ocean gridcells. Sea ice rapidly grows thicker, but would take thousands of years to reach an equilibrium. We do not expect sea ice ever to reach an equilibrium thickness in our simulations even if we extended them, since geothermal heating is not represented; that heat source would be necessary to limit the freezing of seawater to the base of thick ice (McKay, 2000; Warren et al., 2002; Goodman and Pierrehumbert, 2003). Our surface

temperatures could be seen as too warm. For example, if the model ice thickness is only 50 m but in equilibrium would be > 500 m, there is an excessive conductive heat flux of 1.4 Wm^{-2} upward through the ice, causing the surface temperature to be too high by ~ 0.5 K.

Over Earth's history, the Sun has brightened by about 1% every 100 million years, so at 600 Ma the solar constant was $\sim 94\%$ of its present value (Crowley and Baum, 1993). That value, 94%, has been used to initiate the snowball state in models with Neoproterozoic continents clustered at low latitude. The low-latitude land facilitates snowball initiation in those models, because the albedo of bare land (0.2-0.4) exceeds that of open ocean (0.07). For a "modern" Snowball Earth, with most of the continental area at middle or high latitude, a lower solar constant, about 91%, is needed to initiate the snowball (Voigt and Marotzke, 2010), and that is the value we use for this work.

In models, the critical CO_2 level required for snowball onset depends on several modeling choices: sea-ice dynamics (Lewis and Eby, 2006; Voigt and Abbot, 2012), land topography (Liu et al., 2018), continental configuration (Liu et al., 2013), mountains (Walsh et al., 2019), atmospheric dust (Liu et al., 2020, 2021), and cloud radiative forcing (Voigt and Marotzke, 2010). In prior work, modeled snowball climates have been initiated at CO_2 mixing ratios as low as 2 ppm (Voigt and Abbot, 2012) and as high as 600 ppm (Liu et al., 2017) but generally fall between 50 and 300 ppm, with exact values dependent on the ice coverage on sea and land, the solar constant, and the land area (Schrug et al., 2002; Yang et al., 2012). For the coldest early stage of a snowball event, we therefore specify a variety of CO_2 levels, along with several choices for the albedo of snow-free land, and examine the resulting climatic patterns.

For initiation of the snowball state, we set the CO_2 mixing ratio to 100 ppm, and the albedo of snow-free land to a broadband value of 0.4. The albedo of bare land (rocks or soil) increases with wavelength across the solar spectrum from the ultraviolet (UV) to the infrared (IR) (Figure 3.1). We specify the albedo in two bands: 0.3 in the UV and visible (wavelengths 0.3-0.7 μm), and 0.5 in the near-IR (wavelengths 0.7-5.0 μm). Under these conditions, our initial simulation establishes the conditions necessary to maintain a frozen ocean in approximately 20 years. We run the initiation simulation for a total of 100 years to ensure that the frozen-ocean state is not transient, and that the atmosphere is in steady

state. Based on these conditions sufficient to generate a snowball climate, further runs are initialized with a fully ice-covered ocean to test the sensitivity of surface temperatures to variations in bare-land surface albedo and atmospheric CO₂ concentration (details below).

We run the model at the global scale and thus do not resolve the fine-scale dynamics of a sea glacier invading a bay. As described above, we assume that if a land gridcell experiences a monthly average surface temperature that exceeds the melting point, that gridcell could potentially support liquid water if a narrow arm of the sea were to reach it in a paleocontinental configuration, thus rendering it a potential refugium for photosynthetic life.

2.3.2 Sampling across a range of atmospheric CO₂ concentrations and land albedos

In the absence of land plants, which break up stones into sand or silt with higher albedo, the Neoproterozoic land surface was probably darker than modern deserts (the fossil record suggests that land plants did not evolve until 461–472 Ma (Kenrick et al., 2012; Morris et al., 2018)). The highest broadband albedo for modern deserts is 0.40 for the fine sand of the Arabian Empty Quarter (Smith, 1986); the lowest albedo is 0.10–0.15 for the stony desert of the western Gobi (Abell et al., 2020a; Figure S1 of Abell et al., 2020b). Within this range, we test five different sets of snow-free land albedo values, listed here from brightest to darkest as [UV-visible albedo/near-IR albedo]: 0.3/0.5, 0.25/0.45, 0.2/0.4, 0.15/0.35, and 0.1/0.3. Approximately half the solar energy is in the near-IR, so the total solar (broadband) albedo for each case is the average of the two values given; i.e., 0.40, 0.35, 0.30, 0.25, 0.20. As a shorthand to identify the cases, we simply give the broadband values.

We sample CO₂ levels of 10, 25, 50, 100, and 200 ppm. We do not test every combination of albedo and CO₂ values, but we do test the edge cases, as well as the full range of albedos for a 50 ppm CO₂ atmosphere, and the full range of CO₂ values for land albedo 0.3 (Table 2.2).

Albedo of bare (snow-free) land		CO ₂ (ppm)	Global average planetary albedo	Global mean surface tempera- ture (°C)	Radiative forcing (Wm ⁻²) relative to 10 ppm, albedo 0.4	Land area with $T_{\max} > -2^{\circ}\text{C}$ in warmest month (% of total)	Land area with PE>P in annual mean (% of total)	Land area with PE>P and $T_{\max} > -2^{\circ}\text{C}$ (% of total)	Ocean area with $T_{\max} > -2^{\circ}\text{C}$ in warmest month (% of total)
Broadband solar	Visible/ near-IR								
0.4	0.3/0.5	10	0.683	-69.2	0	0.1	50.8	0.1	0
0.4	0.3/0.5	50	0.681	-67.9	2.75	0.23	54.16	0.23	0.01
0.4	0.3/0.5	200	0.68	-66.5	5.16	0.54	59.83	0.54	0.04
0.35	0.25/0.45	50	0.675	-66.6	3.78	1.41	57.67	1.41	0.11
0.3	0.2/0.4	10	0.67	-66.7	2.05	3.1	56.77	3.1	0.24
0.3	0.2/0.4	25	0.669	-66.0	3.6	3.48	59.9	3.45	0.31
0.3	0.2/0.4	50	0.668	-65.3	4.8	4.04	63.14	4.04	0.36
0.3	0.2/0.4	100	0.667	-64.6	5.99	5.27	66.32	5.27	0.49
0.3	0.2/0.4	200	0.667	-63.9	7.21	5.72	70.4	5.7	0.40
0.25	0.15/0.35	50	0.662	-64.0	5.81	9.15	68.16	9.02	0.87
0.2	0.1/0.3	10	0.657	-64.2	4.06	12.15	67.87	12.02	1.17
0.2	0.1/0.3	50	0.655	-62.7	6.81	14.99	74.57	14.82	1.53
0.2	0.1/0.3	200	0.653	-61.2	9.22	17.22	85.03	17.05	1.83

Table 2.2: Characteristics of the model runs. The consequences of radiative forcing shown for combinations of changes to the bare-land albedo and the CO₂ level are relative to the coldest case of CO₂ = 10 ppm and bare-land albedo = 0.4 broadband (0.3 visible / 0.5 near-IR). Land is “net-evaporative” if potential evaporation (PE) exceeds precipitation (P).

We use the Parallel Offline Radiation Tool (PORT) (Conley et al., 2013) to calculate total global radiative forcing associated with each experiment relative to a base case in the middle range at $\text{CO}_2 = 50 \text{ ppm}$ and bare (snow-free) land albedo 0.3. [In Table 2.2 the radiative forcings are shown instead relative to the coldest case ($\text{CO}_2 = 10 \text{ ppm}$, albedo = 0.4) for ease of comparison.] Table 2.2 shows that dropping the albedo of bare land from the brightest case (0.4) to the darkest case (0.2) at 50 ppm causes a radiative forcing (RF) of 4.06 W m^{-2} , resulting in a 5.2 K increase in global mean surface temperature, implying a climate sensitivity of $1.28 \text{ K/(W m}^{-2}\text{)}$. Increasing CO_2 from 10 ppm to 200 ppm (with land albedo 0.3) causes $\text{RF} = 5.16 \text{ W m}^{-2}$, and results in a temperature increase of 2.8 K, implying a lower climate sensitivity of $0.54 \text{ K/(W m}^{-2}\text{)}$. These climate sensitivities may be compared to a median of $0.5 \text{ K/(W m}^{-2}\text{)}$ in 19 GCMs for the modern Earth (Cess et al., 1990).

These climate sensitivities indicate that albedo-driven forcing kicks off stronger feedbacks than CO_2 -driven forcing. The snowball climate has been shown to be relatively insensitive to CO_2 -driven forcing; at such low temperatures, the positive feedback from the water-vapor greenhouse effect is weak (Pierrehumbert, 2005). Outside of the tropics, the wintertime greenhouse effect is negative, resembling the modern Antarctic plateau (Sejas et al., 2018). The greenhouse effect can be calculated as $G = \sigma T_S^4 - \text{OLR}$, where σ is the Stefan-Boltzmann constant, and OLR is outgoing longwave radiation. Surface temperature change due greenhouse warming is $\Delta T_g = [T_S - \frac{\text{OLR}}{\sigma}]^{1/4}$. At 50 ppm, G ranges from 0.7 W m^{-2} to 2.6 W m^{-2} , and ΔT_g , is between 0.9 and 2.3 K (higher warming at lower bare-land albedo). At 200 ppm and 0.2 albedo, G is 4.4 W m^{-2} , and ΔT_g reaches 3.5 K. Pierrehumbert (2005) obtained a similarly small value for the global average on a hard snowball; his Figure 4 shows a clear-sky greenhouse effect of $\sim 8 \text{ W m}^{-2}$. These snowball values are much smaller than those for the modern Earth, where $G \approx 150 \text{ W m}^{-2}$ and $\Delta T_g = 33 \text{ K}$.

2.4 Results

2.4.1 Some of the land surface has above-freezing mean-annual temperatures, and much more has above-freezing temperatures seasonally.

In our runs with lower bare-land albedo, we find small areas of land that are above-freezing on annual average. These areas allow for the potential of “open water” refugia. But refugia do not require open water. If the end of an oceanic bay is below freezing on annual average, but the warmest month is above freezing, sea ice would form in the bay, and it would partially melt in summer. Neoproterozoic algae could have survived in the temporary meltwater pools on the ice, as has been observed by mat-forming eukaryotic algae on the McMurdo Ice Shelf and on the Ward Hunt Ice Shelf in the Canadian Arctic (Vincent et al., 2000; Vincent and Howard-Williams, 2000). In these modern analogs, organisms can survive perennially in ice that is deeply frozen for all but a few weeks or days per year. This would be the “ice surface” refugium described above in Section 1.1(d).

We find that in our coldest case (10 ppm CO₂, bare-land albedo 0.4), 0.1% of the land surface area reaches temperatures above the freezing temperature of seawater (-2°C) in at least one month of the year, despite a global mean surface temperature of -69°C (Figure 3.2a). In our warmest case (200 ppm CO₂, bare-land albedo 0.2) in which global mean surface temperature is -61°C , 17% of land surface area reaches temperatures warm enough to host liquid water in the warmest month. (Our specification of the freezing temperature as -2°C is a conservative choice. With perhaps 20% of the ocean water converted to land glaciers and sea glaciers, the salinity of the remaining seawater would increase, lowering its freezing temperature closer to -3°C .)

To investigate how refugia might form, we calculate the potential evaporation (PE, mm/day), a measure of the rate at which the atmosphere could evaporate or sublimate water from the surface, if that surface had unlimited water availability. Over land, we calculate PE using a modified version of the Penman-Monteith equation (Penman, 1948; Monteith, 1981; Scheff and Frierson, 2014). Over the ocean, it is equal to the latent heat flux from the ocean to the atmosphere converted to units of water flux (mm/day). The dry snowball atmosphere over land creates demand for water resulting in large areas of the land

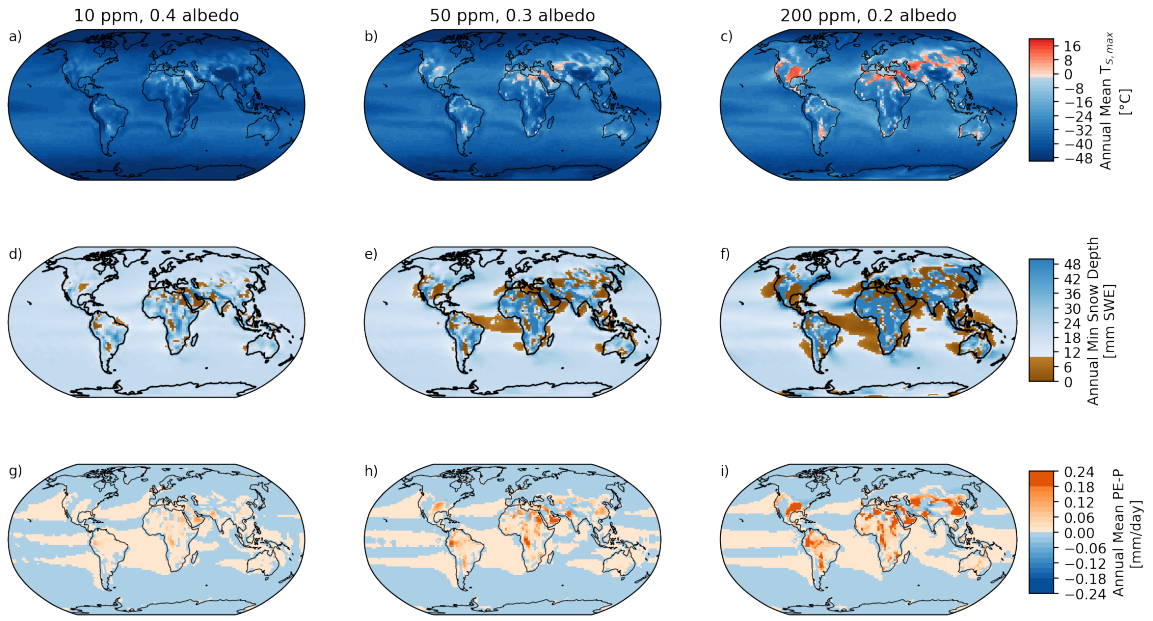


Figure 2.2: Habitability of the simulated snowball climate. **(a, b, c)** Surface temperature of the warmest month in the coldest simulated case (10 ppm CO₂, bare-land albedo 0.4), the midpoint simulation (50 ppm CO₂, bare-land albedo 0.3) and the warmest case (200 ppm CO₂, bare-land albedo 0.1), respectively. Red areas indicate locations with seasonal melting, suggesting the possibility of ice-surface refugia. **(d, e, f)** Annual minimum snow depth (monthly mean) from the same cases, given as mm snow water equivalent (SWE), which is equivalent to kg/m². Brown areas indicate places where snow depth drops below the threshold for surface-albedo change at some point during the year. Note that ocean areas without snow accumulation would nonetheless be covered by sea glaciers. **(g, h, i)** Annual mean potential evaporation (PE) minus precipitation (P) for the same cases.

surface that are snow-free for part of the year (Figure 3.2d-f). Above-freezing land surfaces are concentrated in places where PE outpaces precipitation – in particular, parts of the Arabian Peninsula, the modern Sahara Desert and eastern Asia (compare Figures 3.2a-c and 3.2g-i). Without snow cover, low-albedo land absorbs more solar radiation, allowing for above-freezing local land temperatures and the potential for unfrozen water and refugia if an ocean bay were to intrude to those locations.

A net-evaporative location experiencing mean-annual temperatures above freezing may thus serve as a refugium if it is connected via a narrow bay to the ocean, allowing seawater from below the sublimating sea glacier to flow into the bay and replace the water lost by evaporation.

Our model does not represent the growth of ice sheets on land. However, we can infer that snow-covered regions in Figure 3.2d-f are where ice sheets would grow; where they would flow would depend on the land's topography. Ice sheets have been directly simulated on Neoproterozoic continents (Donnadieu et al., 2003; Mitchell et al., 2015); they cover only parts of the continents, allowing large regions to be ice-free land.

2.4.2 Land surface albedo exerts control on the habitability of nearly-enclosed bays.

Land surface temperatures increase more strongly in response to decreases in bare-land surface albedo than to increases in CO₂, for the same magnitude of global radiative forcing. This response occurs across all latitudes and is stronger in regions with more total land area (Figure 3.3a). Starting from a baseline of albedo 0.4 and 10 ppm CO₂, increasing CO₂ from 10 to 200 ppm constitutes a global radiative forcing of 5.16 Wm⁻², while decreasing snow-free land albedo from 0.4 to 0.2 constitutes a smaller forcing of 4.06 Wm⁻² yet causes a greater increase of warm land area. The change of land area per unit of radiative forcing is shown in Figure 3.3b, for four cases of similar RF, two caused by increasing CO₂ and the others by decreasing albedo. Despite smaller globally mean radiative forcing from albedo changes, land surface temperatures are more responsive to albedo since the radiative forcing is concentrated over snow-free land.

Decreasing bare-land albedo facilitates potential refugia in two ways: (1) warming of bare

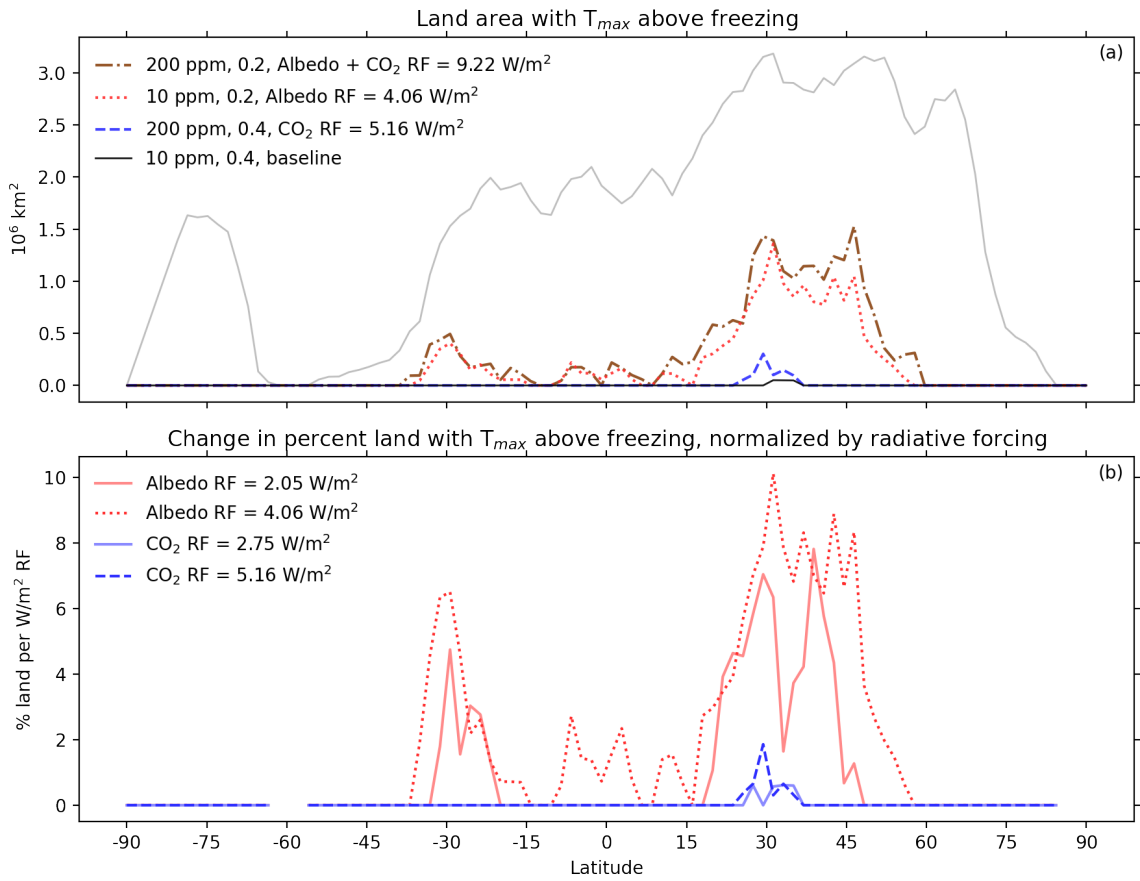


Figure 2.3: (a) Area of land (per 1.9 degrees of latitude increment) with temperature above freezing in the warmest month. Total land area is shown in grey. (b) Change in percent land area above freezing in the warmest month, per unit radiative forcing, relative to the coldest case (10 ppm CO₂, albedo 0.4).

land and (2) exposing new bare land that then becomes warm. In our simulations, both mechanisms occur to effect a change in habitability, with approximately 45% of the newly exposed land above freezing (in the warmest month) having become warm enough to host refugia through the first mechanism, and 55% through the second mechanism at constant CO₂. (Partitioning is similar at 10, 50, and 200 ppm CO₂). We do not see above-freezing temperatures in locations that have snow cover. If a warm, net-precipitating location did exist, it would become a warm ice sheet, like a modern temperate glacier or the wet-snow zone of modern Greenland.

Either decreasing bare-land albedo or raising CO₂ expands the area of potentially habitable land in coastal gridcells; continental interiors already meet the criteria for potential habitability at albedo 0.4. A world with low bare-land albedo would therefore be more likely to host life in narrow bays that intrude into the dark land. As mentioned above, the bare land in the Neoproterozoic probably resembled modern stony deserts rather than sand or soil, so its albedo may have been even lower than the lowest case we modeled (broadband albedo 0.2).

Figure 2.4 and Table 2.2 show, for the various combinations of CO₂ and albedo, the percent of land area capable of hosting refugia, were an arm of the sea to reach it, demonstrating again the relative importance of global radiative forcing by land albedo and CO₂. Starting from the coldest case (bare-land albedo 0.4, CO₂=10 ppm), positive radiative forcing results from either increasing CO₂ or reducing land albedo. For the same radiative forcing, a change of land albedo is more effective than a change of CO₂. Figure 2.4a shows this for the annual maximum temperature (T_{max}); the area of above-freezing land ranges from 0.1% to 12%, by decreasing bare-land albedo alone. [Even in the warmest case (bare-land albedo 0.2, CO₂=200 ppm), we do not see places with annual mean temperature $\bar{T} > -2^{\circ}\text{C}$. That would allow for “open-water” refugia, because during at least part of the year the bay would be ice-free.]

A temperature criterion is not sufficient. We also need PE > P so that land glaciers will not form at these locations. Figure 2.4b shows that the percent of land area with PE > P increases slightly with darkening of the land or increasing CO₂. Combining these criteria, Figure 2.4c shows the percent of land area with $T_{max} > -2^{\circ}\text{C}$ and PE > P.

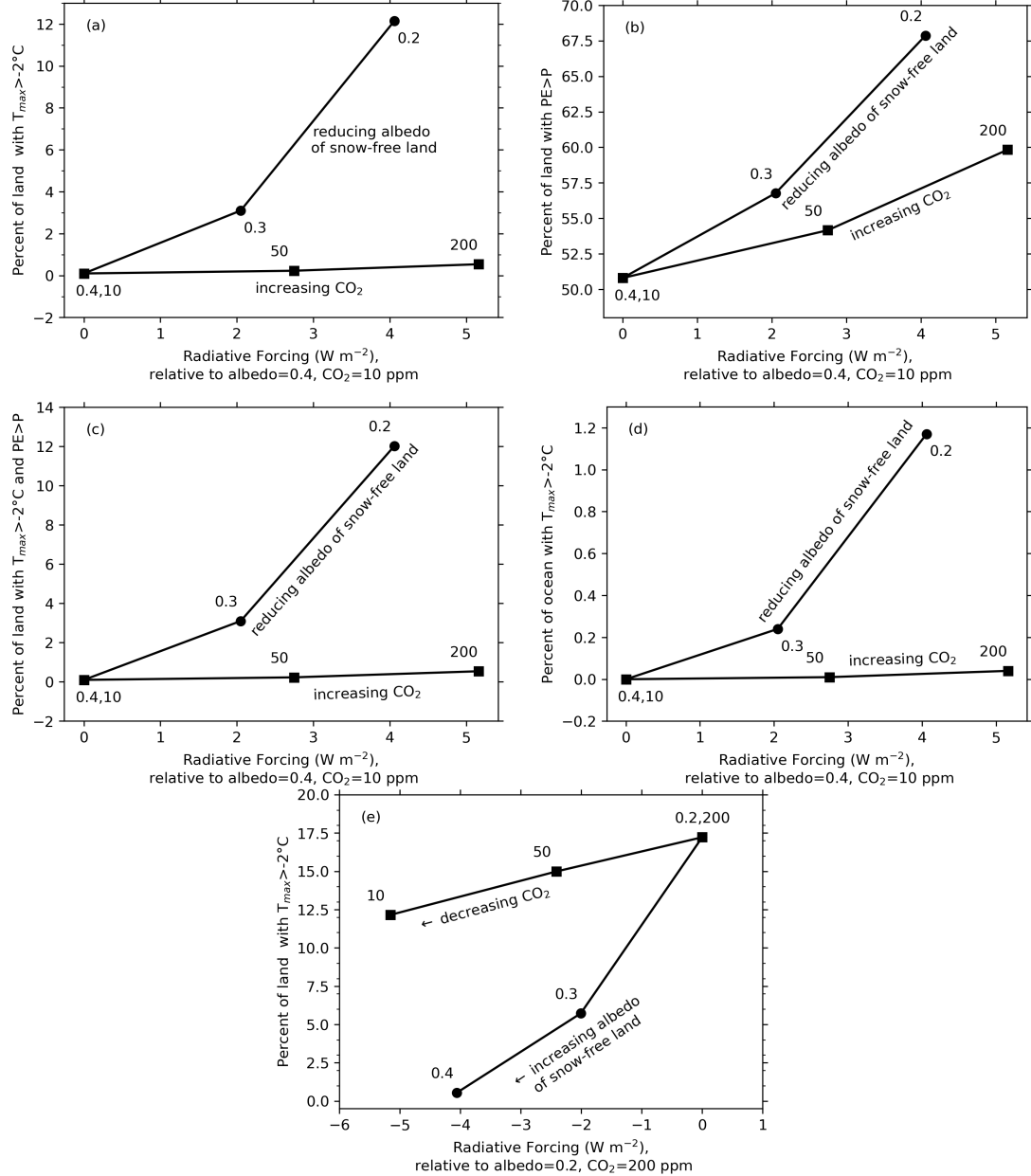


Figure 2.4: Percent of land area capable of hosting refugia, were an arm of the sea to reach it, for several combinations of CO₂ mixing ratio and bare-land albedo. Relative to the coldest case (albedo=0.4 and CO₂=10 ppm), the change in suitable land area is shown as a function of the radiative forcing, caused either by darkening the surface or by increasing CO₂. **(a)** Percent of land area with temperature of the warmest month $T_{max} > -2^\circ\text{C}$. **(b)** Percent of land area with mean annual PE>P. **(c)** Percent of land area with $T_{max} > -2^\circ\text{C}$ and PE>P. **(d)** Percent of ocean area with temperature of the warmest month $T_{max} > -2^\circ\text{C}$. **(e)** Percent of land area with temperature of the warmest month $T_{max} > -2^\circ\text{C}$ relative to the warmest case (albedo=0.2 and CO₂=200 ppm).

There are also some small areas of the ocean, all on coastlines, where the surface temperature exceeds -2°C in the warmest month, but in all cases these areas represent less than 2% of the ocean area (Table 2.2, Figure 2.4d).

With high-albedo land, the climate is so cold that very little of the land reaches above freezing even with 200 ppm CO₂, as shown in Figure 2.4a. But with the warmer climate for darker bare land (albedo 0.2), the above-freezing land area does become sensitive to the CO₂ level (Figure 2.4e).

2.4.3 Refugia on desert land?

Besides inhabiting the ends of narrow oceanic bays, photosynthetic eukaryotes may also have been active on unglaciated land surfaces. Reviewing “early life on land”, Lenton and Daines (2017) emphasized microbial mats powered by oxygenic photosynthesis. In their words: “Initially, such mats would have been dominated by [prokaryotic] cyanobacteria. Sometime during the Proterozoic Eon (2.5–0.54 Ga) they probably gained eukaryotic algae and fungi... Today a mixture of cyanobacteria, algae, fungi, lichens and nonvascular plants are found in terrestrial mats, often termed ‘biological soil crusts’ or ‘cryptogamic cover.’” Lenton and Daines cited evidence that “by the start of the Neoproterozoic (1 Ga), eukaryotes were probably present alongside cyanobacteria in terrestrial mats, but whether these were algae is unclear.” The soil-crust mats occur on modern midlatitude deserts that are seasonally above freezing, as in Utah and Nevada. Similar environments may therefore have offered a habitat for mixed prokaryotic/eukaryotic life in the deserts of Snowball Earth wherever the soil temperatures were above freezing seasonally, as also proposed by Retallack (2023). The locations would have to be in deserts (PE>P) to avoid burial by land-glaciers, but they could have received water from the local sparse precipitation, or from runoff modulated through topography.

2.5 Discussion and conclusion

In our simulations we used the albedo of firn rather than glacier ice (Table 2.1) to represent the snow-free parts of the frozen ocean, biasing the climate colder. Actual sea glaciers should have had a slightly darker surface, allowing for a warmer climate. Yet, despite our

conservative choice of a brighter ice surface, our results suggest that a “hard” snowball climate with ice extending to the equator could have allowed some locations to sustain the surface liquid water needed to host photosynthetic life, despite extremely cold global-mean temperatures. Our global annual mean surface temperatures \bar{T} are considerably colder than those of other GCMs simulating the hard-snowball climate. Abbot et al. (2013) reviewed six GCMs; we can estimate \bar{T} from their Figure 3.1a for 100 ppm CO₂: for five GCMs, $\bar{T} \approx -38^\circ\text{C}$; the cold outlier (the FOAM GCM) had $\bar{T} \approx 46^\circ\text{C}$. Our finding of above-freezing locations even with our extremely cold global mean surface temperatures, all in the range -61 to -69°C (Table 2.1), thus argues strongly for refugia on or near ocean bays.

Although we find strong evidence to support the potential for refugia, the distribution and type of refugia (ice-surface or open-water) would be sensitive to the actual bare-land albedo. The albedo of bare land surfaces during the Neoproterozoic may have been even darker than our darkest case (albedo 0.2), as land plants had not yet evolved, which would limit the erosion of rocks into smaller grain sizes, so that stony deserts, which have broadband albedo 0.10-0.15, would be more likely than modern deserts of soil or sand. If Neoproterozoic land surfaces were indeed dark like stony deserts, this lower land albedo would result in more refugia than we have simulated here.

We find that modern nearly-enclosed bays, resulting from continental rifting (e.g. the Red Sea), are especially habitable and could support seasonal refugia depending on the land surface albedo. Since the dynamics of sea-glacier invasions into nearly-enclosed bays occur below the resolution of the model simulations employed here (Campbell et al., 2011, 2014), our results quantify the maximum potential for refugia within a hard-snowball climate with modern continents; but the exact distribution of such nearly-enclosed bays on Neoproterozoic continents would determine true habitability. A constriction at the entrance to the bay helps to slow the sea glacier (Campbell et al., 2014), but the entrance must not be too shallow because ocean water needs a path below the ice to reach the refugium. The strait at the entrance to the Red Sea (Bab el Mandeb) is only 137 m deep (Siddall et al., 2002), so a sea glacier would likely become grounded there.

Since Neoproterozoic continental reconstructions are constrained primarily by paleomagnetism, which constrains the latitude but not the longitude, there remains large uncertainty

in the likelihood of large continental interiors, which we expect to strongly influence our results (Merdith et al., 2021). The total land area was probably only slightly smaller than today's (Hawkesworth et al., 2019), but the tropical bias in land distribution and degree of continental “clumping”, as well as the location and height of mountain ranges, could influence our results (Laguë et al., 2023).

Our conclusion is that the ends of narrow oceanic bays were likely to serve as refugia for photosynthetic eukaryotes, even during the coldest early phase of a snowball event.

Chapter 3

THE IDENTIFYING THE INFLUENCE OF CARBON CYCLE REPRESENTATION ON SINK SENSITIVITY, TOTAL WARMING, AND GLOBAL CARBON BUDGETS IN SIMPLE CLIMATE MODELS

Abstract

Complex models of the Earth system are increasingly able to represent details of the carbon cycle that determine how much carbon is taken up by the Earth's land and ocean, but a variety of approaches exist to simplify the representation of these processes in reduced-complexity models, or simple climate models (SCMs). Such models are useful for building conceptual understanding as well as informing policy decisions intended to mitigate global warming. We perform a comparison of four SCMs with varying carbon cycle structures in the historical period and by emulating global mean temperature response to idealized emissions trajectories. We find that carbon cycle representation influences the magnitude and uncertainty of land carbon uptake in decarbonization scenarios. These findings suggest that using one model in isolation to guide decarbonization decision-making may hide large uncertainties in how land and ocean sinks may behave in a decarbonization or post-net-zero emissions landscape.

3.1 *Introduction*

3.1.1 Quantifying structural uncertainty in coupled Earth systems

Identifying and quantifying uncertainty in the coupled climate-society system is important for understanding the total outcome of any human policy, as well as for developing climate-oriented benchmarks, such as the remaining carbon budget (Rogelj et al., 2019).

The Earth's carbon cycle contains many important feedback processes that together influence how the Earth's climate responds to increased or decreased net emissions of carbon dioxide (Friedlingstein et al., 2014; Arora et al., 2020).

In Earth System Models (ESMs) biogeochemical processes on land contribute significant uncertainty to the global climate response to emissions [many citations]. Modeling the coupled carbon-water cycle on land requires representing complex biological and ecological processes occurring on small scales (plant stomata open and close on the micrometer scale) by using poorly-constrained parametrizations operating at resolutions that are at least 10 orders of magnitude coarser.

This challenge of how to represent processes within the terrestrial carbon cycle is not likely to be resolved soon since it is representative of our incomplete understanding of how to represent them at global scales, and the number of parametrizations of different biological processes is more likely to increase than stabilize or decrease. Wieder et al. (2015) illustrate this by comparing two equally plausible formulations for biological nitrogen fixation (one calculated from net primary productivity and one calculated from evapotranspiration) in CESM2. They find that while both formulations lead to similar carbon fluxes and pools in mean steady-state pre-industrial pools, they diverge under a high-emissions scenario (RCP8.5) by about 30% in the northern hemisphere.

While these differences in carbon cycle representation can lead to different answers, having a diversity of ways of representing processes unveils the uncertainty stemming from incomplete representation. Comparing outcomes across different model architectures enables us to demarcate how much of our total uncertainty is due to this source.

3.1.2 Simple Climate Models

While Earth system models are capable of representing details of the climate system, the computational burden prevents them from being used for assessing a wide range of pathways. Simple climate models (SCMs) are used by a range of actors from scientists for intuition, global leaders to vet policy, and companies to scope climate-oriented projects. They are even used in the IPCC WG3 to scope climate solutions.

SCMs can be built to emulate ESMs. While ESMs may contain representations of carbon cycle processes that are more mechanistic and rely on empirical or mechanistic observable mechanisms, leading to deterministic simulations, the structure of SCMs varies.

The benefit of SCMs is primarily in their computational efficiency. Because of their reduced complexity, SCMs can simulate thousands of scenarios on one CPU in a matter of seconds or minutes, allowing users to sample across both internal variability and scenario uncertainty with ease. This usability make them far more attractive and ubiquitous tools for policy- or technology-scoping use cases.

Since CMIP-class ESMs are too computationally expensive to explore the full parameter space of structural uncertainties and future scenarios, we can use reduced complexity or “simple” models, which emulate CMIP-class GCMs to test the range of temperature response we get from decreasing CO₂ emissions.

Emissions-driven climate model emulators are physically based emulators that can reproduce ESM dynamics and offer insight into dominant carbon cycle processes. They are used to assess and plan decarbonization pathways, scope CMIP scenarios for ESMs, emulate the climate for economic models, and offer insight into the dominant carbon cycle processes at the global scale.

For this reason, they currently play a powerful role in scenario development and in particular for Working Group III Mitigation Assessment of the IPCC (2022), a set of three climate model emulators were used to vet and classify a large database of scenarios generated from economic models (Kikstra et al., 2022). The emulators were used to classify into the different warming categories, with those limiting warming to below 2°C being the most desirable. In the report, pathways that are able to limit warming to 2°C (with high likelihood), projected CO₂ emissions to be reduced between 2019 and 2050 by around 49% for energy demand, 97% for energy supply, and 136% for agriculture, forestry, and other land use. The implication is that successful mitigation strategies entail dramatic modifications to the existing land carbon sink. While three models are run, FaIRv1.6.2 and MAGICCv7.5.3 and use the CICERO simple climate model (CICERO-SCM) for sensitivity analysis, only MAGICC’s results are reported in the final assessment since they capture the range of the other models.

While at the international scale, this set of multiple models is run to characterize potential mitigation scenarios, at marginally smaller scales, it is common to run only one emulator, varying parameters to emulate ESMs to sample across uncertainty in the forced

response to emissions. In the EU, the climate model, MESMER is used on its own to

- Example: Use of MESMER for EU policy scoping (SPARCCLE)
- Example: Use of FaIR in Rhodium Group Climate Outlook report
- Example: Use of HECTOR in CarbonPlan assessment of ocean carbon removal

Since SCMs are built to produce the climate response to radiative forcing, they inherently include a representation of the carbon cycle. The SCMs vary in how implicit or explicit that representation is.

3.1.3 Decarbonization regime (vs emissions)

An important obstacle in modeling any kind of solution, even with an ESM is that decarbonization emissions scenarios are necessarily new territory for our observed climate system and our climate models.

3.1.4 Ubiquity of Simple Climate Models

The ubiquity of their use in modern climate decision-making, their diversity in structure, and the inherent uncertainty of an imminent untested emissions regime, together make SCMs important and exciting subjects for inter-comparison for the purposes of assessing structural uncertainty.

3.1.5 Metrics of climate sensitivity: Transient Climate Response to Cumulative CO₂ Emissions (TCRE) and the Zero-Emissions Commitment (ZEC)

We use two metrics that can be used in conjunction with one another to quantify the remaining carbon budget for climate stabilization. The first is the Transient Climate Response to Cumulative CO₂ Emissions (TCRE) (MacDougall, 2016) and the second is the Zero-Emissions Commitment (ZEC). The TCRE can be defined as the modeled proportionality (or slope) of transient global mean warming to cumulative emissions. ESMs consistently exhibit this emergent response to cumulative emissions across a wide range of cumulative

emissions pathways (Koven et al., 2022). In scenarios reaching net-zero (or net-negative) emissions, some of the committed temperature response to emissions is realized after emissions reach zero, which is quantified as the ZEC, evaluated at some designated time after emissions cease. ZEC can be seen as a measure of the relative strength of lagged warming to lagged CO₂ uptake operating over longer timescales when emissions reach net-zero or net-negative (Koven et al., 2022). The use of the two metrics together allows for the quantification of a total CO₂ remaining carbon budget international warming threshold targets of 1.5 or 2°C (Rogelj et al., 2019; Jones and Friedlingstein, 2020).

We can use TCRE and ZEC to estimate a remaining carbon budget using the following inputs: (1) anthropogenic warming to date (2) cumulative historical CO₂ emissions and (3) current non-CO₂ fraction of total anthropogenic forcing

In theory, ZEC can be quantified as the temperature change taking place after net-zero, though in practice, when emissions decrease progressively (as opposed to falling to zero rapidly), some of the ZEC can be realized before emissions cease (Koven et al., 2023), meaning that ZEC may be more accurately quantified as the temperature change with respect to the expected linear TCRE.

[ESM bell curve removes discontinuities in the emissions curve (why is this good again?) and flat10 allows TCRE and ZEC to be distinct. If we validate that ZEC and TCRE are about the same, this allows us to use flat10 in future work to diagnose ZEC.]

Quantifying and understanding the underlying dynamics controlling ZEC is essential for predicting peak-CO₂-driven warming, the relative timing between peak emissions and peak warming, and the remaining carbon budgets (Koven et al., 2023).

3.1.6 Research Questions

1. How does the carbon cycle structure in an SCM influence the magnitude and timing of warming in an decarbonization scenarios?

2. How do different model structures allocate carbon to land and ocean sinks, and how do the allocations differ depending on emissions mode (increasing or decreasing)?

Model	Carbon cycle structure	Reference
FaIR	4 fixed-allocation timescales, $\alpha\tau_i$, of carbon removal.	Millar et al. (2017); Smith et al. (2018); Leach et al. (2021)
HECTOR	3-box terrestrial model with LUC 4-box ocean model	Hartin et al. (2015, 2016); Dorheim et al. (2023)
MAGICC	3-box terrestrial model Modified impulse response ocean model	Meinshausen et al. (2011)
Swann/Deutsch Box Model	9-box terrestrial model 7-box ocean model	Swann (2010) Toggweiler (1999)

Table 3.1: Carbon Cycle Approach by Model

3.2 Methods

3.2.1 Models

We compare four models of varying structures, levels complexity, and applications. In Table 4.2, we describe the components of how the carbon cycle is represented in each model. In Figure 3.1 each model’s carbon cycle structure is portrayed as a schematic diagram, illustrating the variation in structure that we explore.

FaIR

At the lowest level of complexity, we run the Finite-amplitude Impulse Response Model, version 2.1.3, or FaIR (Leach et al., 2021; Smith et al., 2018; Millar et al., 2017). FaIR’s carbon cycle is a modified version of the four-timescale impulse response function for carbon dioxide derived by Joos et al. (2013). In practice, FaIR’s carbon cycle is composed of four reservoirs with unique timescales of carbon removal from the atmosphere, $\alpha\tau_i$, such that τ_i

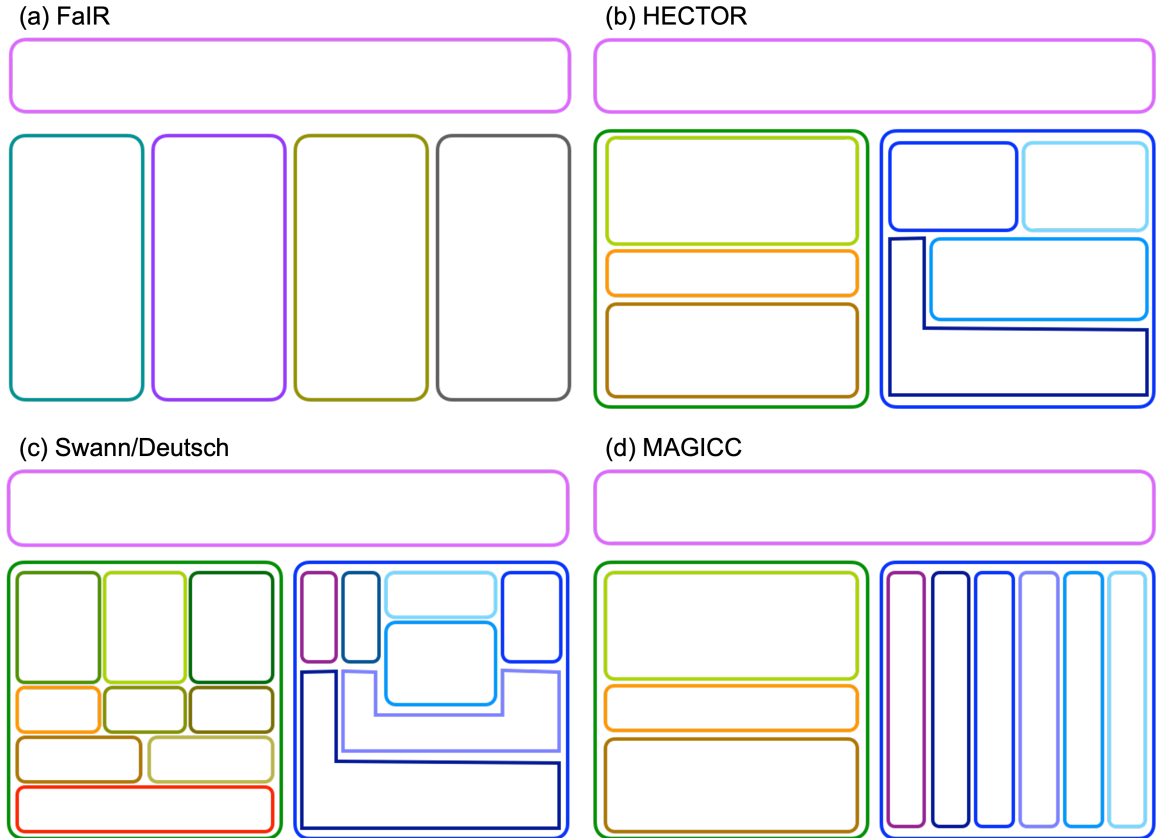


Figure 3.1: Carbon cycle structures for each SCM. In each schematic, a pink horizontal rectangles at the top represents the SCM's atmosphere carbon pool. HECTOR, Swann/Deutsch and MAGICC represent land and ocean carbon cycles separately and explicitly and have been colored green and blue to indicate terrestrial and ocean carbon representations, respectively. HECTOR and Swann/Deutsch contain representations of ocean circulation, which influences carbon draw-down from the atmosphere to the ocean.

is the characteristic timescale for reservoir, i , and α is an adjustment factor, computed at each time step and applied to all characteristic timescales. Each timescale of decay operates on a specified fraction of the emissions to the atmosphere, a_i , (approximately one fourth for each reservoir), such that:

$$C(t)/C_0 = a_0 + \sum_{i=1}^4 a_i e^{\frac{-t}{\alpha\tau_i}} \quad (3.1)$$

(Also see Equation 2 of Leach et al., 2021)

HECTOR

At the next level of complexity, we run HECTOR version 3.2.0, an open-source, process-based, carbon-climate model that calculates the globally-resolved flow of carbon and energy between the atmosphere, ocean and terrestrial biosphere, as described by Hartin et al. (2015, 2016). Anthropogenic emissions are emitted from a geologic carbon pool, `earth_c`, and LUC emissions are emitted as fractions of the land carbon pools (`veg_c`, `detritus_c`, and `soil_c`).

In HECTOR's terrestrial carbon cycle component, atmospheric carbon flows to the vegetation pool through net primary productivity (NPP). The rate of NPP varies with atmospheric carbon, modified by a user-set fertilization parameter, β . Carbon flows from live vegetation to detritus and soil; detritus flows to soil, and both detritus and soil carbon return to the atmosphere through respiration. Respiration is modified by a Q_{10} factor. The CO₂ fertilization feedback and respiration response to temperature that β and Q_{10} represent, respectively, modify the flux of carbon between land and atmosphere pools in opposing directions. NPP increases with higher CO₂, and respiration also increases with higher CO₂ driven by higher temperatures.

HECTOR's ocean carbon cycle component is composed of four ocean boxes – two surface (one cold high-latitude and one warm low-latitude box), one intermediate, and one deep ocean box. The flux of carbon between the atmosphere and each surface ocean box is a function of the gradient in $p\text{CO}_2$ between the atmosphere and ocean box at each time step (Equation 11 of Hartin et al., 2015). Within each surface box, $p\text{CO}_2$ is calculated as a

function of temperature, salinity, and pH. Temperatures of the surface ocean boxes are linearly related to atmospheric temperature (allowing the cold high-latitude box to be a stronger sink). Carbon is transported between ocean boxes in a prescribed circulation. The total ocean sink at each time step is the sum of all ocean fluxes.

MAGICC

MAGICC is the primary simple climate model used by the IPCC. We run MAGICCv6.0, a hemispherically-averaged upwelling-diffusion ocean coupled to an atmosphere layer and a globally averaged carbon cycle model (Meinshausen et al., 2011). While many aspects of MAGICC are highly complex, the carbon cycle model is distinct from but of similar complexity to HECTOR and the other models included in this analysis.

MAGICC's terrestrial carbon cycle component is similar to HECTOR's terrestrial carbon cycle with three pools (live vegetation, detritus, and soil pools) representing carbon flow between each pool. It can also represent deforestation explicitly.

The ocean carbon cycle component uses a modified impulse-response function to represent the carbon sink (Joos et al., 1996; Meinshausen et al., 2011). The IRF is derived from

SWANN-DEUTSCH

The Swann-Deutsch (SD) model can be seen as the highest-complexity carbon cycle model in its structure of both the land and ocean. Similarly to HECTOR, atmospheric CO₂ is computed as the difference between emissions sources and land and ocean carbon sinks.

The terrestrial part of our carbon cycle box model (Swann, 2010), consists of 9 carbon pools, with fluxes between them. There are 3 live pools, leaf, root and wood, 3 detritus pools and 3 soil pools - with their own turnover times. Each carbon pool has a timescale, τ , associated with it. For the live pools (leaves, roots, and wood) that timescale represents the average lifetime before that part of the plant will die (mortality). For the dead pools it represents the average time carbon spends in that pool before either being respired or transferred to another dead pool. The timescale of a given carbon pool depends on the

environment and ecosystem in which it exists. The SD model also represents CO₂ fertilization and the response of respiration to temperature as the β and Q_{10} as user-set parameters respectively.

The ocean model is a seven-box model of the ocean overturning circulation with nutrient and carbon cycles adapted by Curtis Deutsch from Toggweiler (1999). The seven boxes include four surface, one thermocline/intermediate, one mid-depth, and one deep ocean box. Like HECTOR, the SD model contains a chemistry submodule to compute $p\text{CO}_2$ from salinity and temperature.

We couple the SD carbon cycle model to FaIR, so that at annual time steps, FaIR computes a temperature from atmospheric CO₂, using a 3-layer energy balance model, which is then passed to the SD model at the next time step.

3.2.2 Simulations

Emissions trajectories for each of the four scenarios is shown in Figure 3.2.

Historical: Global Carbon Budget

We drive a historical simulation for each model using emissions of CO₂-FFI and CO₂-LULUCF beginning in 1850 from the Global Carbon Project Budget 2021 (Friedlingstein et al., 2022). Forster et al. (2023) Emissions are dropped to zero after the record ends in 2021, and simulations are continued until 1000 years of simulation are complete.

Observations of global mean CO₂ concentration and growth rate are from the NOAA Global Monitoring Network (Lan et al.).

[GCB Historical plus ZEC]

Idealized

We run a set of idealized runs that are designed to diagnose the response of the carbon cycle to a decarbonization regime. These include a Flat10_ZEC, a Gaussian emissions scenario, which we refer to as the ESM-Bell curve, and a 500 PgC pulse emissions scenario. In the Flat10-ZEC emissionss scenario, 10 PgC is emitted every year for 100 years, immediately

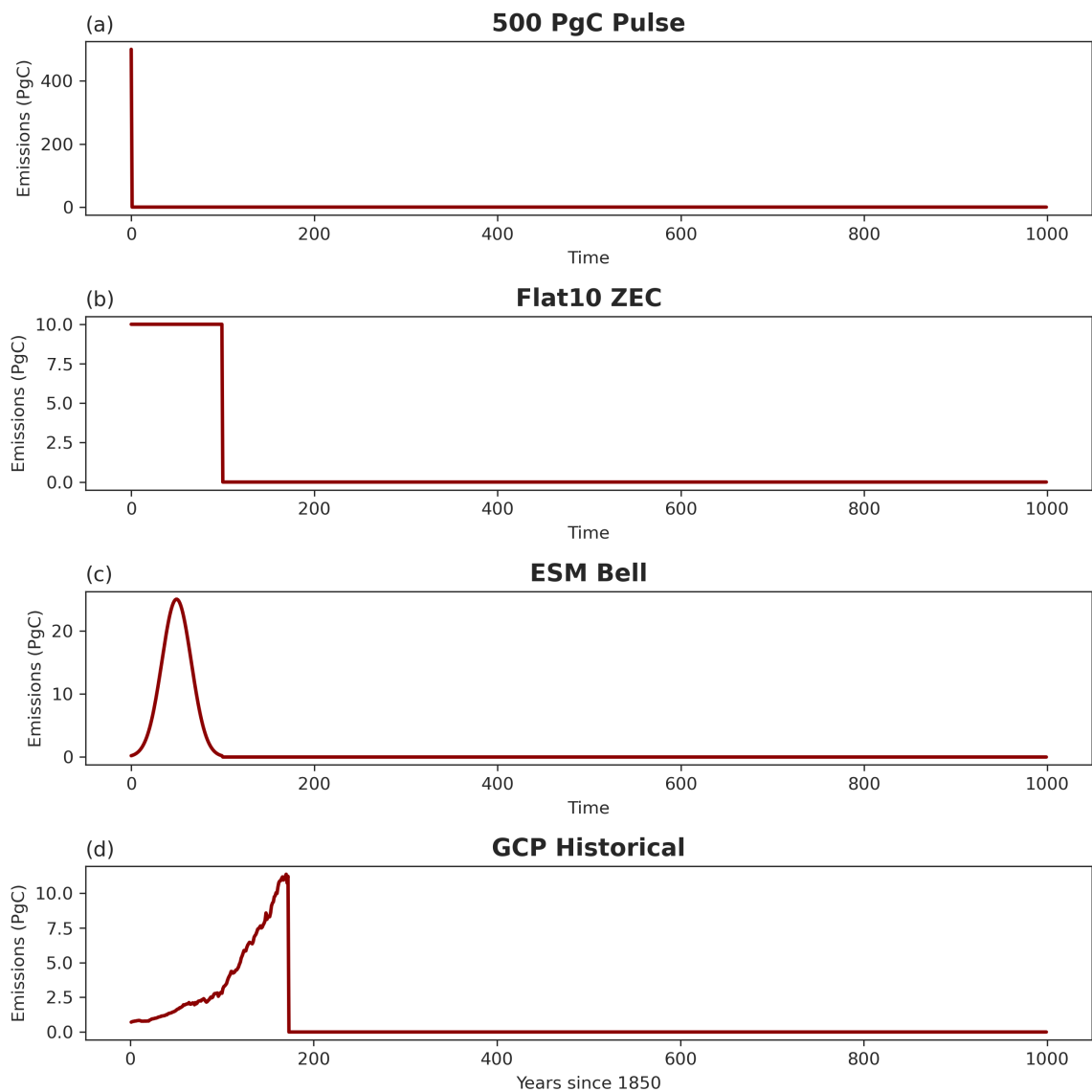


Figure 3.2: Emissions scenarios

followed by zero emissions. In the ESM-Bell curve, we use the emissions scenario from ZECMIP in which a Gaussian bell-shaped curve of emissions is followed, which reaches 1000 PgC in year 100, and smoothly transitions to zero emissions at year 100. In the 500 PgC pulse experiments, a pulse of 500 PgC is emitted followed by zero emissions.

We run the idealized simulations for a total runtime of 1000 years for each emissions scenario.

[Flat10ZEC is now in the CMIP7 fast-track; all models will be running this experiment; and context for CMIP7 esm runs]

3.2.3 Configuration

Unlike MAGICC, FaIR, and HECTOR, the Swann-Deutch carbon cycle model is un-tuned in its default configuration. Minor hand-tuning is done to calibrate the SD model to align with historical observations of temperature. Outside of this adjustment, the SCMS are run largely in their default configuration in order to diagnose the initial inter-model spread and in order to bring into relief any potential bias that would be assumed in running a single model on its own.

3.3 Results

3.3.1 SCMs produce historical CO₂ concentration record well.

All models reproduce historical observations of CO₂ concentration in their default “out-of-the-box” configuration. We compare the each model’s airborne CO₂ to observations of global mean CO₂ concentration from the NOAA Global Monitoring Network (Lan et al.). Historical airborne fraction in response to historical emissions is consistent across models and is and in line with observations. Figure 3.3 shows the fidelity of each model to the observed CO₂ record.

Since the SCMs were built using historical emissions-to-concentration as ground-truth and, in the cases of FaIR, HECTOR, and MAGICC, have been tuned to produce airborne fractions consistent with ESM and consequently real-world CO₂ concentrations, this result is relatively unsurprising. However, it demonstrates their ability to reproduce the forced

response of ESMs to historical emissions. As a result, we can use this result to validate that SCMs are able to capture the principle dynamics of the global carbon cycle at play in an increasing-emissions regime of the historical period.

3.3.2 Wide range of climate paths from the same emissions trajectory.

In all simulations, the spread between SCM atmospheric CO₂ and global temperature anomaly increases following net-zero. The spread increases to a maximum between 50 and 200 years after net-zero with minimal decrease in spread afterward.

While the response to historical emissions was not surprising given that all models have been built to reproduce historical emissions-to-concentrations, what is surprising is the response to emissions starting in 2022 when emissions are dropped to net-zero. Figure 3.4 shows atmospheric CO₂ in the historical (pre-2022) and after a hypothetical drop to zero emissions (post-2022). SCMs display a maximum spread in CO₂ of 57.7 ppm 49 years following cessation of emissions (compared to a maximum spread of 23.4 ppm in 2021, the last year of historical emissions).

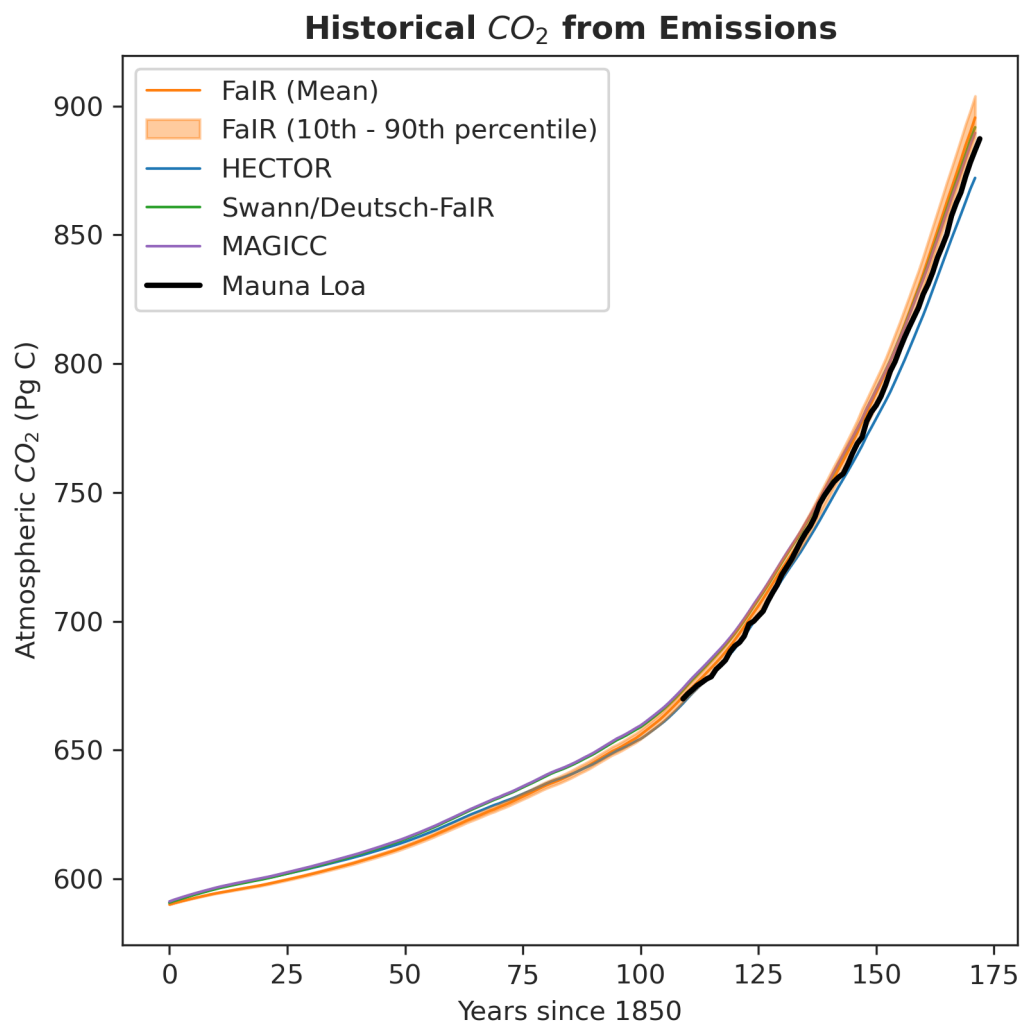


Figure 3.3: Historical CO₂ concentration for all models.

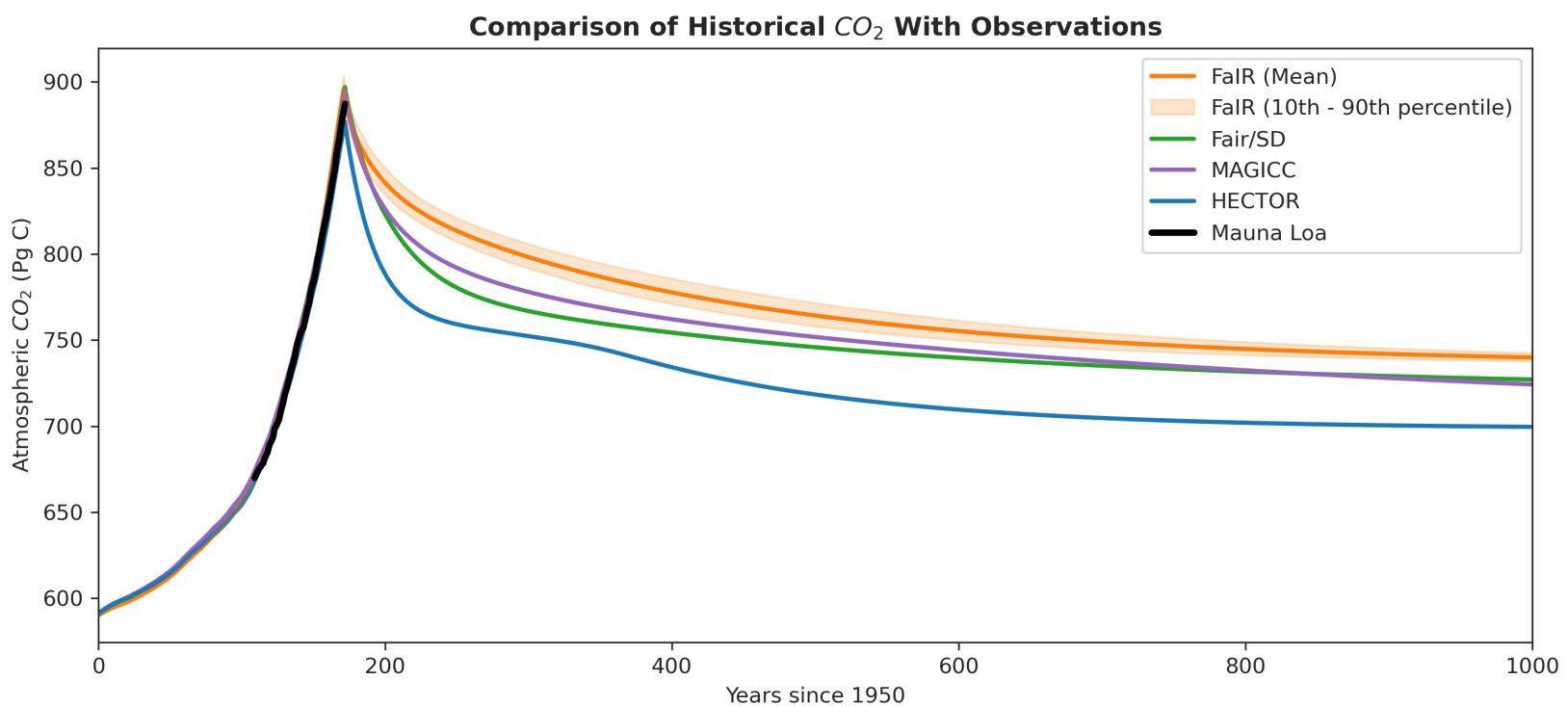


Figure 3.4: GCP to net-zero

In response to the 500 PgC pulse, a large initial spread between models of more than 150 ppm is driven by a sharp decrease in airborne fraction due to FaIR’s short (4-year) timescale uptake, which causes FaIR to show a sharp decrease in atmospheric CO₂ during the first four years of the scenario. After this initial divergence, the models see a secondary maximum spread 68 years following net-zero of 53.6 ppm (between FaIR and HECTOR) driven by a more rapid decline in atmospheric CO₂ in HECTOR compared to FaIR. The spread between modeled CO₂ only slightly declines after this point. The response of CO₂ in the AR5-IR model is included in Figure 3.5.

From this pulse experiment, we can detect that long-term differences in atmospheric CO₂ can be traced back to differences in rates of carbon removal in the first 200 years following the decrease in emissions to net-zero.

The spread in atmospheric CO₂ across models leads to a corresponding spread in the temperature response in the 500 PgC pulse emissions scenario. Temperature differences persist and increase slightly after year 200, leading to a 0.23K range in mean global temperature anomaly after 1000 years.

In both the ESM bell curve (Figure 3.6) and the Flat10 ZEC (Figure 3.7) emissions scenarios, the SCMs develop a spread in atmospheric CO₂ in the first 200 years following the beginning of decarbonization (years 50-100 for the ESM bell curve scenario and year 100 for the Flat10 ZEC). Similarly to the 500 PgC pulse scenario, the spread in atmospheric CO₂ stabilizes after the first 200 years and persists until the end of the simulation. The concomitant spread in global mean temperature increases and persists, largely driven by the unique evolution of HECTOR’s atmospheric CO₂. The timing of HECTOR’s carbon sinks lead to a consistent kink in atmospheric CO₂ approximately 80 years after net-zero in all scenarios.

3.3.3 Models disagree on long-term global temperature response.

Figure 3.7 shows the carbon and climate response across models in the flat10_zec scenario. While some differences emerge in the emissions phase (before year 100), which can be seen in Figure 3.8, the difference in ZEC, or the temperature evolution after decarbonization can be

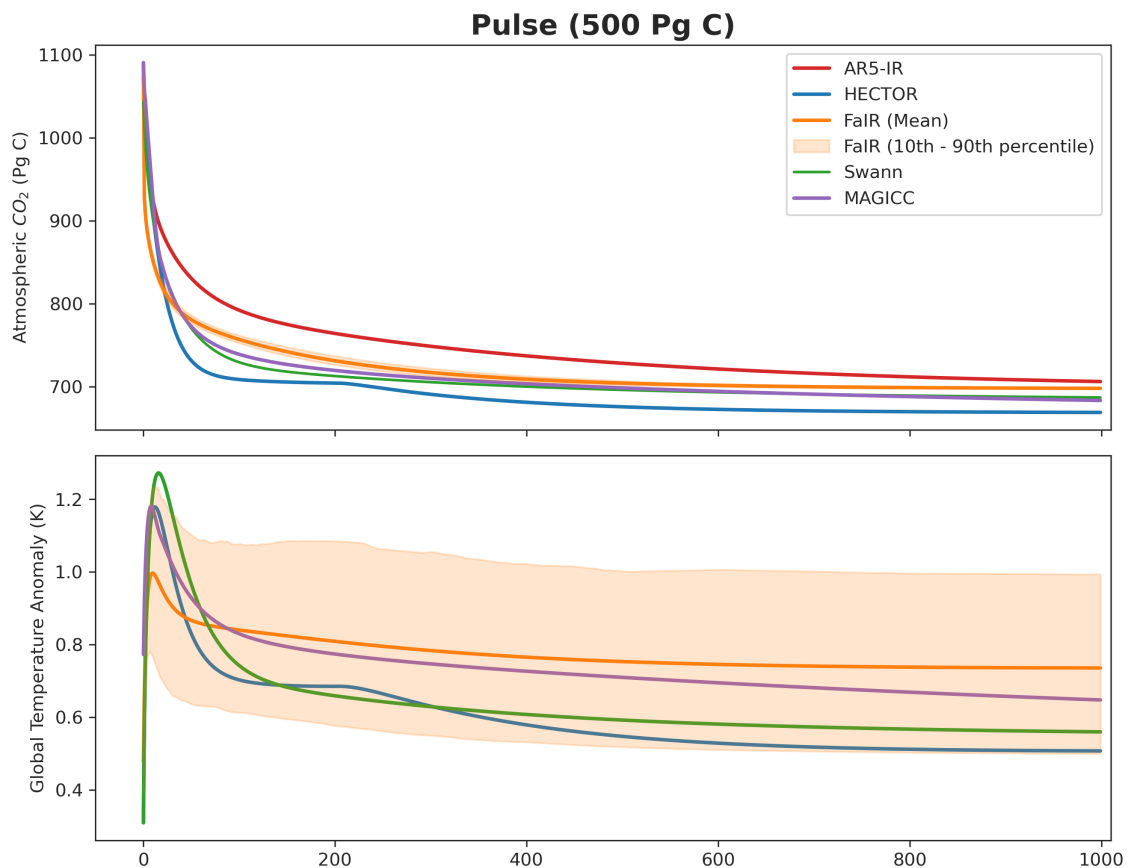
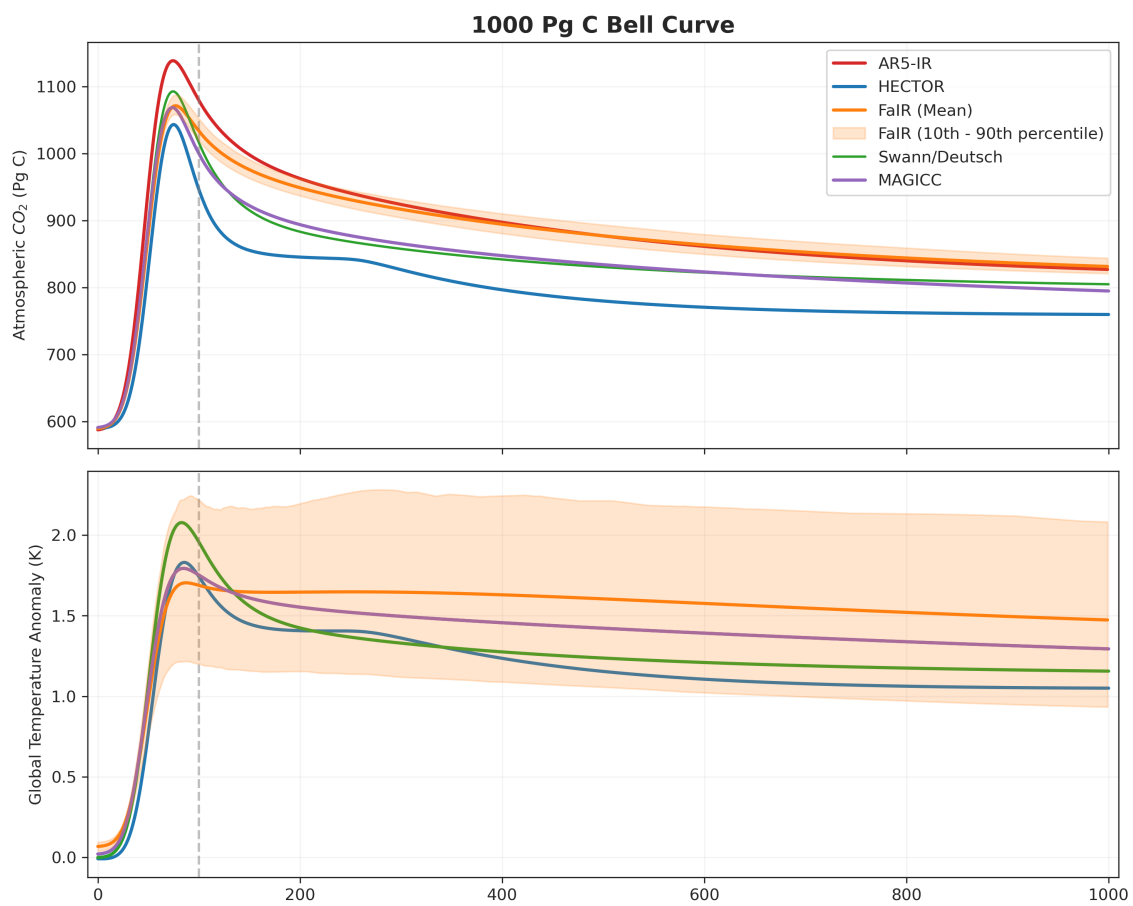


Figure 3.5: 500 PgC Pulse CO_2 and temperature

Figure 3.6: ESM Bell [CO₂] and temperature

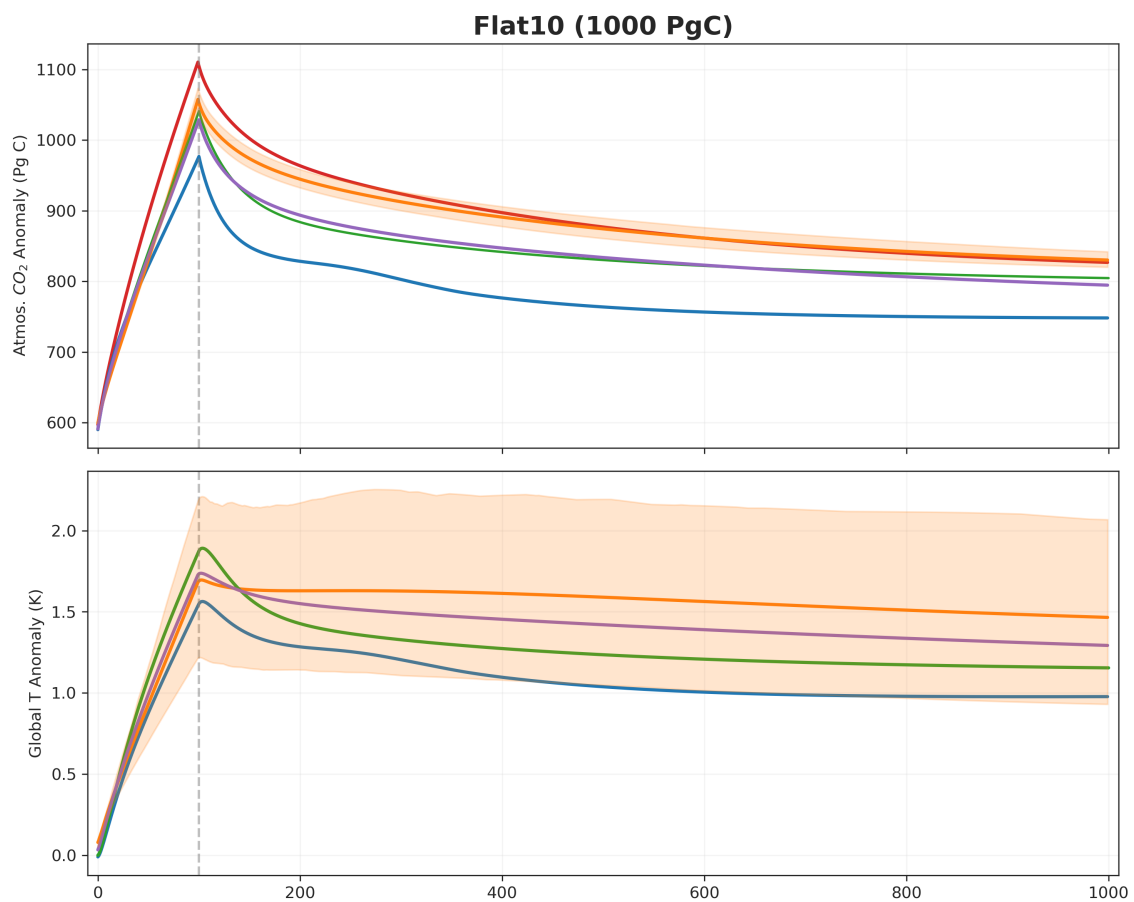


Figure 3.7: Flat10-ZEC [CO₂] and global temperature anomaly.

compared in Figure 3.9, in which all models begin with respect to their own TCRE at year 100 and the evolution of temperature with respect to TCRE1000 is show. This illustrates that the behavior of the longterm sinks varies from each other, leading to a widening spread in ZEC over the first 200-300 years, and allow the spread to stabilize but not shrink over the following 600 years.

Figures 3.8 shows the comparison of TCRE+ZEC50 in SCMs (squares). While SCMs exhibit differences in TCRE and appear to converge after 50 years, this convergence is only temporary, marking the approximate point where the temperature anomalies of FaIR, FaIR_SD, and MAGICC shift reposition. If the clock were stopped at ZEC50, it might look like the sum of TCRE and ZEC is consistent across these three models, but over time, the change in temperature driven by ZEC outweighs the TCRE, and the models display a spread of about 0.5°C by year 1000 of simulation.

In Figure 3.8, are the TCRE+ZEC50s calculated from the same flat10_zec emissions scenario for a selection of ESMs participating in a Flat10 intercomparison project for context. The data for these ESMs is courtesy of [who to cite here?]. 50 years after net zero, ESMs have a range in total temperature response of over 1°C.

3.3.4 Structural differences between SCMs lead to different carbon cycle outcomes and climate responses

HECTOR, MAGICC, and FaIR_SD allocate carbon to physical pools corresponding to the terrestrial and ocean carbon cycles. Figure 3.10 shows how those pools are allocated in the flat10_10 emissions scenario. Notably the largest differences are in long timescale carbon pools – ocean and soil pools. During the period with the largest differences in atmospheric CO₂, HECTOR allocates more carbon to soil pools than to detritus or live vegetation pools put together. Whereas MAGICC and FaIR_SD allocate larger amounts of carbon to live vegetation (leaves, wood, and roots). FaIR_SD allocates the least amount of carbon to ocean pools.

We can compute a remaining carbon budget for each SCM and compare the spread across model structure to the spread in other factors influencing the remaining carbon

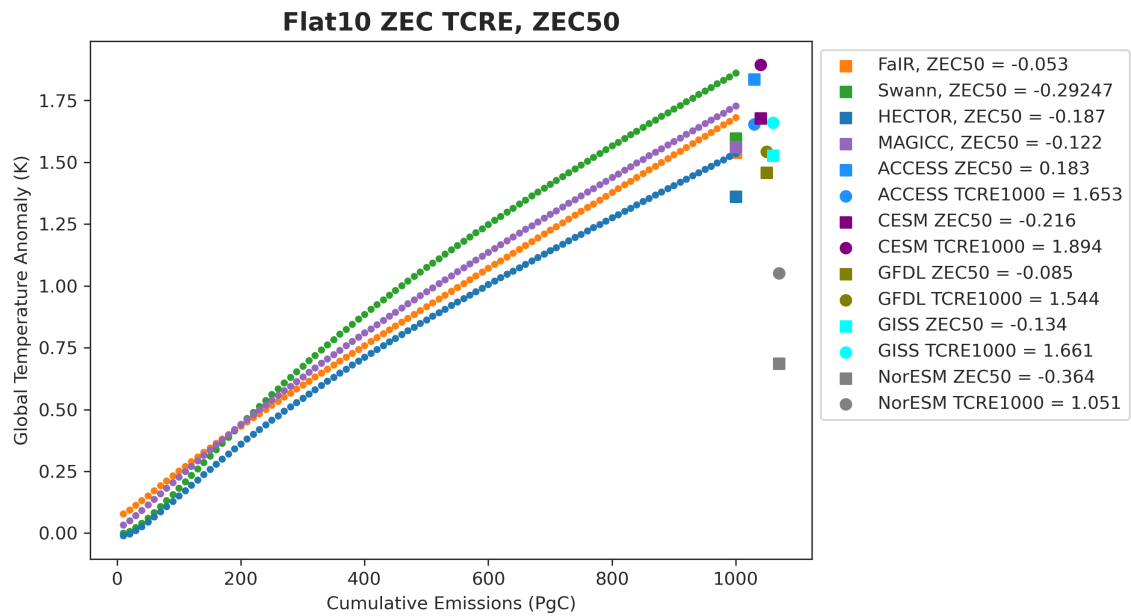


Figure 3.8: Flat10 ZEC TCRE and ZEC50 for all models and ESMs.

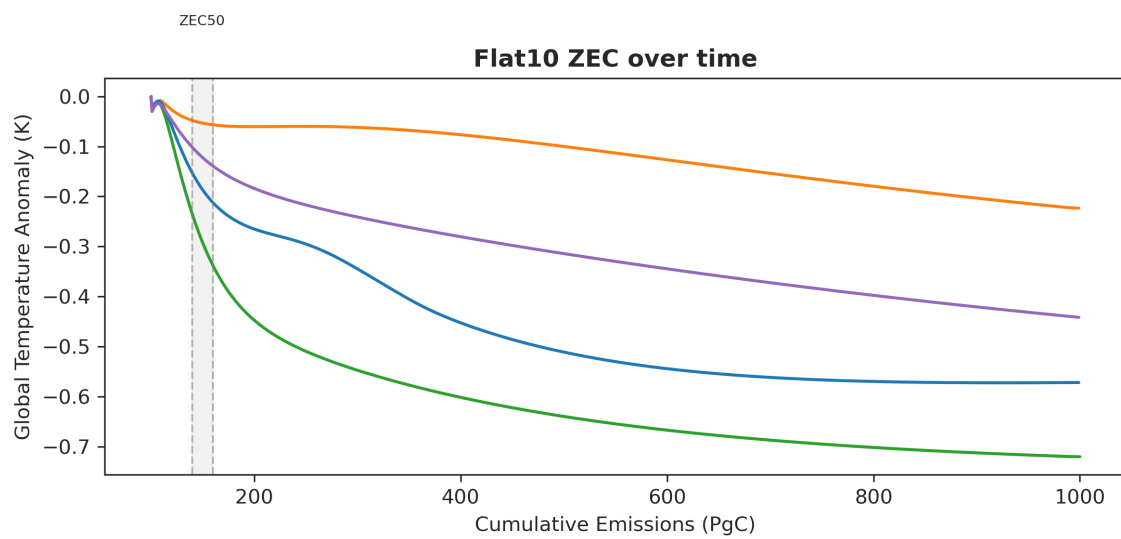


Figure 3.9: Flat10-ZEC [CO₂] and global temperature anomaly.

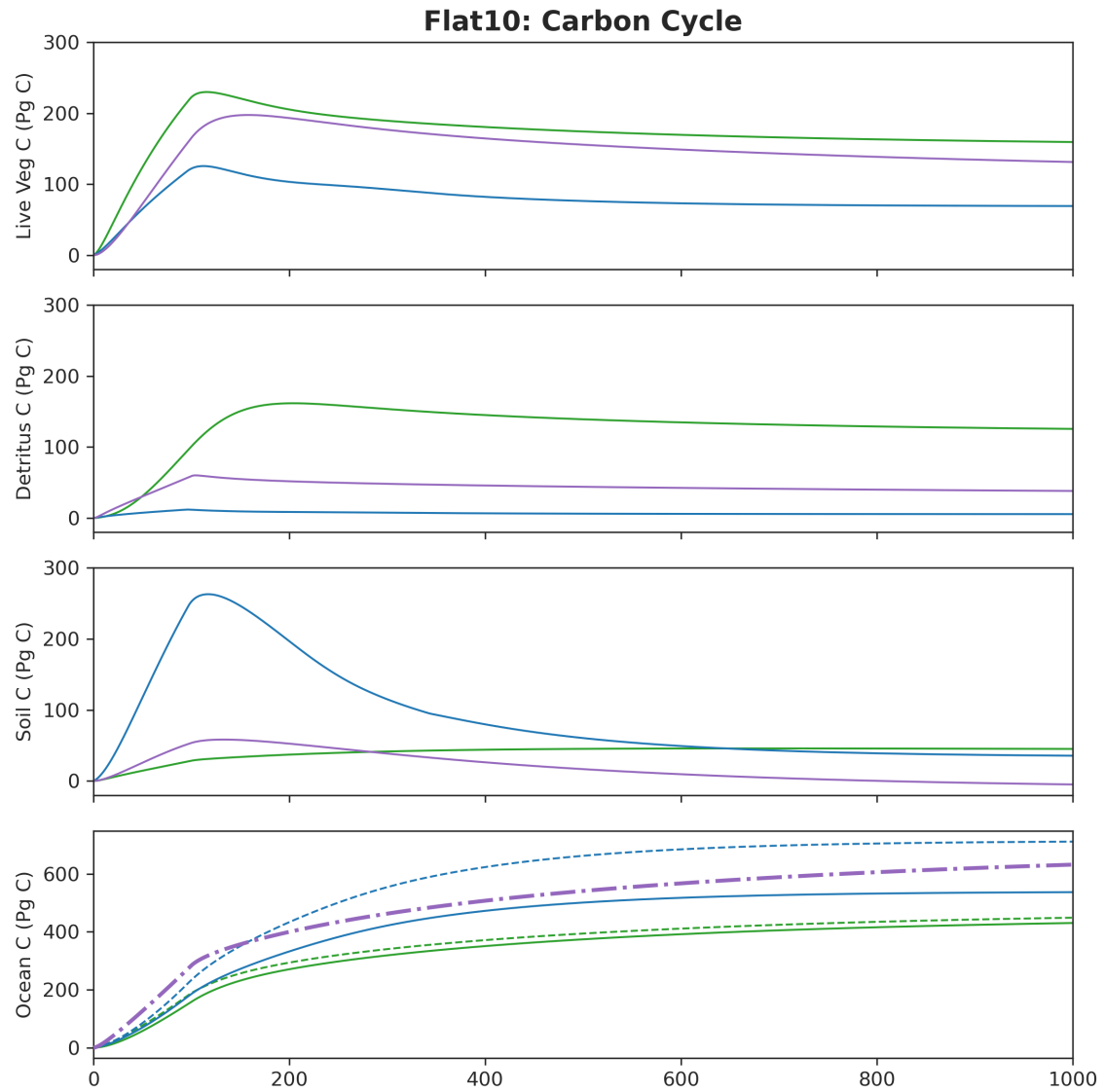


Figure 3.10: **Flat10-ZEC Carbon pools.** For FaIR_SD (green), HECTOR (blue), and MAGICC (purple), time evolution of carbon pools for the flat10_zec experiment. Solid lines in the ocean pools indicate the sum of the non-surface pools, while the dashed lines represent the total ocean pool size. MAGICC's total ocean carbon is plotted as the purple dash-dot line.

budget (RCB).

To do so we follow the example of Rogelj et al. (2019) to estimate the terms in the equation for RCB for a given temperature change limit (T_{lim}) as a function of the historical anthropogenic warming to date (T_{hist}), the non-CO₂ contribution to future temperature rise, T_{nonCO_2} , the Zero Emissions Commitment, given as T_{ZEC} in Equation 3.2 and TCRE, and finally an adjustment factor for sources of unrepresented Earth system feedbacks (E_{Esfb}).

$$\text{RCB} = \frac{T_{\text{lim}} - T_{\text{hist}} - T_{\text{nonCO}_2} - T_{\text{ZEC}}}{\text{TCRE}} - E_{\text{Esfb}} \quad (3.2)$$

We set a limit of 1.5°C for T_{lim} . T_{hist} can be estimated from observations with respect to an 1850-1900 baseline. To do so, we use the Forster et al. (2023) combined temperature dataset: anthropogenic warming in 2021 is 1.11 °C warmer than the baseline. For cumulative CO₂ emissions from fossil fuels and land use (from 1870 to the end of 2021), we use the Global Carbon Project global emissions dataset starting in 1870. In 2023, cumulative emissions is 675.31 Pg C.

To determine T_{nonCO_2} we use our results from the Flat10_ZEC:

$$T_{\text{nonCO}_2} = \frac{T_{\text{lim}} - T_{\text{hist}} - T_{\text{ZEC}}}{\text{TCRE}} \times \text{TCRE}_{\text{flat10}} \quad (3.3)$$

Here, T_{ZEC} is from

3.4 Discussion & Conclusions

How does the carbon cycle structure in an SCM influence the magnitude and timing of warming in an decarbonization scenarios? Comparing across reduced complexity climate models allows us to quantify structural uncertainty in the climate system. In these idealized emissions scenarios, structural uncertainty emerges in decarbonization. We simulate both cases where emissions drop gradually, as in the esm-bell curve scenario and where emissions drop suddenly. In both cases, differences between SCMs in ZEC are greater than differences in TCRE between models.

This spread is driven from differences in the ways each of the models balances the long-term evolution of carbon uptake and long-term thermal inertia of emissions-driven warming.

How do different model structures allocate carbon to land and ocean sinks, and how do the allocations differ depending on emissions mode (increasing or decreasing)? By allocating carbon to long timescale carbon sinks differently, these SCMs produce these differences and do not produce them in the emissions phase.

What conclusion can we draw about the remaining carbon budget? First, ESMs produce different peak-warming levels, and the peak warming can differ from the long-term temperature response to cumulative emissions.

In this study, we perform a first-step model intercomparison project (MIP) with particular focus on carbon cycle structure in the types of SCMs being used to scope decarbonization pathways. We find that differences in carbon cycle structure can meaningfully influence the timing and amount of expected warming during decarbonization scenarios without changing historical airborne fraction. This underscores an inherent lack of knowledge about the principle dynamics at play in decarbonization scenarios.

Our main conclusion from this work is that structural diversity in carbon cycle representation in these simple climate models leads to a difference in warming response due to differences in how the carbon is allocated across the Earth system. As emissions are increasing, these differences may not influence the overall trend in atmospheric CO₂, but in decarbonization scenarios it changes the climate response. This can be seen most clearly in the flat10_zec experiment and validated in other emissions scenarios, like a Gaussian bell curve of emissions, we see the same divergence when emissions begin to decrease.

This work highlights the need for emissions-forced decarbonization runs in ESM that can help us train emulators to get the right answer for the right reasons (building reliability and insight).

Secondly, it highlights the danger in using only one SCM to project carbon cycle changes in response to mitigation scenarios. A better approach is to use at least two with different approaches to emulation.

Finally it motivates the following questions, which will be addressed in the next chapter:

- (1) What are the timescales of carbon uptake in the long-term, and how different are they from each other in each carbon cycle representation?
- (2) How sensitive are these uptake timescales to choice of parameterization?

In this chapter, we calibrate the analyzed models loosely to the historical record and as a result produce a wide range of climate outcomes. The significance of this is that there are many ways to calibrate these simple models. We deliberately choose to run these models in their default configuration, with minimal calibration to the historical period. While these models are built to be able to be calibrated to various ESMs, choice of calibration can be subjective and lead to different climate outcomes (Sanderson, 2020). By using the default configuration, we attempt to be agnostic to this choice, but are also subject to varying biases in calibration. For that reason, in the following chapter, we take a secondary approach to calibration in order to minimize the influence of this source of spread.

Chapter 4

CHARACTERIZING CARBON SINK RESPONSES TO DECARBONIZATION ACROSS MODEL STRUCTURES

4.1 Motivation and Introduction

[set up importance]

ZEC is a critical metric of our Earth system with policy implications. In combination with TCRE, it quantifies the total amount of global surface warming for a given amount of CO₂ emitted. It can therefore be used to calculate a total carbon budget limit given a global surface temperature threshold. It can also be utilized in different forcing contexts to define total warming.

[set up mystery]

The fact that ZEC is an empirical quantity that emerges from the coupling of climate and the carbon cycle gives it powerful applicability, but makes its physical meaning difficult (a) interpret (b) distinguish from other “committed” warming metrics and (c) characterize with meaningful uncertainty.

- Previous quantification of ZEC relied on experimental setups that included unrealistic termination shocks (in atmospheric CO₂ concentration), and differences in inferred emissions pathways.

- A recent review of the various processes that influence the total magnitude and sign of ZEC that “uncertainty remains high in both ZEC’s sign and magnitude over short- and long-term timeframes, owing to uncertainties in the impact of its constituent parts” (Palazzo Corner et al., 2023).

- New simple model experiments show that ZEC can be partially realized before net-zero emissions in a ramp-down emissions scenario, suggesting that ZEC can be understood to be the deviation from the path-independence of the TCRE relationship than as a measure of the committed warming after reaching net zero.

- Question of whether ZEC/TCRE relation holds in negative emissions scenarios.
- Critical need to understand the physical processes determining the values and balance of ZEC and TCRE in the physical Earth system.

[role of carbon cycle in mystery]

Palazzo Corner et al. (2023) characterize ZEC as a surface energy balance relation in a simplified “zero-dimensional” model between energy emitted and absorbed by the Earth’s lower atmosphere and surface, wherein temperature stabilization is set at the balance of absorption and emission.

As before net-zero emissions, the amount of carbon taken up by land and ocean sinks influences the total energy absorbed by the Earth’s atmosphere and surface and therefore the total radiative balance and resulting temperature.

ZEC can also be understood as the degree to which the TCRE relation is non-linear. In a scenario with a gradual decrease in annual emissions before zero (as is likely will be the real world), the linearity of the TCRE before net-zero is reduced, which can be interpreted as the partial realization of ZEC before net-zero (Koven et al., 2023).

There are many factors that together influence whether ZEC is positive or negative. Processes that lead to more energy being absorbed by Earth’s surface and atmosphere contribute to post-net-zero warming, or positive ZEC, while processes that lead to energy being emitted to space or stored longer in sinks contribute to negative ZEC.

In Palazzo Corner et al. (2023), the authors explain that the pace at which long-timescale processes that are influenced by anthropogenic CO₂-emissions forcing change from their forced state to their unforced state eventually is what determines ZEC. The two major long-timescale processes that are currently being forced by anthropogenic CO₂ are increased ocean heat uptake and increased land and ocean sinks.

Another long-timescale process that will influence ZEC is the long-term release of greenhouse gases from permafrost.

Additionally, the directionality of one of these processes will influence the directionality of the other. For example, if strong carbon sinks persist in strength after emissions reach net-zero, ocean heat uptake may not need to continue to be as strong since CO₂ will be more rapidly removed from the atmosphere.

The rates of change in land and ocean sinks will influence each other in a similar offsetting way. Moreover the ocean and land differ in expected timescales of carbon uptake with cumulative land uptake likely to stabilize within decades after net-zero and cumulative ocean uptake likely to continue growing for centuries (MacDougall et al., 2020)

A underlying challenge is that many processes within each of these long-term Earth processes are not well represented by Earth System Models or not represented at all. For example, carbon release from permafrost thaw, nitrogen limitation of photosynthesis, thermal adaptation in vegetation, robust stomatal responses to atmospheric CO₂, and the mean strength and depth of the Atlantic Meridional Overturning Circulation (AMOC) and bottom water formation in the Southern Ocean, are just a few processes that suffer from poor representation in models and have been shown to have potential to influence

When ZEC is understood as the balance between these many different small and large-scale influences operating at various timescales, it is hard to see how it could truly be zero on th

In chapter 3, we saw that differences in long-term temperature appear between models and persist for hundreds of years in these simple models. The longterm differences in surface temperature, i.e. differences in the post-net-zero long-term balance of energy, become determined between 50-200 years following net-zero in both the ESM bell curve and the flat10 emissions scenario.

[Flat10_ZEC]

- Flat10_ZEC is an emissions scenario that allows us to elegantly quantify the TCRE/ZEC relationship in a model.
- Current efforts are underway to run Flat10 in ESMs. Just announced that CMIP7 will include Flat10_ZEC in its FastTrack experiment list, meaning that

Big overarching question: What is the influence of carbon cycle model structure on ZEC?

4.2 Research Questions

1. How does carbon cycle model structure quantitatively influence the timing of committed warming, as measured by ZEC?

- (a) We use the Flat10 simulations to generate characteristic timescales of carbon removal across models after emissions reach net-zero.

2. How does model structure quantitatively lead to differences carbon cycle response to decarbonization?

- (a) We use the Flat10 simulations to generate characteristic timescales of carbon removal across models after emissions reach net-zero.

3. What aspects of the carbon cycle structure determine each characteristic timescale?

- (a) Answering this question allows the user to calibrate each model while maintaining model structure diversity across the MIP.
- (b) We construct a set of perturbed parameter ensembles (PPEs) specific to each model.
- (c) Performing the PPE allows us to sample across the range of climate responses within each model structure and to further investigate which aspects of the carbon cycle exert the most influence on the carbon cycle response.

4.3 Methods

1. Models For three of the models used in the previous study, we generate a perturbed parameter ensemble that samples across the behavior of the models' carbon cycles.

- (a) **FaIR Default:** We use FaIR's calibrated constrained ensemble, version 1.2.0 (10.5281/zenodo.7112539) to determine the bounds of 47 parameters that determine the model's climate response to emissions. These include 32 parameters that vary species behavior in FaIR. *more about the calibrated, constrained FaIR ensemble described briefly here:*
- (b) In order to produce an initial unconstrained distribution, we use a latin hypercube sampling method to generate a set of 1,000 parameter combinations using upper and lower bounds of the constrained ensemble.

- (c) **FaIR Swann-Deutsch:** As a first step we replace FaIR’s `step_concentration` gas cycle module with the SD carbon cycle model, replacing the temperature inputs with FaIR’s temperature calculation at every timestep. We select five parameters detailed below to perturb the behavior of the SD carbon cycle model. We again use a latin hypercube sampling method to generate a separate ensemble of 1,000 parameter combinations in combination with FaIR’s parameters, as before, sampling within the bounds of FaIR’s constrained ensemble.
- (d) We progressively restrict the bounds of the SD carbon cycle model using the historical simulation.

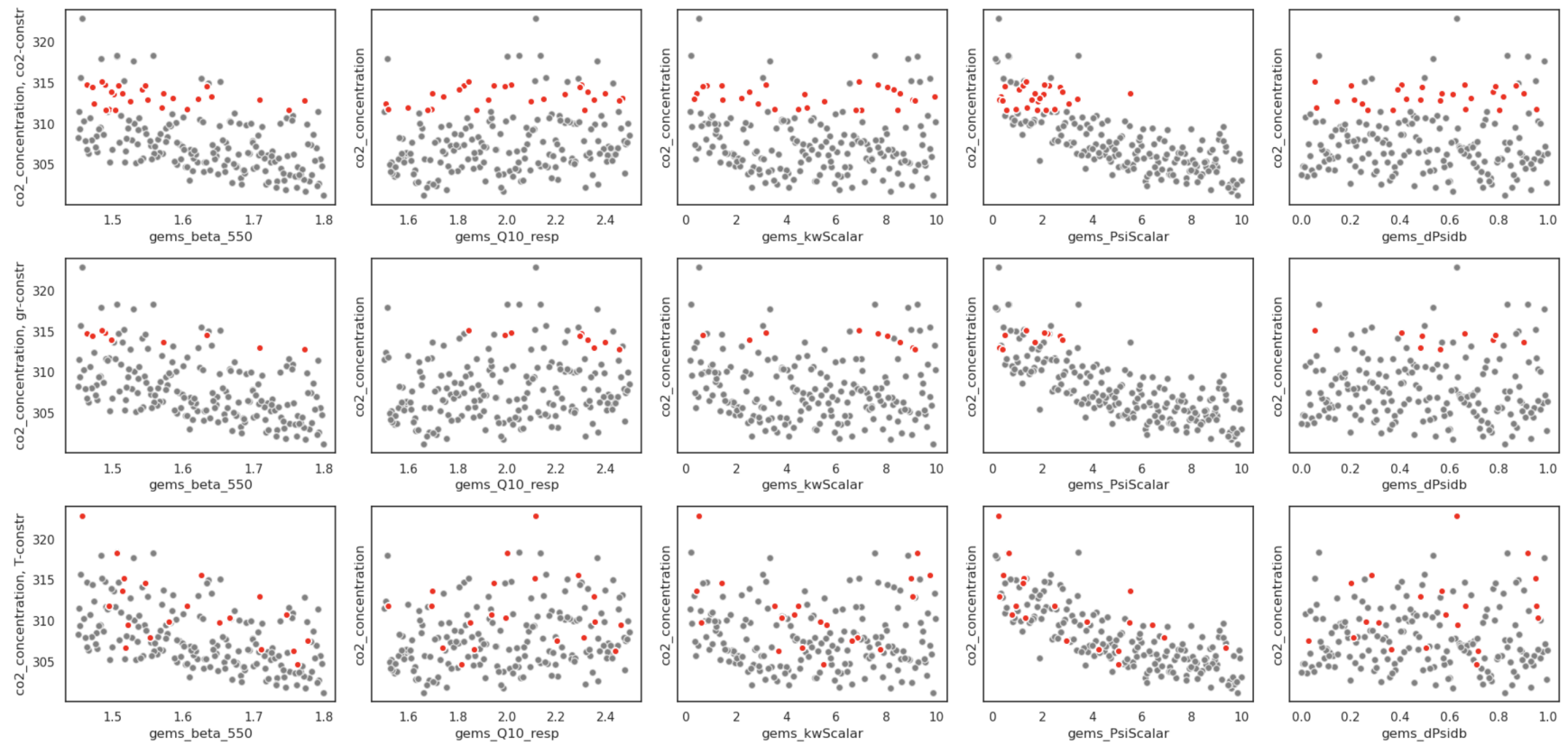


Figure 4.1: Parameters vs. CO₂, GR, and T (TK: will replace with wider beta range, higher figsize and resolution)

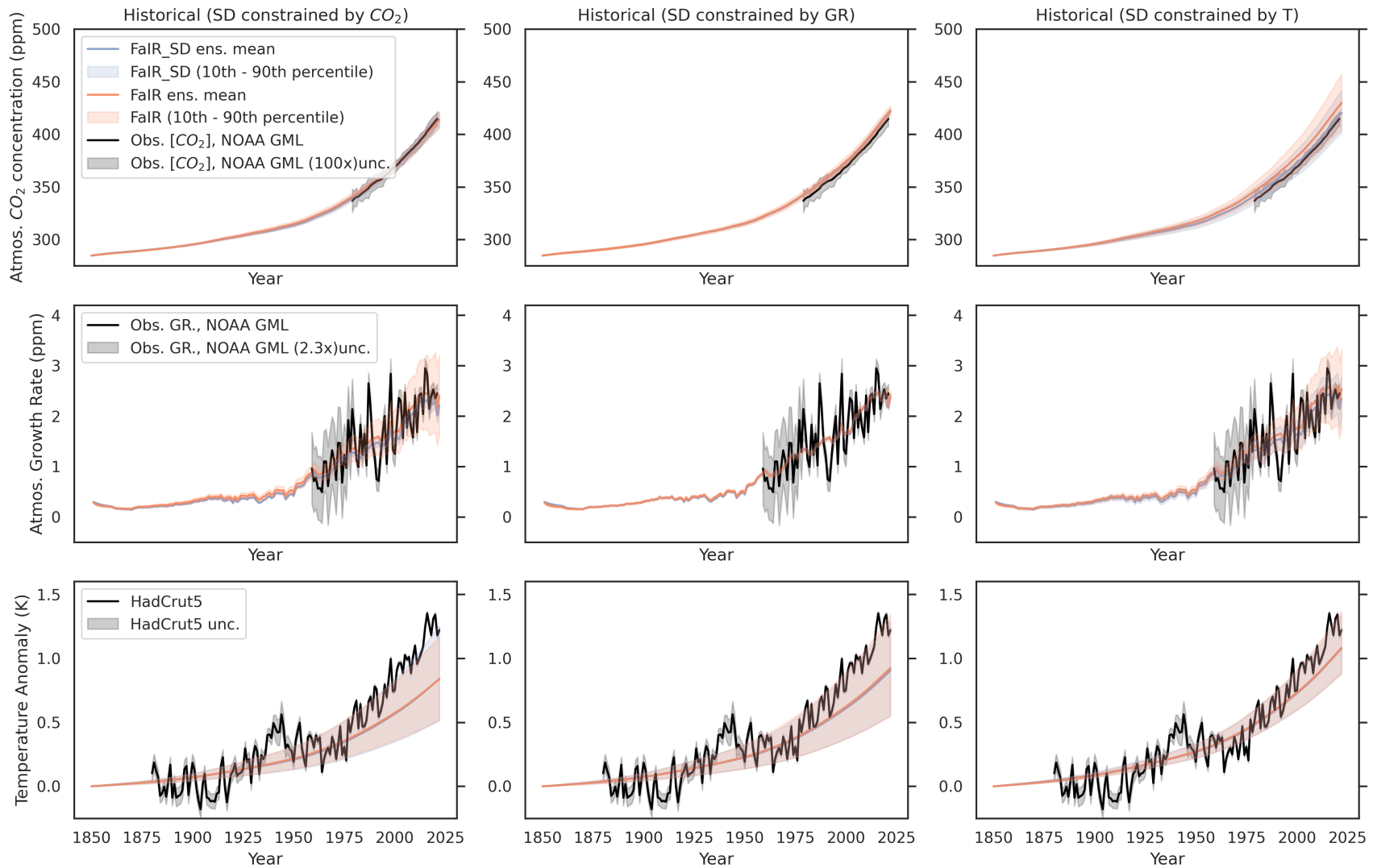


Figure 4.2: Fair and Fair_SD CO₂, GR, and T as constraints

- (e) HECTOR: Version 3.2.0

2. Perturbed carbon cycle parameters in FaIR_SD

- (a) **beta_550**, β_{550} : rate ratio of NPP to change in atmospheric CO₂. In the SD carbon cycle model, it is parameterized as β_{550} , where

$$\beta_{fert} = \frac{\beta_{550} - 1}{\ln(550/365)} \quad (4.1)$$

- (b) **Q10_resp**, Q_{10} : rate ratio of respiration of terrestrial vegetation taking place at temperatures differing by 10 °C or K.

- (c) **kwScalar**, S_{kw} : Scaling factor for piston velocity in units of meters per day, regulating the flux of CO₂ between the ocean and the atmosphere at the surface. Piston velocity in the SD ocean model operates on surface ocean boxes scaled by the fraction without ice, which is 0.9 for all boxes except the low-latitude surface box, which has an open-water fraction of 1. The default value for piston velocity is 3 m/s. For each surface box, i , effective kw is calculated from the scaling factor, the fractional ice coverage, F_{ice} (0.1 in all surface boxes except the low latitude box, where it is 0), and the default piston velocity, kw_d , which is 3 m/s.

$$kw_i = S_{kw} \ kw_d \ (1 - F_{ice_i}) \quad (4.2)$$

$$F_{gasx,i} = kw_i \ A_i \ K_{sol} \ (C_{w,i} - \alpha \ C_a) \quad (4.3)$$

where F_{gasx} is the air-sea gas exchange flux, A is the surface area of each ocean box.

- (d) **PsiScalar**, S_ψ : Scaling factor for circulation
- (e) **dPsidb**, $d\psi/db$: Climate response of ocean circulation

3. Calibrating and constraining the ensembles

- (a) CO₂: 100 × uncertainty in NOAA GML reported global mean CO₂.
- (b) GR 2.5 × uncertainty in NOAA GML reported CO₂ growth rate since

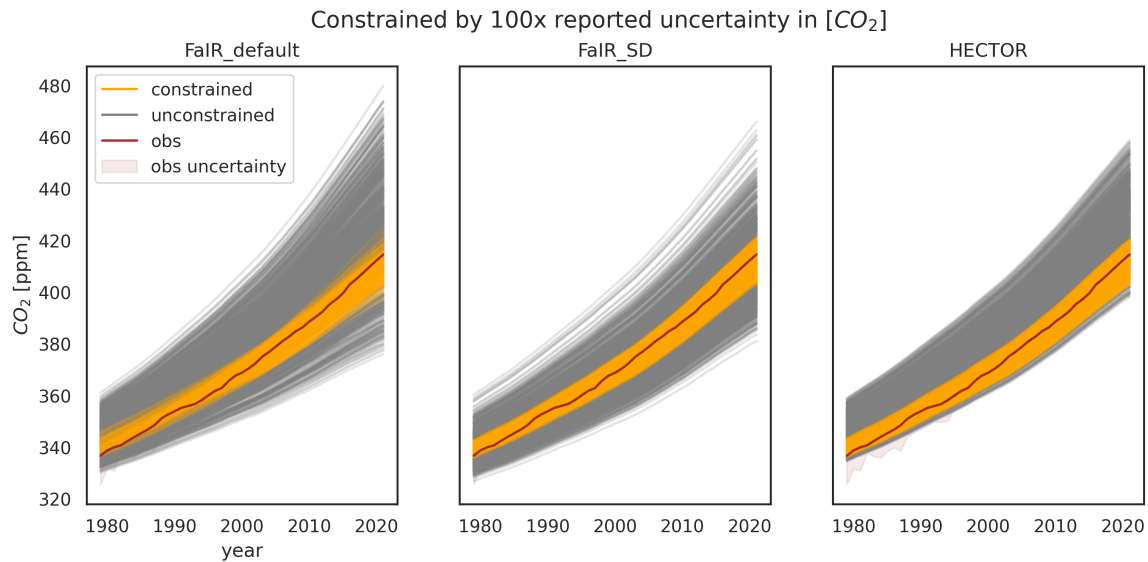


Figure 4.3: GCP Historical CO_2 concentration as a constraint for FaIR, FaIR_SD and HECTOR

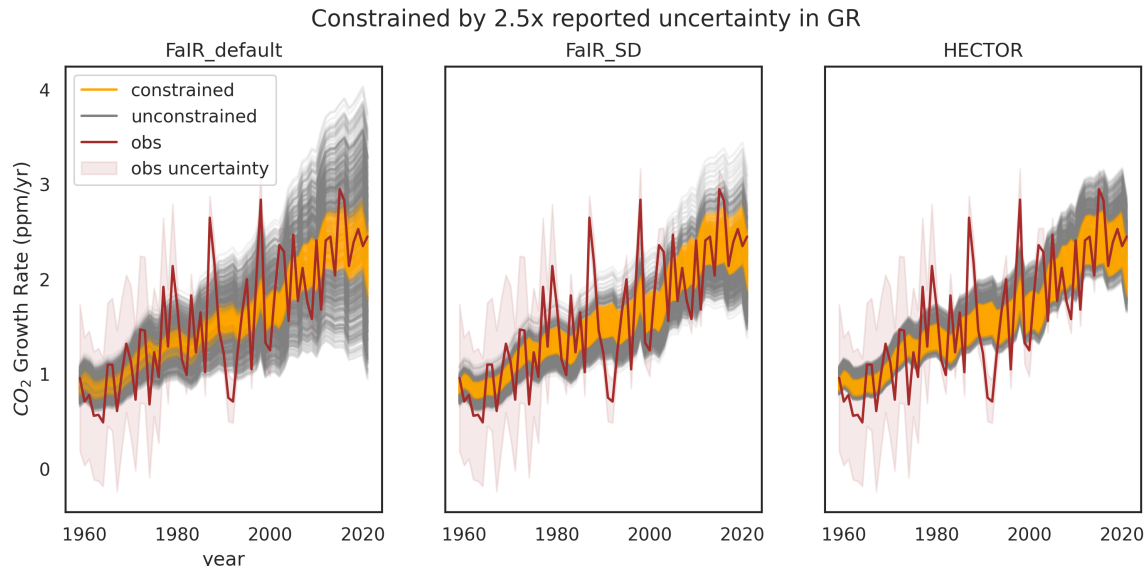


Figure 4.4: GCP Historical CO_2 growth rate as a constraint for FaIR, FaIR_SD and HECTOR

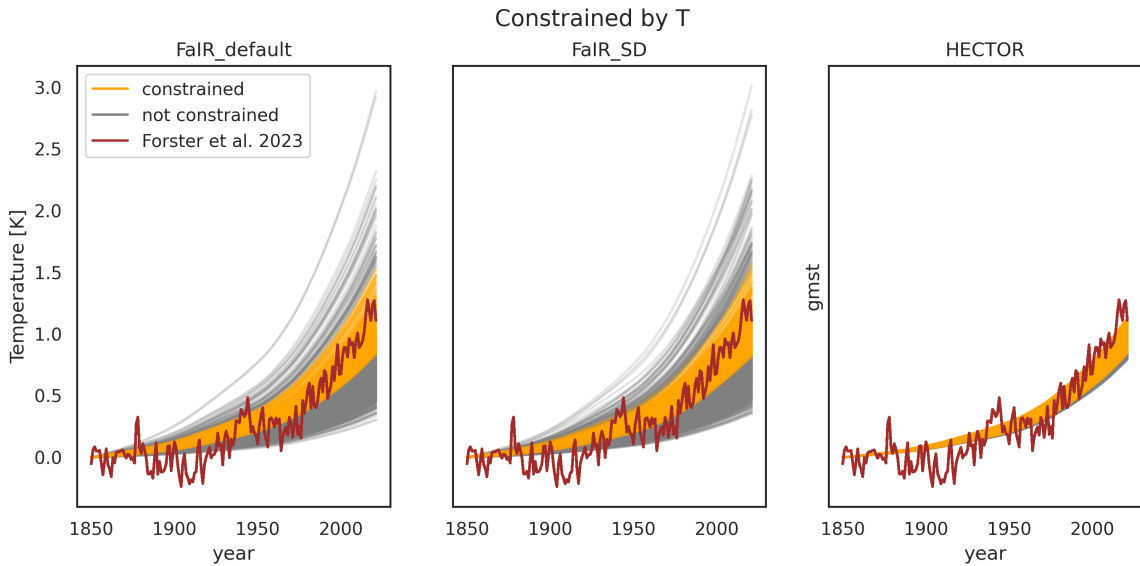


Figure 4.5: GCP Historical temperature change as a constraint for FaIR, FaIR_SD and HECTOR

(c) Temperature change, compared to record from Forster et al. (2023)

4. Simulations

(a) Global Carbon Budget Historical Emissions dataset [citation]

(b) Flat10 ZEC (and what we can learn from Flat10)

Flat10 ZEC

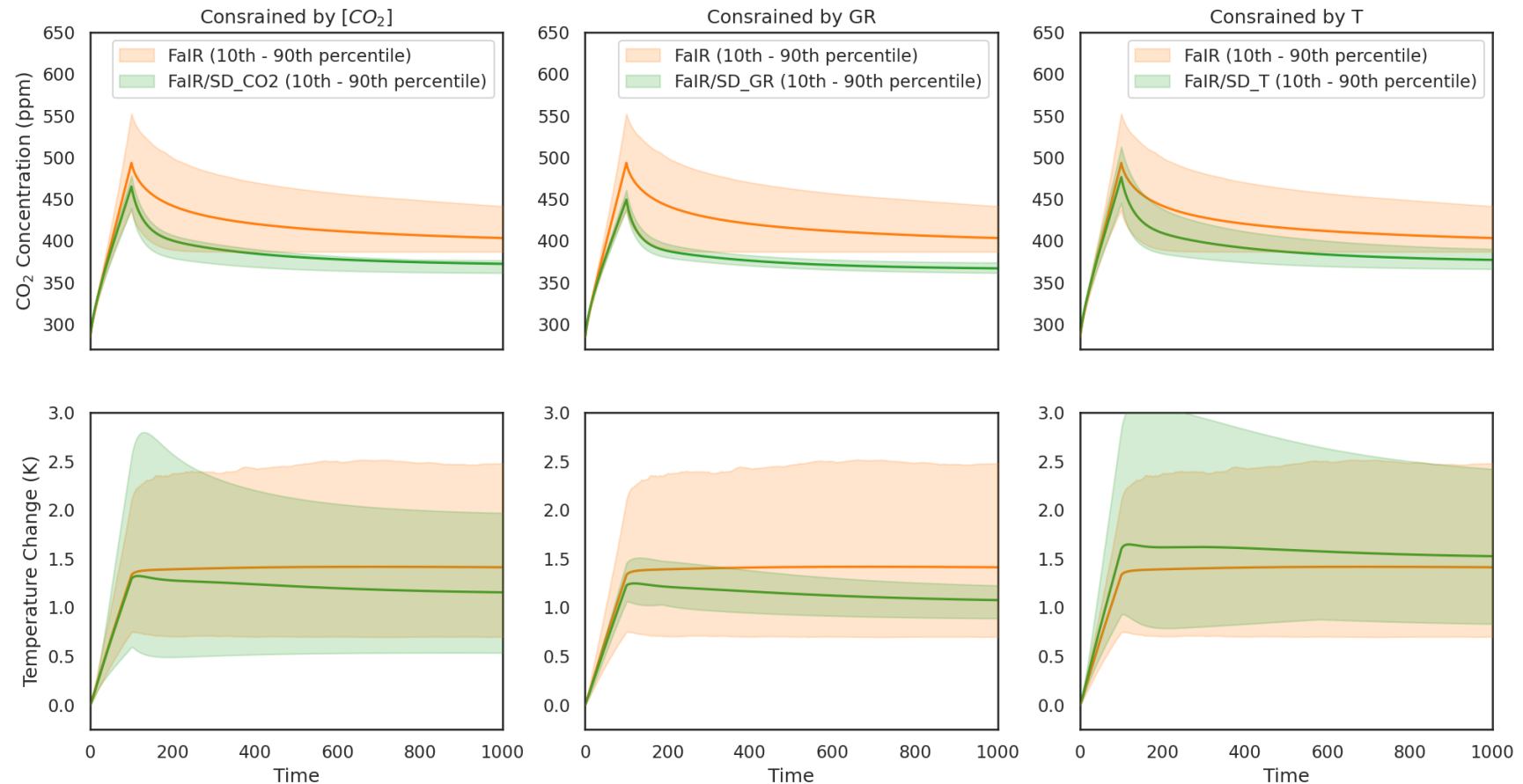


Figure 4.6: Flat10 CO₂ and T for Fair & ZEC. (TK: add HECTOR)

4.4 Results

1. Carbon pools:

- (a) FaIR vs. FaIR_SD: If we interpret FaIR's four timescales of removal as representative of different carbon sinks we can compare the allocation carbon between the different pools (Millar et al., 2017).

2. **TCRE**: consistent across models. No significant difference between models in TCRE (Figure 4.8).

3. **ZEC**: differences across models

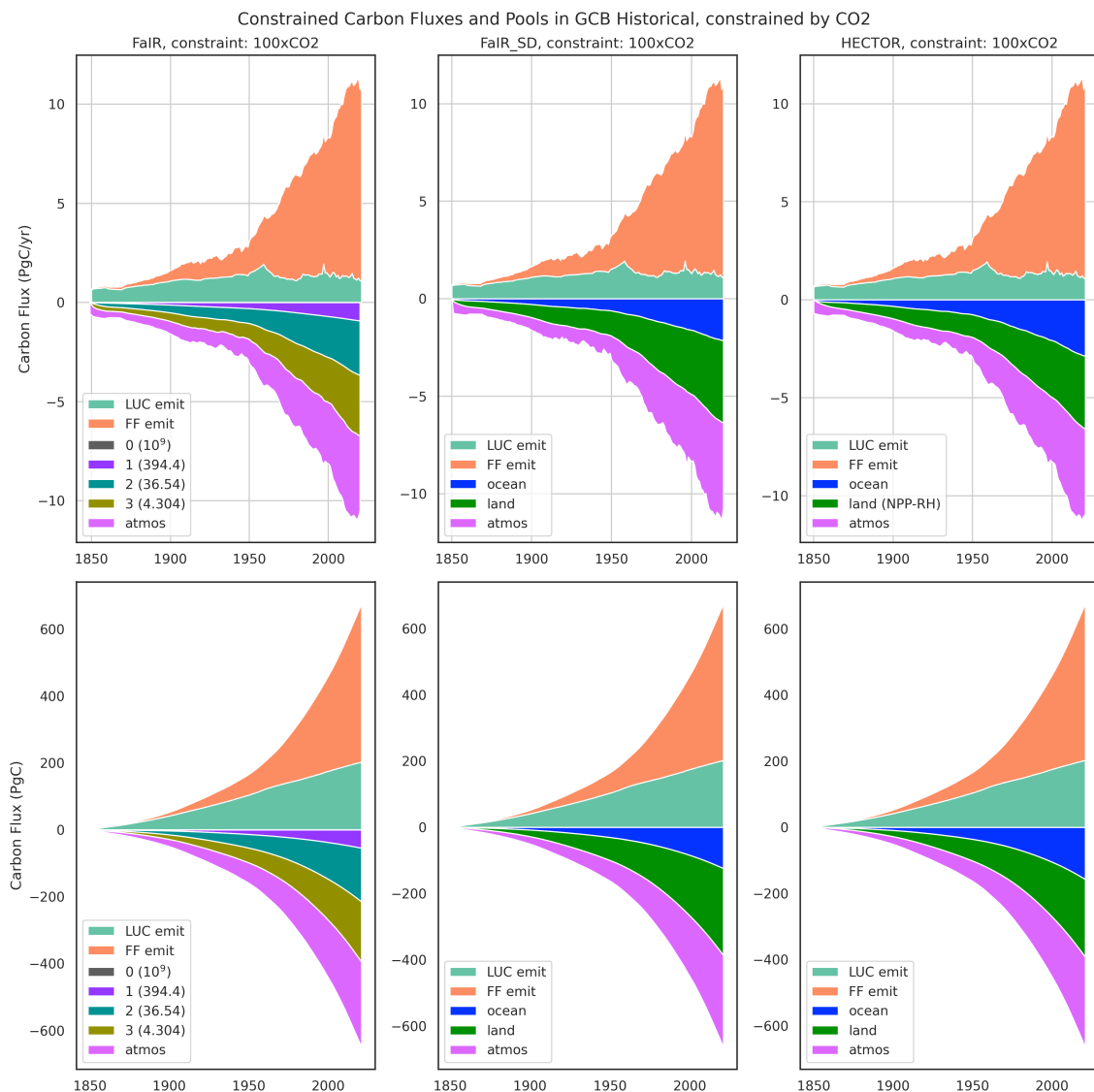


Figure 4.7: GCB Historical carbon fluxes

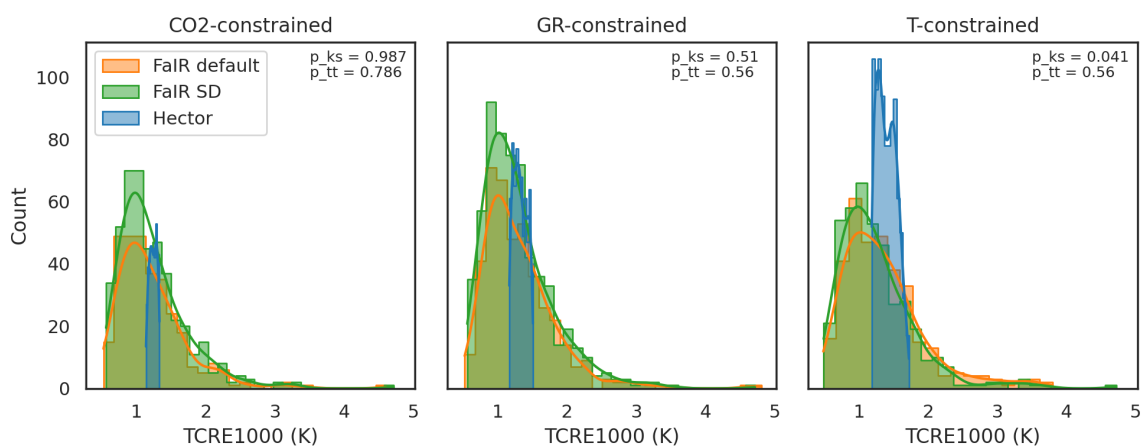


Figure 4.8: Distributions of Flat10_ZEC TCRe1000 for FaIR, FaIR_SD, HECTOR

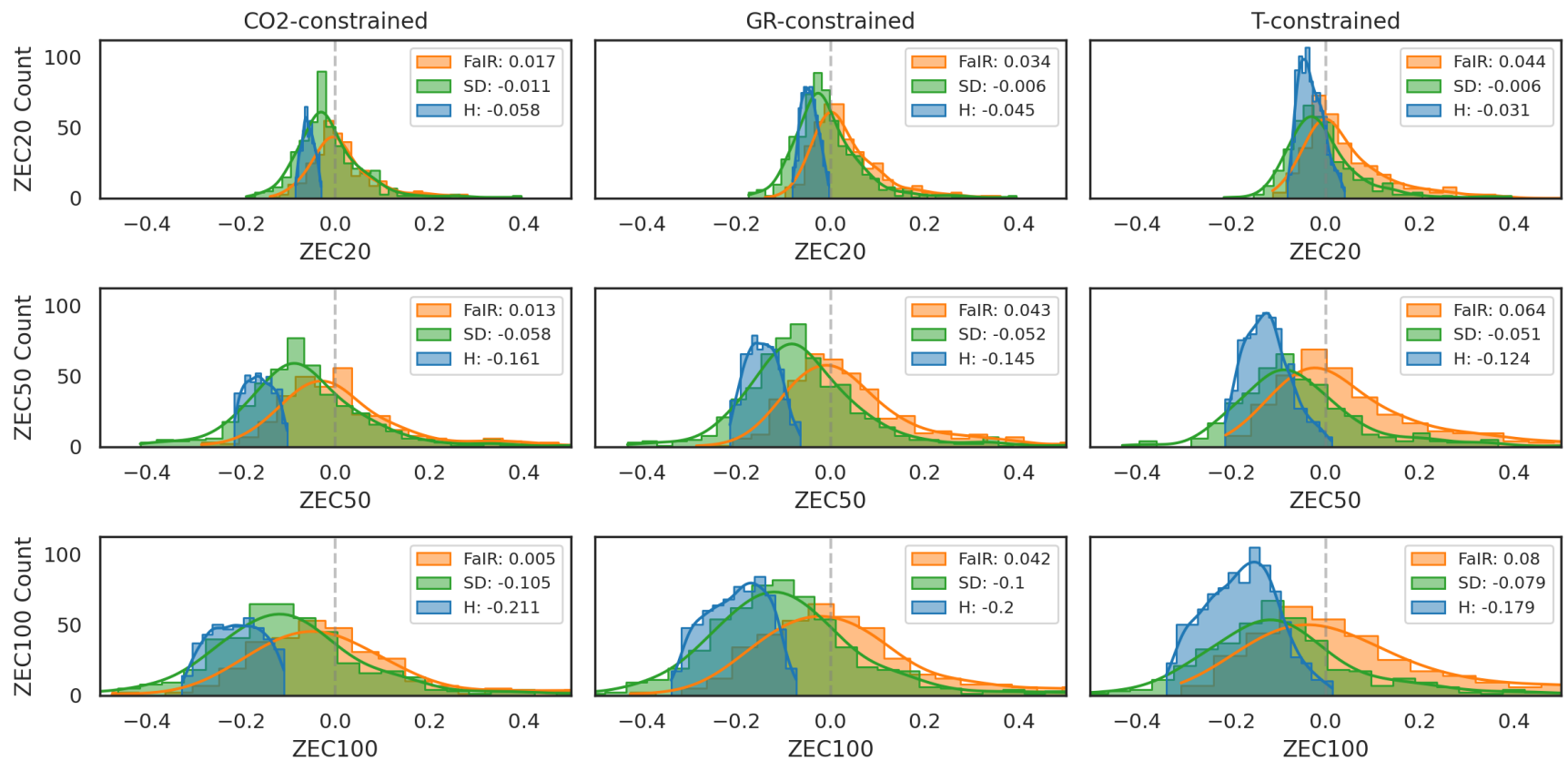


Figure 4.9: Histogram of ZEC20, ZEC50, ZEC100 for all FaIR, FaIR_SD, HECTOR

4. Timescales of sinks:

- 5. To explain the differences in ZEC, we fit a set of increasing order exponential memory functions to the different models' carbon cycle responses to identify divergences in timescales of carbon removal.
- 6. We compare the FaIR_SD and HECTOR land and ocean carbon cycle timescales to identify which aspects of the carbon cycle contribute most to the differences in ZEC and offer some interpretations for FaIR's near-zero ZEC.

- (a) **Single Exponential memory function for FaIR_SD and HECTOR:** We define a simple exponential memory function that relates sink strength to prior emissions,

$$S(t) = \int_0^t E(t_e) a e^{-\frac{(t-t_e)}{\tau}} dt_e \quad (4.4)$$

- (b) We first fit the memory function to the FaIR_SD land sink during the Flat10 emissions phase (year 0 through 99) and apply it to the full flat Flat10 ZEC time period (total run length of 1110 years). This fit is denoted as `emissions` in Figures
- (c) We then fit the function to emissions time series and sink response for the entire simulation period.

- (d) **Multi Exponential memory function for FaIR SD and HECTOR:** We also fit a 2-, 3-, and 4-timescale memory model fit to Flat10 ZEC sinks described as follows:

$$S(t) = \int_0^t E(t_e) \left(a_1 e^{-\frac{(t-t_e)}{\tau_1}} + a_2 e^{-\frac{(t-t_e)}{\tau_2}} \right) dt_e \quad (4.5)$$

$$S(t) = \int_0^t E(t_e) \left(a_1 e^{-\frac{(t-t_e)}{\tau_1}} + a_2 e^{-\frac{(t-t_e)}{\tau_2}} + a_3 e^{-\frac{(t-t_e)}{\tau_3}} \right) dt_e \quad (4.6)$$

$$S(t) = \int_0^t E(t_e) \left(a_1 e^{-\frac{(t-t_e)}{\tau_1}} + a_2 e^{-\frac{(t-t_e)}{\tau_2}} + a_3 e^{-\frac{(t-t_e)}{\tau_3}} + a_4 e^{-\frac{(t-t_e)}{\tau_4}} \right) dt_e \quad (4.7)$$

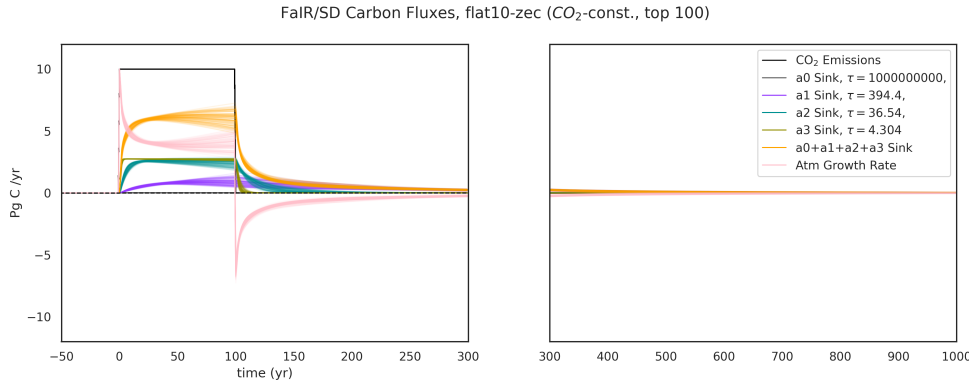
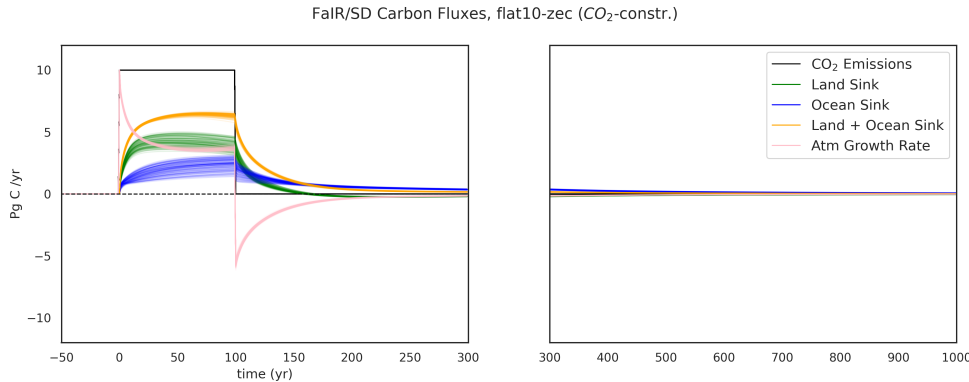
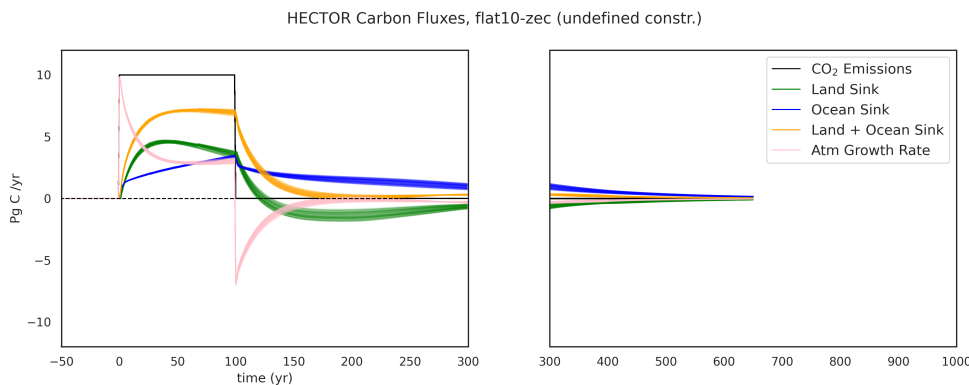
(a) FaIR carbon fluxes for 100 ensemble members constrained by CO_2 . (TK correct title)(b) FaIR_SD carbon fluxes for 100 ensemble members constrained by CO_2 .(c) HECTOR carbon fluxes for 100 ensemble members constrained by CO_2 .

Figure 4.10: Flat10_ZEC carbon fluxes of sink and atmosphere pools for 100 ensemble members constrained by CO_2 .

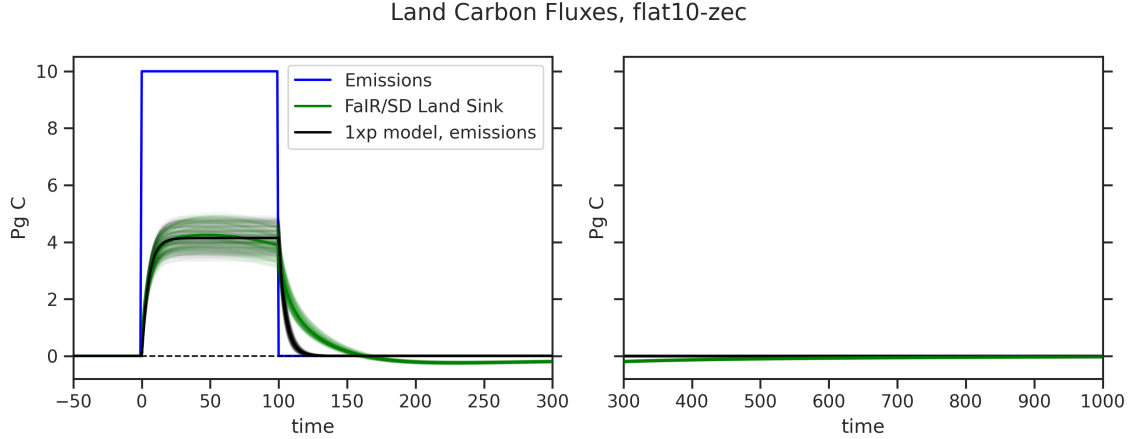


Figure 4.11: FaIR_SD Land C Fluxes, Single Exponential fit using emissions and land sink response over 100 years of emissions

Means of each curve-fit parameter set (τ_i and a_i) for FaIR_SD are given in Table 4.2

- (e) **Land sink responses in FaIR_SD.**
- (f) **Ocean sink responses in FaIR_SD.**
- (g) **Total sink responses in FaIR_SD.**

7. *TK: Timescales of sinks in HECTOR and FaIR. We will apply the same memory function to HECTOR and FaIR to compare curve-fit τ parameters between models for each memory function. Note that FaIR is built using timescales of removal, and we can compute the α lifetime modifier as an output at each timestep. We will then compare the mean effective timescales of removal in FaIR to the curve-fit timescales.*
8. *Distributions of timescales: Figure 4.21 shows the distributions of the single-exponential memory functions of the land, ocean, and total sinks. Figure 4.23 shows the distributions of the double-exponential memory functions of the land, ocean, and total sinks compared to the single-exponential τ parameters.*

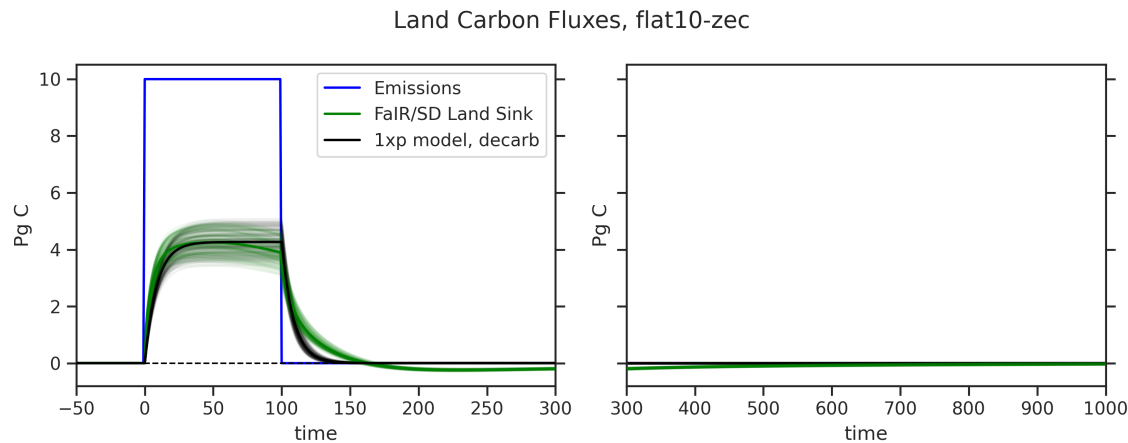


Figure 4.12: FaIR_SD Land C Fluxes, Single Exponential fit using emissions and land sink response over entire simulation time period

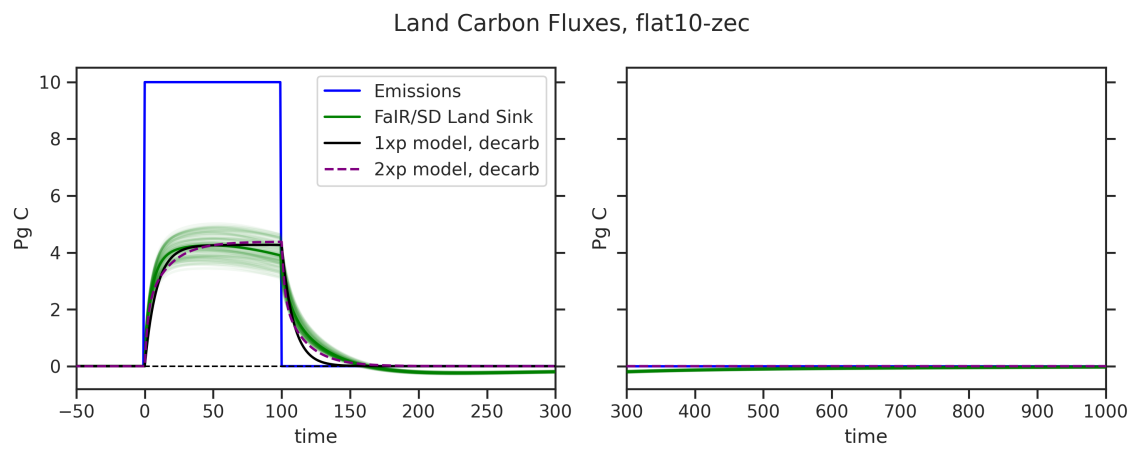


Figure 4.13: FaIR_SD Land C Fluxes, Double Exponential fit using emissions and land sink response over entire simulation time period

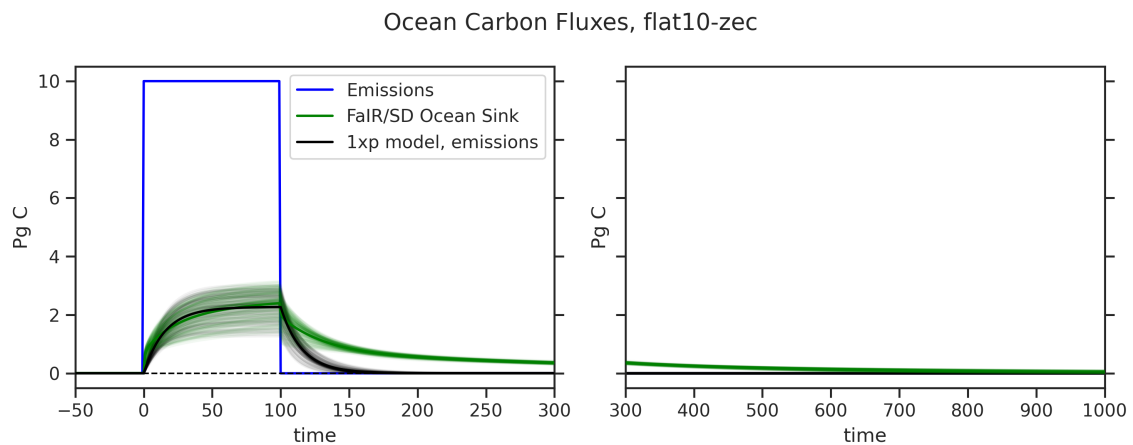


Figure 4.14: FaIR_SD Ocean C Fluxes, Single Exponential fit using emissions and ocean sink response over 100 years of emissions

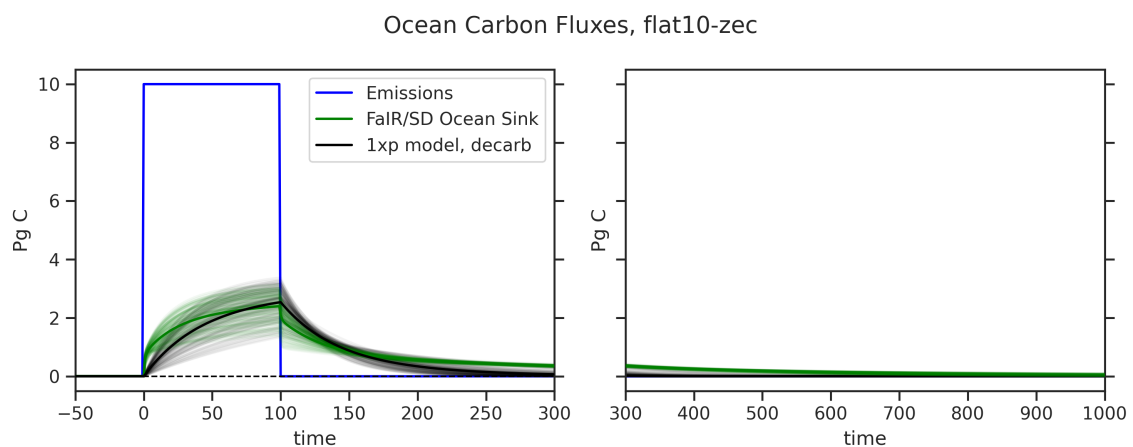


Figure 4.15: FaIR_SD Ocean C Fluxes, Single Exponential fit using emissions and ocean sink response over entire simulation time period

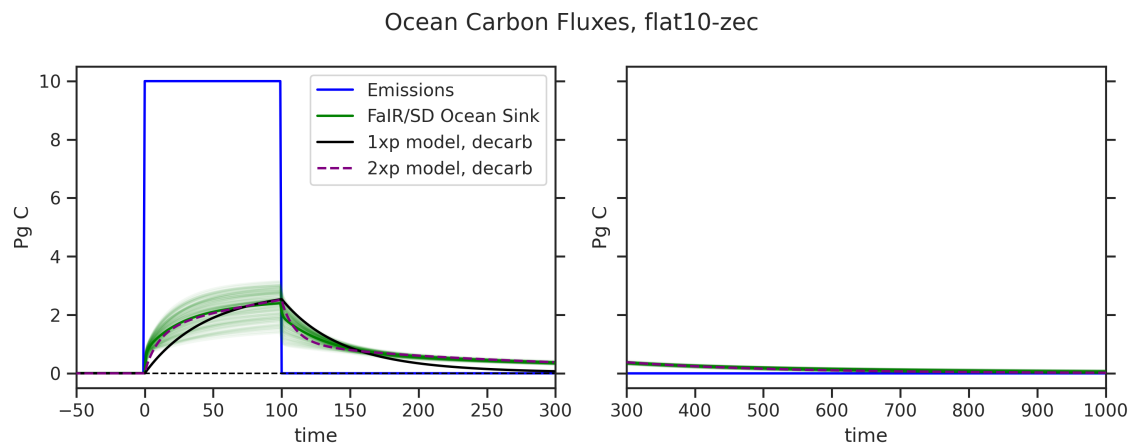


Figure 4.16: FaIR_SD Ocean C Fluxes, Single Exponential fit using emissions and ocean sink response over entire simulation time period

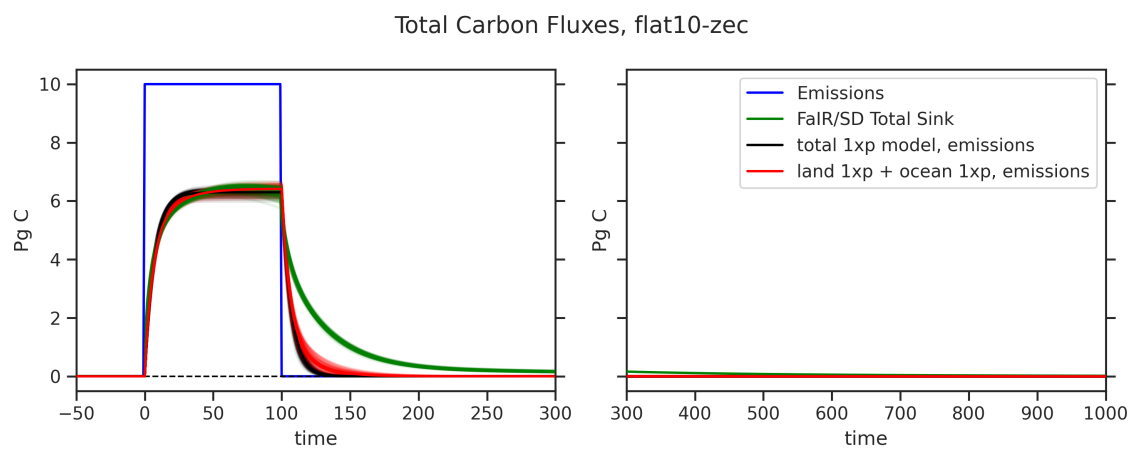


Figure 4.17: FaIR_SD Total Sink C Fluxes, Single Exponential fit using emissions and sink response over 100 years of emissions

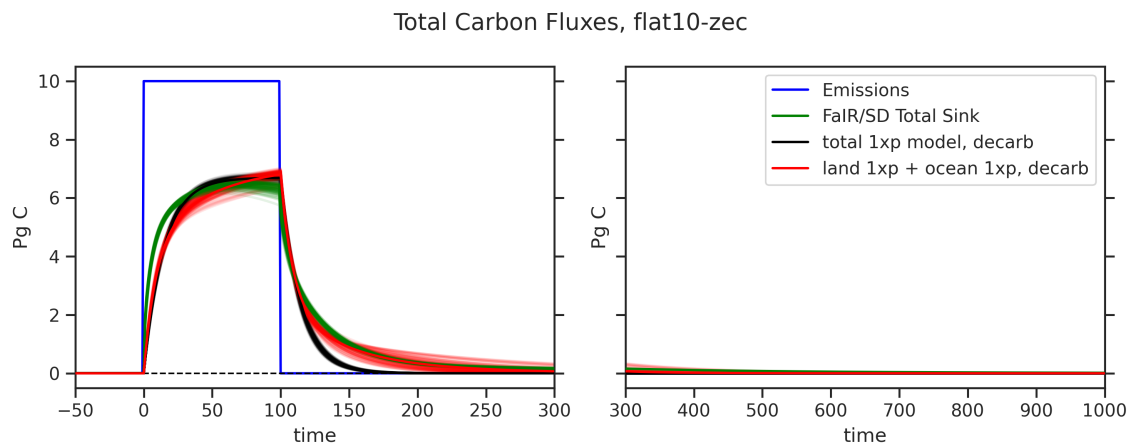


Figure 4.18: FaIR_SD Total Sink C Fluxes, Single Exponential fit using emissions and sink response over entire simulation time period

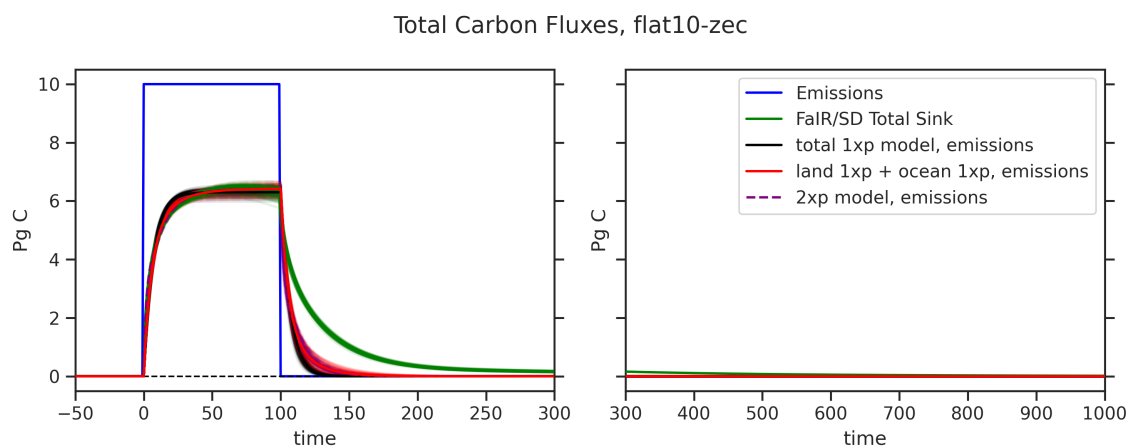


Figure 4.19: FaIR_SD Total Sink C Fluxes, Double Exponential fit using emissions and sink response over 100 years of emissions

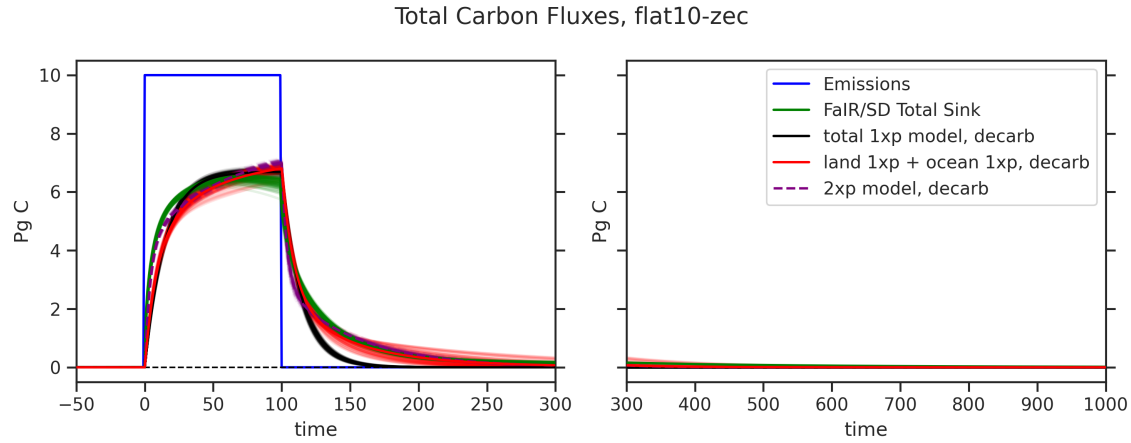


Figure 4.20: FaIR_SD Total Sink C Fluxes, Double Exponential fit using emissions and sink response over entire simulation time period

FaIR Default	a0	a1	a2	a3	Total
1x Exp: emis.	$\tau_1 = X,$ $a_1 = X$	$\tau_1 = X, a_1 = X$			
1x Exp: total	$\tau_1 = X,$ $a_1 = X$	$\tau_1 = 1.3e4,$ $a_1 = 5.4e-10$			
2x Exp: total	X	X	X	X	$\tau_1 = 3.52, a_1 = 0.17$ $\tau_2 = 117.6, a_2 = 1.9e-3$
3x Exp: total	X	X	X	X	$\tau_1 = 1.73, a_1 = 0.24$ $\tau_2 = 8.37, a_2 = 0.03$ $\tau_3 = 140.4, a_3 = 1.5e-3$
4x Exp: total	X	X	X	X	$\tau_1 = 1.66, a_1 = 0.24$ $\tau_2 = 7.58, a_2 = 0.03$ $\tau_3 = 121.94, a_3 = 1.6e-3$ $\tau_4 = -1.7e8, a_4 = 2.7e-5$

Table 4.1: FaIR_SD timescales for each memory function and sink. These are calculated from the to 100 ensemble members constrained from CO₂.

FaIR_SD	Land	Ocean	Total
1x Exp: emissions	$\tau_1 = 4.96, a_1 = 0.9$	$\tau_1 = 15.68, a_1 = 0.02$	$\tau_1 = 14.38, a_1 = 0.05$
1x Exp: total	$\tau_1 = 8.61, a_1 = 0.05$	$\tau_1 = 54.87, a_1 = 0.01$	$\tau = 6.91, a_1 = 0.1$
2x Exp. total	$\tau_1 = 2.05, a_1 = 0.13$ $\tau_2 = 15.16, a_2 = 0.02$	$\tau_1 = 8.98, a_1 = 0.03$ $\tau = 219.08, a_2 = 0.0$	$\tau_1 = 3.86, a_1 = 0.14$ $\tau_2 = 70.08, a_2 = 0.0$
3x Exp: total	$\tau_1 = TK, a_1 = TK$	$\tau_1 = TK, a_1 = TK$	$\tau_1 = 2.54, a_1 = 0.18$ $\tau_2 = 32.35, a_2 = 0.01$ $\tau_3 = 275.06, a_3 = 0.0$
4x Exp: total	$\tau_1 = TK, a_1 = TK$	$\tau_1 = TK, a_1 = TK$	$\tau_1 = 0.64, a_1 = 0.73$ $\tau_2 = 8.14, a_2 = 0.04$ $\tau_3 = 72.1, a_3 = 0.0,$ $\tau_4 = -1.38 \times 10^9, a_4 = 0.0$

Table 4.2: FaIR_SD timescales for each memory function and sink. These are calculated from the to 100 ensemble members constrained from CO₂.

9. We find that differing carbon cycle structures, even when constrained to the same response to historical emissions to concentrations produce differing timescales of removal, a robust response across different ways of constraining the ensemble (Figure 4.9).
10. In the first-order memory function, we find that a curve-fits for timescales of removal produce the largest timescales for HECTOR, shorter for FaIR_SD and shortest for default FaIR.
11. When we fit higher order exponential curves to FaIR, FaIR_SD and HECTOR, the largest differences emerge between the longest timescales of removal.
12. In higher order exponential curves, shorter timescales of removal are
13. *TK: metrics of fit of memory function parameters to each model's sink*
14. *TK: ESM carbon fluxes, TCRe and ZEC evolution context*

4.5 Conclusion

1. Simple models still have structural uncertainty that cannot be eliminated by parametric filtering
2. Land parameters exert strong influence on land carbon sink dynamics in model structures that explicitly represent land. Even in a very limited parametric space, the trade-offs between beta and Q_{10} prevent present a limitation to strict calibration.

4.6 Discussion

1. Potential future avenues for continuation of this work:
 - (a) We cannot fairly compare the response of emissions-regime carbon sinks to decarbonization-regime carbon sinks because the longer timescales of change do not emerge if only 100 years is given. (This is also a limitation of the Joos et al. (2013) modeling

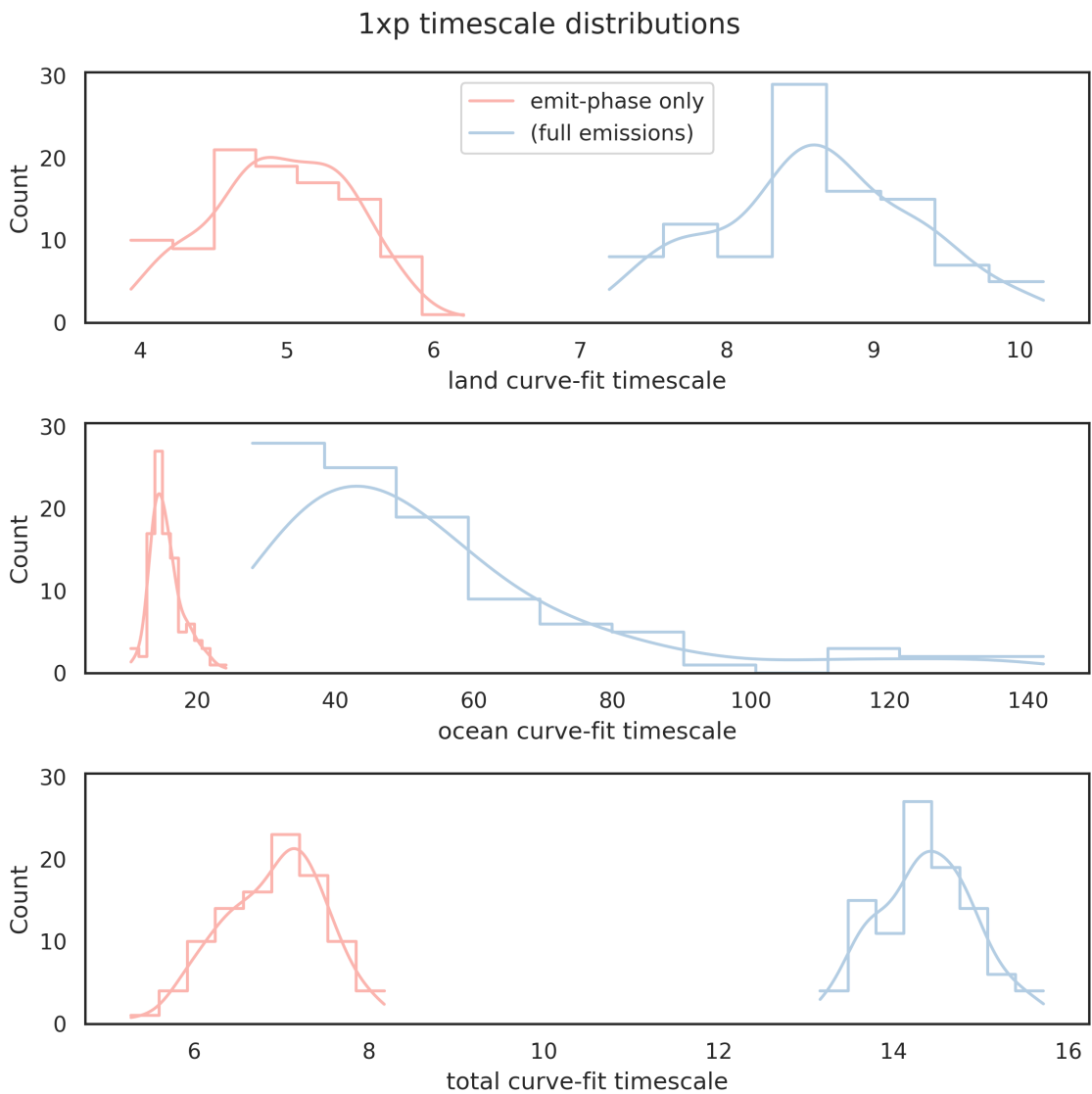


Figure 4.21: Distribution of timescales in single exponential curves.

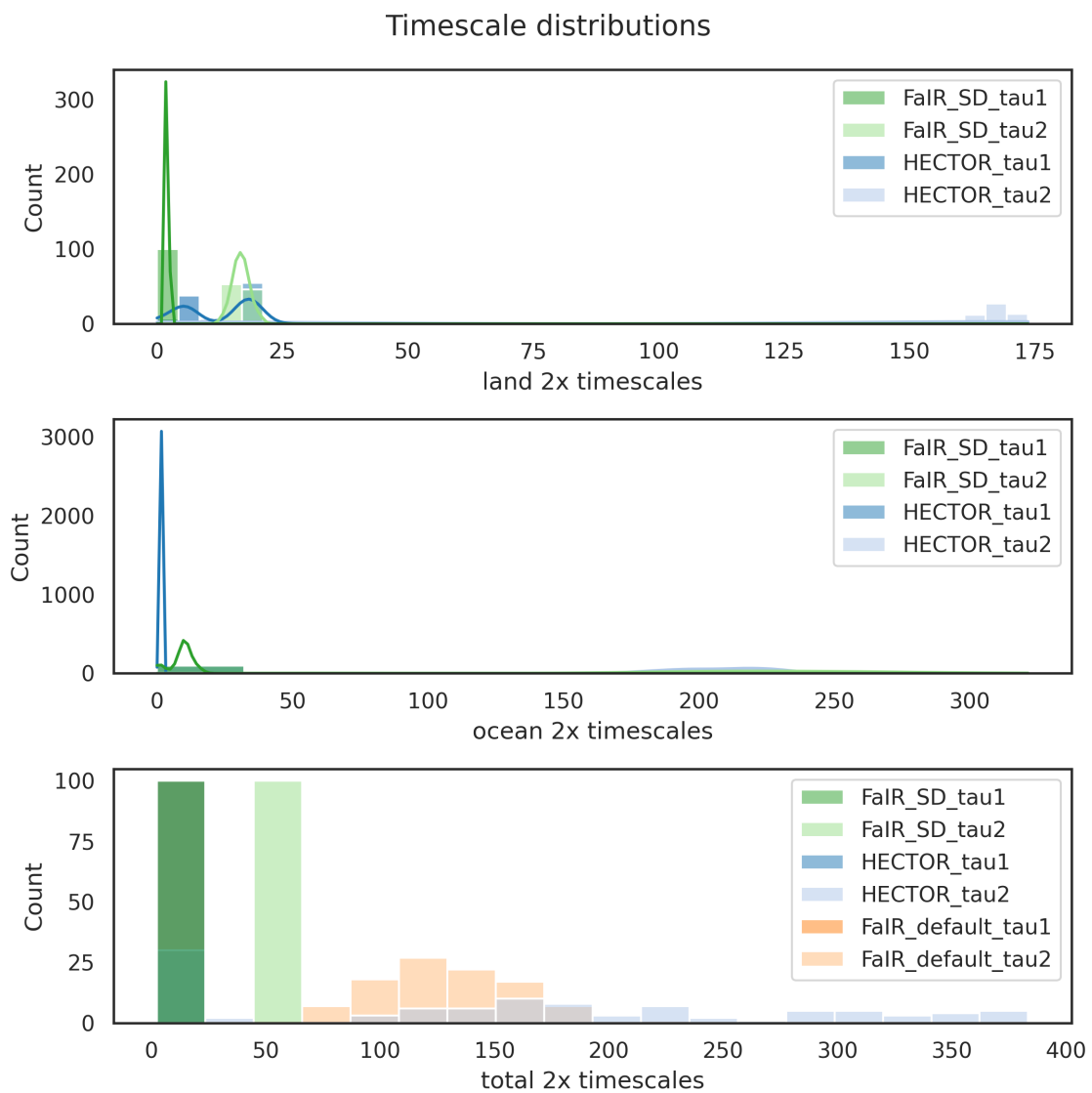


Figure 4.22: Distribution of timescales in double exponential curves.

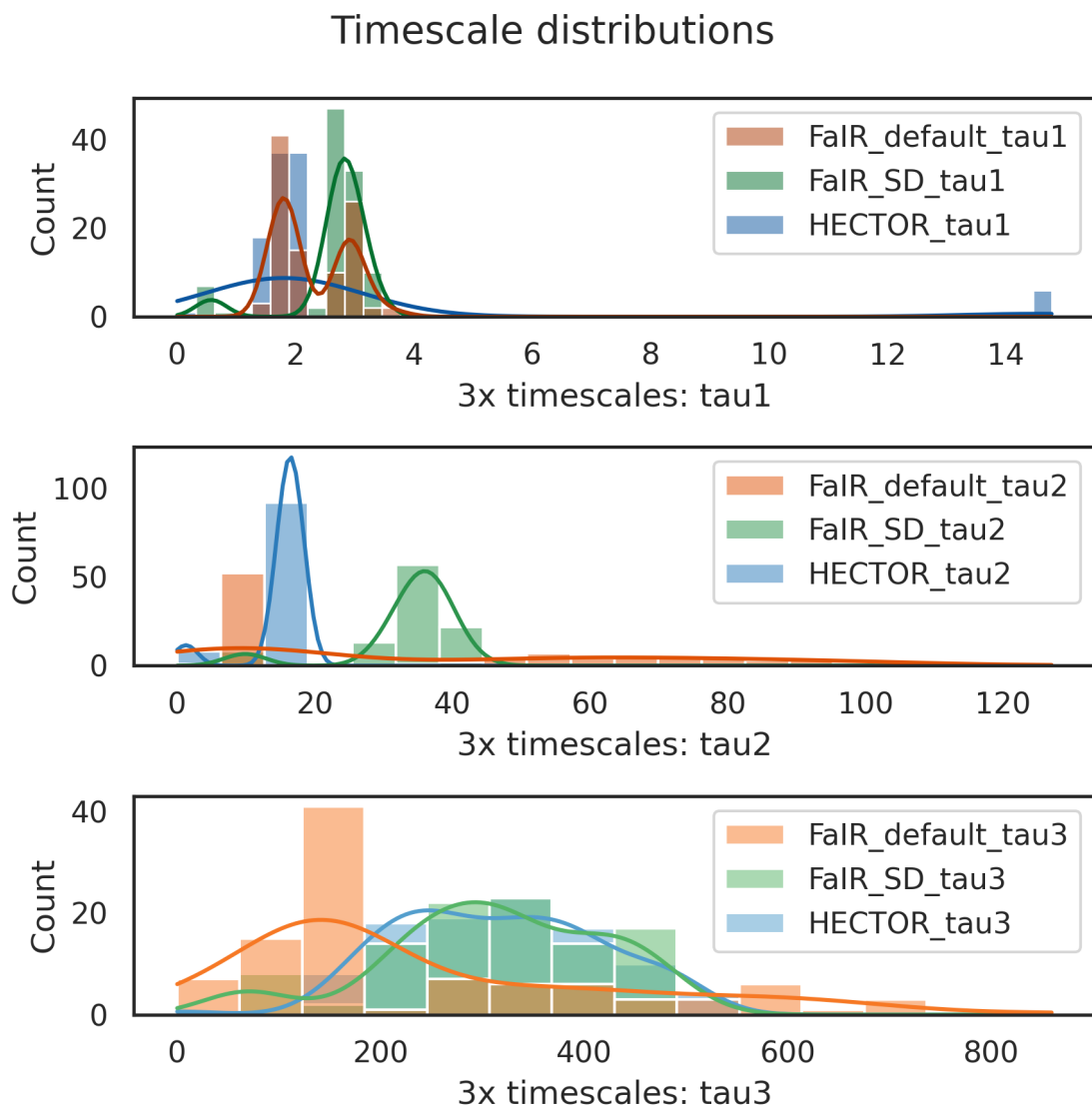


Figure 4.23: Distribution of timescales in triple exponential curves.

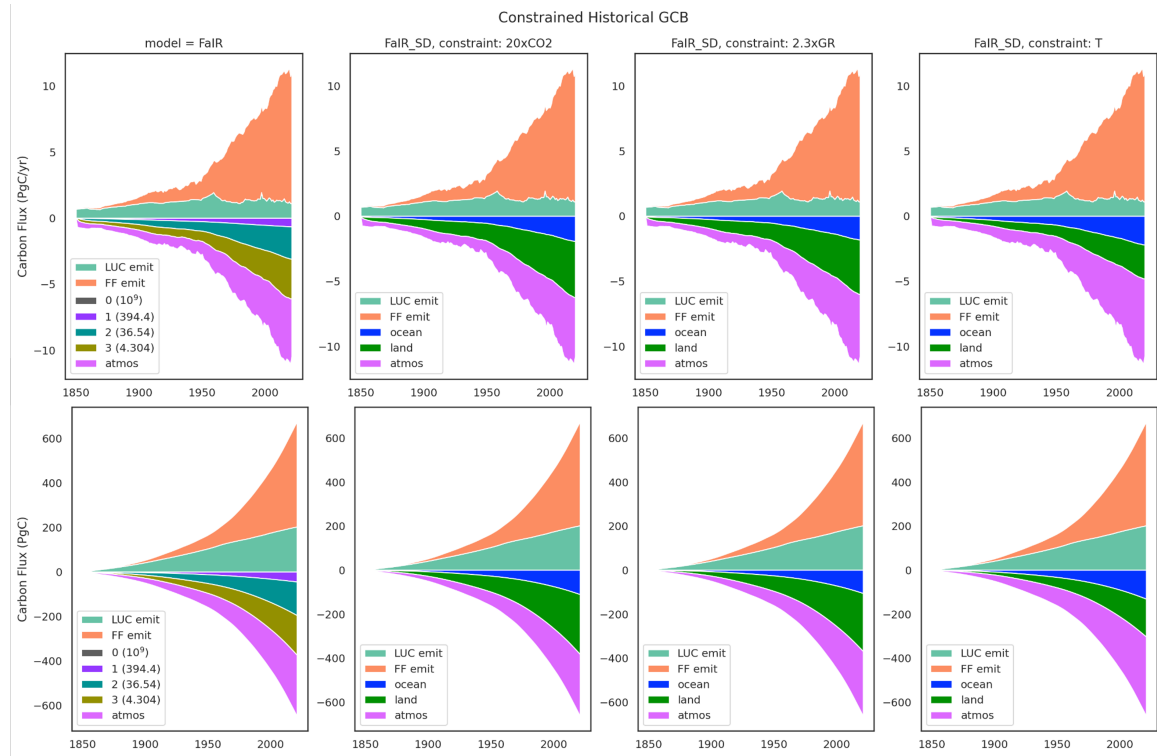


Figure 4.24: Carbon budgets using different constraints for Fair-SD

study that only uses 300 years of simulation for some model runs, which are then used to determine input lifetimes in Fair.) Future scenarios that compare, for example, a 1000 PgC pulse of carbon to the Flat10 ZEC and a 1 PgC/yr for 1000 years emissions scenario to investigate differences between sink responses during the emissions-phase vs. decarbonization-phase.

- (b) More models (other kinds of models).
- (c) Comparison with coming CMIP7 ESM Flat10 runs.

Chapter 5

CONCLUSIONS AND FUTURE WORK

Conclusions

In two divergent climate settings, we show that habitability is sensitive to the behavior of processes at the interface between the atmosphere and surface. In particular, the specific response of processes on land to atmospheric forcing exerts a strong control on the overall climate state.

Biophysical and biogeochemical responses of land to climate make large differences for habitability of Earth in two very different contexts.

In chapter 2, we show that the overall habitability of a Snowball climate on Earth is sensitive to bare ground surface albedo. This sensitivity is due to the way that the land surface responds to a change in albedo in its exchange of water and energy.

Future Work

An crucial difference between the definitions of habitability during Snowball Earth and future climate is the influence of human influence on the climate state.

Appendix A

PENETRATION OF A SEA GLACIER DOWN A NARROW BAY

A sea glacier entering a long narrow bay with length L_{bay} could be expected to have some spatial and temporal variability in flow speed and thickness, due for example to obstructions such as islands, shoals, or narrows in the bay; however, we can look beyond those possibly minor variations to find characteristic numbers describing important aspects of long, straight, narrow bays, their sea glaciers, and their climates.

We use a coordinate system $[x, y, z]$, with x and y horizontal; x can be aligned along the axis of the bay, with $x = 0$ at the bay mouth, and z is vertical. The corresponding velocity components are $[u, v, w]$.

If a bay has a roughly uniform width W , then flow $v(x, y)$ transverse to the long axis of the bay is small.

A sea glacier is floating, so except on shoals, there is no basal friction, and the flow speed $u(x, y, z)$ along the bay can be treated as independent of depth, i.e. as $u(x, y)$.

Nye (1965) found a solution appropriate for $u(x, y)$ for floating ice in a uniform deep narrow channel or deep bay, and Campbell et al. (2011) averaged Nye's solution across the bay to find its average value $\bar{u}(x)$,

$$\bar{u}(x) = \frac{W}{2} \frac{A(x) k(x)^n}{n + 2} \quad (\text{A.1})$$

Temperature (and therefore ice softness) is incorporated in $A(x)$, resistive side-wall drag is incorporated in $k(x)$, and $n \cong 3$ is the exponent in the Glen nonlinear flow law for ice (Glen, 1955).

Thomas (1973) and Sanderson (1979) showed that $\bar{u}(x)$ varies little in x , so following Campbell et al. (2011) we set \bar{u} to be a constant, which we take as a characteristic velocity u_{char} .

Ablation rate $b(x)$ (m/s) depends on sublimation on the upper surface and melting at the

base; however, Goodman (2006) found that in the tropics on Snowball Earth, basal melting was insignificant relative to surface sublimation. Although sublimation rate can vary along a long narrow bay, following Campbell et al. (2011), we can define a characteristic ablation rate b_{char} as the average value of $b(x)$ along the centerline of the bay ($b < 0$ for sublimation).

A characteristic ice thickness H_{char} is set by the offshore sea glacier, which enters the bay and moves from its mouth at $x = 0$ to the glacier terminus at $x = L_{glac}$ where the ice thickness reaches zero. Time t_{flow} for ice to travel the distance L_{glac} is inversely proportional to the speed u_{char} ; t_{flow} is also the time needed to sublimate the full ice thickness H_{char} at rate $-b_{char}$.

Equating these two time estimates,

$$t_{flow} = \frac{L_{glac}}{u_{char}} \frac{H_{char}}{-b_{char}} \quad (\text{A.2})$$

Solving Eq. A.2 for the penetration length L_{glac} in terms of the characteristic values,

$$L_{term} = -\frac{H_{char} u_{char}}{b_{char}} \quad (\text{A.3})$$

Eq. A.3 shows that penetration length L_{glac} is shorter when u_{char} is smaller (e.g. due to obstructions that impede ice flow along the bay), and when sublimation rate b_{char} is larger in magnitude (e.g. due to a warmer drier climate of the surrounding desert). Thickness H_{char} of the sea glacier on the adjacent ocean also matters; however, H_{char} is controlled by external factors beyond the narrow bay.

A characteristic steady-state thickness profile $h(x)$ can also be found. The volumetric flux $q(x)$ (m^3/s) is volume of incompressible ice passing through a “gate” across the bay with area $W \times h(x)$ at each position x , given by

$$q(x) = u_{char} W h(x), \quad (\text{A.4})$$

and the mass-conservation equation takes the form

$$\frac{dq}{dx} = W b_{char}. \quad (\text{A.5})$$

Putting Eq. A.4 into A.5 gives

$$\frac{dh}{dx} = \frac{b_{char}}{u_{char}}. \quad (\text{A.6})$$

Integrating Eq. A.6 with the boundary condition $h(0) = H_{char}$ yields a linear thickness profile

$$h(x) = H_{char} + \frac{b_{char}}{u_{char}} x, \quad (\text{A.7})$$

and the sea glacier terminates where $h=0$, i.e. at L_{term} given in Eq. A.3 above.

Examples with greater spatial variability, fewer assumptions, and additional physical details will be more complicated (e.g. see Campbell et al., 2011, 2014); however, this simple analytical solution can provide insights to guide refinements and approximations.

The existence of a refugium at the end of the bay requires $L_{glac} < L_{bay}$.

BIBLIOGRAPHY

- Dorian S. Abbot, Aiko Voigt, and Daniel Koll. The jormungand global climate state and implications for neoproterozoic glaciations. *Journal of Geophysical Research: Atmospheres*, 116(D18):D18103, 2011.
- Dorian S. Abbot, Aiko Voigt, Dawei Li, Guillaume Le Hir, Raymond T. Pierrehumbert, Mark Branson, David Pollard, and Daniel D. B. Koll. Robust elements of snowball earth atmospheric circulation and oases for life. *Journal of Geophysical Research: Atmospheres*, 118(12):6017–6027, 2013.
- Jordan T. Abell, Alex Pullen, Zachary J. Lebo, Paul Kapp, Lucas Gloege, Andrew R. Metcalf, Junsheng Nie, and Gisela Winckler. A wind-albedo-wind feedback driven by landscape evolution. *Nature Communications*, 2020a. doi: 10.1038/s41467-019-13661-w.
- Jordan T. Abell, Stefan R. Rahimi, Alex Pullen, Zachary J. Lebo, Dehai Zhang, Paul Kapp, Lucas Gloege, Sean Ridge, Junsheng Nie, and Gisela Winckler. A quantitative model-based assessment of stony desert landscape evolution in the hami basin, china: Implications for plio-pleistocene dust production in eastern asia. *Geophysical Research Letters*, 47(20):e2020GL090064, 2020b.
- Eric Agol, Caroline Dorn, Simon L. Grimm, Martin Turbet, Elsa Ducrot, Laetitia Delrez, Michaël Gillon, Brice-Olivier Demory, Artem Burdanov, Khalid Barkaoui, Zouhair Benkhaldoun, Emeline Bolmont, Adam Burgasser, Sean Carey, Julien de Wit, Daniel Fabrycky, Daniel Foreman-Mackey, Jonas Haldemann, David M. Hernandez, James Ingalls, Emmanuel Jehin, Zachary Langford, Jérémie Leconte, Susan M. Lederer, Rodrigo Luger, Renu Malhotra, Victoria S. Meadows, Brett M. Morris, Francisco J. Pozuelos, Didier Queloz, Sean N. Raymond, Franck Selsis, Marko Sestovic, Amaury H. M. J. Triaud, and Valerie Van Grootel. Refining the transit-timing and photometric analysis of

- trappist-1: Masses, radii, densities, dynamics, and ephemerides. *The Planetary Science Journal*, 2(1):1, jan 2021. doi: 10.3847/PSJ/abd022.
- V. K. Arora, A. Katavouta, R. G. Williams, C. D. Jones, V. Brovkin, P. Friedlingstein, J. Schwinger, L. Bopp, O. Boucher, P. Cadule, M. A. Chamberlain, J. R. Christian, C. Delire, R. A. Fisher, T. Hajima, T. Ilyina, E. Joetzjer, M. Kawamiya, C. D. Koven, J. P. Krasting, R. M. Law, D. M. Lawrence, A. Lenton, K. Lindsay, J. Pongratz, T. Raddatz, R. Séférian, K. Tachiiri, J. F. Tjiputra, A. Wiltshire, T. Wu, and T. Ziehn. Carbon-concentration and carbon-climate feedbacks in cmip6 models and their comparison to cmip5 models. *Biogeosciences*, 17(16):4173–4222, 2020. doi: 10.5194/bg-17-4173-2020. URL <https://bg.copernicus.org/articles/17/4173/2020/>.
- C. M. Bitz, K. M. Shell, P. R. Gent, D. A. Bailey, G. Danabasoglu, K. C. Armour, M. M. Holland, and J. T. Kiehl. Climate sensitivity in the community climate system model version 4. *J. Climate*, 25:3053–3070, 2012. doi: 10.1175/JCLI-D-11-00290.1.
- C.M. Bitz and W.H. Lipscomb. An energy-conserving thermodynamic model of sea ice. *Journal of Geophysical Research: Oceans*, 104(C7):15669–15677, 1999.
- Gordon Bonan. *Ecological Climatology: Concepts and Applications*. Cambridge University Press, 3 edition, 2015.
- Gordon B. Bonan, F. Stuart Chapin, and Starley L. Thompson. Boreal forest and tundra ecosystems as components of the climate system. *Climatic Change*, 29(2):145–167, 1995. doi: 10.1007/BF01094014.
- C. Braun, J. Hörner, A. Voigt, and J.G. Pinto. Ice-free tropical waterbelt for snowball earth events questioned by uncertain clouds. *Nature Geoscience*, 15(6):489–493, 2022.
- M.I. Budyko. The effect of solar radiation variations on the climate of the earth. *Tellus*, 21:611–619, 1969.
- C.E. Bøggild, R.E. Brandt, K.J. Brown, and S.G. Warren. The ablation zone in northeast greenland: ice types, albedos and impurities. *Journal of Glaciology*, 56(195):101–113, 2010.

- A.J. Campbell, E.D. Waddington, and S.G. Warren. Refugium for surface life on snowball earth in a nearly-enclosed sea? a first simple model for sea-glacier invasion. *Geophysical Research Letters*, 38(19):L19502, 2011. doi: 10.1029/2011GL048846.
- A.J. Campbell, E.D. Waddington, and S.G. Warren. Refugium for surface life on snowball earth in a nearly-enclosed sea? a numerical solution for sea-glacier invasion through a narrow strait. *J. Geophys. Res.*, 119:2679–2690, 2014. doi: 10.1002/2013JC009703.
- R. D. Cess, G. L. Potter, J. P. Blanchet, G. J. Boer, A. D. Del Genio, M. Déqué, V. Dymnikov, V. Galin, W. L. Gates, S. J. Ghan, J. T. Kiehl, A. A. Lacis, H. Le Treut, Z.-X. Li, X.-Z. Liang, B. J. McAvaney, V. P. Meleshko, J. F. B. Mitchell, J.-J. Morcrette, D. A. Randall, L. Rikus, E. Roeckner, J. F. Royer, U. Schlese, D. A. Sheinin, A. Slingo, A. P. Sokolov, K. E. Taylor, W. M. Washington, R. T. Wetherald, I. Yagai, and M.-H. Zhang. Intercomparison and interpretation of climate feedback processes in 19 atmospheric general circulation models. *Journal of Geophysical Research: Atmospheres*, 95(D10):16601–16615, 1990.
- A.J. Conley, J.-F. Lamarque, F. Vitt, W.D. Collins, and J. Kiehl. Port, a cesm tool for the diagnosis of radiative forcing. *Geoscientific Model Development*, 6(2):469–476, 2013. doi: 10.5194/gmd-6-469-2013.
- T.J. Crowley and S.K. Baum. Effect of decreased solar luminosity on late precambrian ice extent. *Journal of Geophysical Research: Atmospheres*, 98(D9):16723–16732, 1993.
- R. Dadic, P.C. Mullen, M. Schneebeli, R.E. Brandt, and S.G. Warren. Effects of bubbles, cracks, and volcanic tephra on the spectral albedo of bare ice near the transantarctic mountains: Implications for sea glaciers on snowball earth. *Journal of Geophysical Research: Earth Surface*, 118(3):1658–1676, 2013.
- G. Danabasoglu, J.-F. Lamarque, J. Bacmeister, D. A. Bailey, A. K. DuVivier, J. Edwards, L. K. Emmons, J. Fasullo, R. Garcia, A. Gettelman, C. Hannay, M. M. Holland, W. G. Large, P. H. Lauritzen, D. M. Lawrence, J. T. M. Lenaerts, K. Lindsay, W. H. Lipscomb, M. J. Mills, R. Neale, K. W. Oleson, B. Otto-Bliesner, A. S. Phillips, W. Sacks, S. Tilmes,

- L. van Kampenhout, M. Vertenstein, A. Bertini, J. Dennis, C. Deser, C. Fischer, B. Fox-Kemper, J. E. Kay, D. Kinnison, P. J. Kushner, V. E. Larson, M. C. Long, S. Mickelson, J. K. Moore, E. Nienhouse, L. Polvani, P. J. Rasch, and W. G. Strand. The community earth system model version 2 (cesm2). *Journal of Advances in Modeling Earth Systems*, 12(2):e2019MS001916, 2020. doi: 10.1029/2019MS001916.
- Y. Donnadieu, F. Fluteau, G. Ramstein, C. Ritz, and J. Besse. Is there a conflict between the neoproterozoic glacial deposits and the snowball earth interpretation: an improved understanding with numerical modeling. *Earth and Planetary Science Letters*, 208(1):101–112, 2003.
- K. Dorheim, S. Gering, R. Gieseke, C. Hartin, L. Pressburger, A. N. Shiklomanov, S. J. Smith, C. Tebaldi, D. Woodard, and B. Bond-Lamberty. Hector v3.1.1: functionality and performance of a reduced-complexity climate model. *EGUphere*, 2023:1–20, 2023. doi: 10.5194/egusphere-2023-1477.
- D.A.D. Evans. Stratigraphic, geochronological, and paleomagnetic constraints upon the neoproterozoic climatic paradox. *American Journal of Science*, 300(5):347–433, 2000.
- P. M. Forster, C. J. Smith, T. Walsh, W. F. Lamb, R. Lamboll, M. Hauser, A. Ribes, D. Rosen, N. Gillett, M. D. Palmer, J. Rogelj, K. von Schuckmann, S. I. Seneviratne, B. Trewin, X. Zhang, M. Allen, R. Andrew, A. Birt, A. Borger, T. Boyer, J. A. Broersma, L. Cheng, F. Dentener, P. Friedlingstein, J. M. Gutiérrez, J. Gütschow, B. Hall, M. Ishii, S. Jenkins, X. Lan, J.-Y. Lee, C. Morice, C. Kadow, J. Kennedy, R. Killick, J. C. Minx, V. Naik, G. P. Peters, A. Pirani, J. Pongratz, C.-F. Schleussner, S. Szopa, P. Thorne, R. Rohde, M. Rojas Corradi, D. Schumacher, R. Vose, K. Zickfeld, V. Masson-Delmotte, and P. Zhai. Indicators of global climate change 2022: annual update of large-scale indicators of the state of the climate system and human influence. *Earth System Science Data*, 15(6):2295–2327, 2023. doi: 10.5194/essd-15-2295-2023.
- P. Friedlingstein, R. M. Andrew, J. Rogelj, G. P. Peters, J. G. Canadell, R. Knutti, G. Luderer, M. R. Raupach, M. Schaeffer, D. P. van Vuuren, and C. Le Quéré. Persistent growth

of co₂ emissions and implications for reaching climate targets. *Nature Geoscience*, 7(10):709–715, 2014. doi: 10.1038/ngeo2248. URL <https://doi.org/10.1038/ngeo2248>.

P. Friedlingstein, M. W. Jones, M. O’Sullivan, R. M. Andrew, D. C. E. Bakker, J. Hauck, C. Le Quéré, G. P. Peters, W. Peters, J. Pongratz, S. Sitch, J. G. Canadell, P. Ciais, R. B. Jackson, S. R. Alin, P. Anthoni, N. R. Bates, M. Becker, N. Bellouin, L. Bopp, T. T. T. Chau, F. Chevallier, L. P. Chini, M. Cronin, K. I. Currie, B. Decharme, L. M. Djeutchouang, X. Dou, W. Evans, R. A. Feely, L. Feng, T. Gasser, D. Gilfillan, T. Gkritzalis, G. Grassi, L. Gregor, N. Gruber, Ö. Gürses, I. Harris, R. A. Houghton, G. C. Hurt, Y. Iida, T. Ilyina, I. T. Luijkx, A. Jain, S. D. Jones, E. Kato, D. Kennedy, K. Klein Goldewijk, J. Knauer, J. I. Korsbakken, A. Kötzinger, P. Landschützer, S. K. Lauvset, N. Lefèvre, S. Lienert, J. Liu, G. Marland, P. C. McGuire, J. R. Melton, D. R. Munro, J. E. M. S. Nabel, S.-I. Nakaoka, Y. Niwa, T. Ono, D. Pierrot, B. Poulter, G. Rehder, L. Resplandy, E. Robertson, C. Rödenbeck, T. M. Rosan, J. Schwinger, C. Schwingshakl, R. Séférian, A. J. Sutton, C. Sweeney, T. Tanhua, P. P. Tans, H. Tian, B. Tilbrook, F. Tubiello, G. R. van der Werf, N. Vuichard, C. Wada, R. Wanninkhof, A. J. Watson, D. Willis, A. J. Wiltshire, W. Yuan, C. Yue, X. Yue, S. Zaehle, and J. Zeng. Global carbon budget 2021. *Earth System Science Data*, 14(4):1917–2005, 2022. doi: 10.5194/essd-14-1917-2022.

J. Glen. The creep of polycrystalline ice. *Proc. R. Soc. A*, 228:519–538, 1955.

J.C. Goodman. Through thick and thin: Marine and meteoric ice in a "snowball earth" climate. *Geophysical Research Letters*, 33:L16701, 2006. doi: 10.1029/2006GL026840.

J.C. Goodman and R.T. Pierrehumbert. Glacial flow of floating marine ice in "snowball earth". *Geophys. Res. Oceans*, 108(C10):3308, 2003. doi: 10.1029/2002JC001471.

T.C. Grenfell, S.G. Warren, and P.C. Mullen. Reflection of solar radiation by the antarctic snow surface at ultraviolet, visible, and near-infrared wavelengths. *J. Geophys. Res.*, 99:18669–18684, 1994.

W.B. Harland. Critical evidence for a great infra-cambrian glaciation. *Geologische Rundschau*, 54(1):45–61, 1964.

C. A. Hartin, P. Patel, A. Schwarber, R. P. Link, and B. P. Bond-Lamberty. A simple object-oriented and open-source model for scientific and policy analyses of the global climate system – hector v1.0. *Geoscientific Model Development*, 8(4):939–955, 2015. doi: 10.5194/gmd-8-939-2015.

C. A. Hartin, B. Bond-Lamberty, P. Patel, and A. Mundra. Ocean acidification over the next three centuries using a simple global climate carbon-cycle model: projections and sensitivities. *Biogeosciences*, 13(15):4329–4342, 2016. doi: 10.5194/bg-13-4329-2016. URL <https://bg.copernicus.org/articles/13/4329/2016/>.

C. Hawkesworth, P.A. Cawood, and B. Dhuime. Rates of generation and growth of the continental crust. *Geoscience Frontiers*, 10:165–173, 2019.

O. Hoegh-Guldberg, D. Jacob, M. Taylor, M. Bindi, S. Brown, I. Camilloni, A. Diedhiou, R. Djalante, K.L. Ebi, F. Engelbrecht, J. Guiot, Y. Hijioka, S. Mehrotra, A. Payne, S.I. Seneviratne, R. Warren A. Thomas, and G. Zhou. *Impacts of 1.5°C Global Warming on Natural and Human Systems*, page 175–312. Cambridge University Press, 2018. doi: 10.1017/9781009157940.005.

Paul F. Hoffman, Dorian S. Abbot, Yosef Ashkenazy, Douglas I. Benn, Jochen J. Brocks, Phoebe A. Cohen, Grant M. Cox, Jessica R. Creveling, Yannick Donnadieu, Douglas H. Erwin, Ian J. Fairchild, David Ferreira, Jason C. Goodman, Galen P. Halverson, Malte F. Jansen, Guillaume Le Hir, Gordon D. Love, Francis A. Macdonald, Adam C. Maloof, Camille A. Partin, Gilles Ramstein, Brian E. J. Rose, Catherine V. Rose, Peter M. Sadler, Eli Tziperman, Aiko Voigt, and Stephen G. Warren. Snowball earth climate dynamics and cryogenian geology-geobiology. *Science Advances*, 3(11):e1600983, 2017. doi: 10.1126/sciadv.1600983.

P.F. Hoffman and D.P. Schrag. Snowball earth. *Scientific American*, 68(1):68–75, 2000.

- P.F. Hoffman and D.P. Schrag. The snowball earth hypothesis: Testing the limits of global change. *Terra Nova*, 14:129–155, 2002.
- S.R. Hudson, S.G. Warren, R.E. Brandt, Grenfell, T.C., and D. Six. Spectral bidirectional reflectance of antarctic snow: Measurements and parameterization. *Journal of Geophysical Research: Atmospheres*, 111:D18106, 2006. doi: 10.1029/2006JD007290.
- E. Hunke, W.H. Lipscomb, A. Turner, N. Jeffery, and S. Elliott. Cice: the los alamos sea ice model documentation and software user's manual la-cc-06-012. Technical report, Los Alamos National Laboratory, Los Alamos, New Mexico., 2015.
- J. Hörner and A. Voigt. Sea-ice thermodynamics can determine waterbelt scenarios for snowball earth. *EGUSphere*, 2023. doi: 10.5194/egusphere-2023-2073.
- IPCC. *Climate Change 2022: Mitigation of Climate Change. Contribution of Working Group III to the Sixth Assessment Report of the Intergovernmental Panel on Climate Change.* Cambridge University Press, Cambridge, UK and New York, NY, USA, 2022. doi: 10.1017/9781009157926. URL https://www.ipcc.ch/report/ar6/wg3/downloads/report/IPCC_AR6_WGIII_Full_Report.pdf.
- Chris D Jones and Pierre Friedlingstein. Quantifying process-level uncertainty contributions to tcrc and carbon budgets for meeting paris agreement climate targets. *Environmental Research Letters*, 15(7):074019, jun 2020. doi: 10.1088/1748-9326/ab858a. URL <https://dx.doi.org/10.1088/1748-9326/ab858a>.
- F. Joos, R. Roth, J. S. Fuglestvedt, G. P. Peters, I. G. Enting, W. von Bloh, V. Brovkin, E. J. Burke, M. Eby, N. R. Edwards, T. Friedrich, T. L. Frölicher, P. R. Halloran, P. B. Holden, C. Jones, T. Kleinen, F. T. Mackenzie, K. Matsumoto, M. Meinshausen, G.-K. Plattner, A. Reisinger, J. Segschneider, G. Shaffer, M. Steinacher, K. Strassmann, K. Tanaka, A. Timmermann, and A. J. Weaver. Carbon dioxide and climate impulse response functions for the computation of greenhouse gas metrics: a multi-model analysis. *Atmospheric Chemistry and Physics*, 13(5):2793–2825, 2013. doi: 10.5194/acp-13-2793-2013.

Fortunat Joos, Michele Bruno, Roger Fink, Ulrich Siegenthaler, Thomas F. Stocker, Corinne Le Quéré, and Jorge L. Sarmiento. An efficient and accurate representation of complex oceanic and biospheric models of anthropogenic carbon uptake. *Tellus B: Chemical and Physical Meteorology*, Jan 1996. doi: 10.3402/tellusb.v48i3.15921.

P. Kenrick, C.H. Wellman, H. Schneider, and G.D. Edgecombe. A timeline for terrestrialization: consequences for the carbon cycle in the palaeozoic. *Phil. Trans. Royal Soc. London*, B367(1588):519–536, 2012.

J. S. Kikstra, Z. R. J. Nicholls, C. J. Smith, J. Lewis, R. D. Lamboll, E. Byers, M. Sandstad, M. Meinshausen, M. J. Gidden, J. Rogelj, E. Kriegler, G. P. Peters, J. S. Fuglestvedt, R. B. Skeie, B. H. Samset, L. Wienpahl, D. P. van Vuuren, K.-I. van der Wijst, A. Al Khourdajie, P. M. Forster, A. Reisinger, R. Schaeffer, and K. Riahi. The ipcc sixth assessment report wgiii climate assessment of mitigation pathways: from emissions to global temperatures. *Geoscientific Model Development*, 15(24):9075–9109, 2022. doi: 10.5194/gmd-15-9075-2022. URL <https://gmd.copernicus.org/articles/15/9075/2022/>.

J.L. Kirschvink. Late proterozoic low-latitude global glaciation: the snowball earth. In J.W. Schopf and C. Klein, editors, *The Proterozoic Biosphere*, pages 51–52. Cambridge Univ. Press, New York, 1992.

A.H. Knoll. The multiple origins of complex multicellularity. *Annual Review of Earth and Planetary Sciences*, 39(1):217–239, 2011.

A.H. Knoll. Paleobiological perspectives on early eukaryotic evolution. *Cold Spring Harbor Perspectives in Biology*, 6(1):a016121, 2014.

C. D. Koven, V. K. Arora, P. Cadule, R. A. Fisher, C. D. Jones, D. M. Lawrence, J. Lewis, K. Lindsay, S. Mathesius, M. Meinshausen, M. Mills, Z. Nicholls, B. M. Sanderson, R. Séférian, N. C. Swart, W. R. Wieder, and K. Zickfeld. Multi-century dynamics of the climate and carbon cycle under both high and net negative emissions scenarios. *Earth System Dynamics*, 13(2):885–909, 2022. doi: 10.5194/esd-13-885-2022. URL <https://esd.copernicus.org/articles/13/885/2022/>.

Charles D Koven, Benjamin M Sanderson, and Abigail L S Swann. Much of zero emissions commitment occurs before reaching net zero emissions. *Environmental Research Letters*, 18(1):014017, jan 2023. doi: 10.1088/1748-9326/acab1a. URL <https://dx.doi.org/10.1088/1748-9326/acab1a>.

M.M. Laguë, G.B. Bonan, and A.L.S. Swann. Separating the impact of individual land surface properties on the terrestrial surface energy budget in both the coupled and uncoupled land–atmosphere system. *Journal of Climate*, 32(18):5725–5744, 2019.

M.M. Laguë, G.R. Quetin, S. Ragen, and W.R. Boos. Continental configuration controls the base-state water vapor greenhouse effect: lessons from half-land, half-water planets. *Climate Dynamics*, 2023. doi: 10.1007/s00382-023-06857-w.

X. Lan, P. Tans, and K.W. Thoning. Trends in globally-averaged co₂ determined from noaa global monitoring laboratory measurements version 2024-04. doi: 10.15138/9n0h-zh07. URL <https://gml.noaa.gov/ccgg/trends/global.html>.

N. J. Leach, S. Jenkins, Z. Nicholls, C. J. Smith, J. Lynch, M. Cain, T. Walsh, B. Wu, J. Tsutsui, and M. R. Allen. Fairv2.0.0: a generalized impulse response model for climate uncertainty and future scenario exploration. *Geoscientific Model Development*, 14(5): 3007–3036, 2021.

T.M. Lenton and S.J. Daines. Matworld – the biogeochemical effects of early life on land. *New Phytologist*, 215:531–537, 2017. doi: 10.1111/nph.14338.

A.J. Lewis, J.P. amd Weaver and M. Eby. Deglaciating the snowball earth: Sensitivity to surface albedo. *Geophysical Research Letters*, 33(23):L23604, 2006. doi: 10.1029/2006GL027774.

D. Li and R.T. Pierrehumbert. Sea glacier flow and dust transport on snowball earth. *Geophysical Research Letters*, 38(17):L17501, 2011.

P. Liu, Y. Liu, Y. Peng, J.-F. Lamarque, M. Wang, and Y. Hu. Large influence of dust on the precambrian climate. *Nature Communications*, 11(1):4427, 2020.

Y. Liu, W.R. Peltier, J. Yang, and G. Vettoretti. The initiation of neoproterozoic "snowball" climates in CCSM3: the influence of paleocontinental configuration. *Climate of the Past*, 9(6):2555–2577, 2013.

Y. Liu, W.R. Peltier, J. Yang, Vettoretti G., and Y. Wang. Strong effects of tropical ice-sheet coverage and thickness on the hard snowball earth bifurcation point. *Climate Dynamics*, 48(11):3459–3474, 2017.

Y. Liu, W.R. Peltier, J. Yang, and Y. Hu. Influence of surface topography on the critical carbon dioxide level required for the formation of a modern snowball earth. *Journal of Climate*, 31(20):8463–8479, 2018.

Y. Liu, P. Liu, D. Li, Y. Peng, and Y. Hu. Influence of dust on the initiation of neoproterozoic snowball earth events. *Journal of Climate*, 34(16):6673–6689, 2021.

James E. Lovelock. Geophysiology: A new look at earth science. *Bulletin of the American Meteorological Society*, 67(4):392–397, 1986. ISSN 00030007, 15200477.

Francis A. Macdonald, Mark D. Schmitz, James L. Crowley, Charles F. Roots, David S. Jones, Adam C. Maloof, Justin V. Strauss, Phoebe A. Cohen, David T. Johnston, and Daniel P. Schrag. Calibrating the cryogenian. *Science*, 327(5970):1241–1243, 2010.

A. H. MacDougall, T. L. Frölicher, C. D. Jones, J. Rogelj, H. D. Matthews, K. Zickfeld, V. K. Arora, N. J. Barrett, V. Brovkin, F. A. Burger, M. Eby, A. V. Eliseev, T. Hajima, P. B. Holden, A. Jeltsch-Thömmes, C. Koven, N. Mengis, L. Menzel, M. Michou, I. I. Mokhov, A. Oka, J. Schwinger, R. Séférian, G. Shaffer, A. Sokolov, K. Tachiiri, J. Tjiputra, A. Wiltshire, and T. Ziehn. Is there warming in the pipeline? a multi-model analysis of the zero emissions commitment from CO₂. *Biogeosciences*, 17(11) : 2987 – –3016, 2020. doi : 10.5194/bg – 17 – 2987 – 2020. URL <https://bg.copernicus.org/articles/17/2987/2020/>.

Andrew H. MacDougall. The transient response to cumulative co₂ emissions: a review. *Current Climate Change Reports*, 2(1):39–47, 2016. doi: 10.1007/s40641-015-0030-6. URL <https://doi.org/10.1007/s40641-015-0030-6>.

C.P. McKay. Thickness of tropical ice and photosynthesis on a snowball earth. *Geophysical Research Letters*, 27(14):2153–2156, 2000.

M. Meinshausen, S. C. B. Raper, and T. M. L. Wigley. Emulating coupled atmosphere-ocean and carbon cycle models with a simpler model, magicc6 – part 1: Model description and calibration. *Atmospheric Chemistry and Physics*, 11(4):1417–1456, 2011. doi: 10.5194/acp-11-1417-2011.

Andrew S. Merdith, Simon E. Williams, Alan S. Collins, Michael G. Tetley, Jacob A. Mulder, Morgan L. Blades, Alexander Young, Sheree E. Armistead, John Cannon, Sabin Zahirovic, and R. Dietmar Müller. Extending full-plate tectonic models into deep time: Linking the neoproterozoic and the phanerozoic. *Earth-Science Reviews*, 214:103477, 2021.

R. J. Millar, Z. R. Nicholls, P. Friedlingstein, and M. R. Allen. A modified impulse-response representation of the global near-surface air temperature and atmospheric concentration response to carbon dioxide emissions. *Atmospheric Chemistry and Physics*, 17(11):7213–7228, 2017.

Ross N. Mitchell, Thomas M. Gernon, Grant M. Cox, Adam R. Nordsvan, Uwe Kirscher, Chuang Xuan, Yebo Liu, Xu Liu, and Xiaofang He. Orbitally forced ice sheet fluctuations during the marinoan snowball earth glaciation. *Nature Geoscience*, 8(9):704–707, 2015.

J.L. Monteith. Evaporation and surface temperature. *Quart. J. Roy. Meteor. Soc*, 107:1–27, 1981.

Jennifer L. Morris, Mark N. Puttick, James W. Clark, Dianne Edwards, Paul Kenrick, Silvia Pressel, Charles H. Wellman, Ziheng Yang, Harald Schneider, and Philip C. J. Donoghue. The timescale of early land plant evolution. *Proc. Nat. Acad. Sci.*, 115(10):E2274–E2283, 2018. doi: 10.1073/pnas.1719588115.

R.B. Neale, J.H. Richter, A.J. Conley, S. Park, P.H. Lauritzen, D.L. Gettelman, A. Williamson, P. J. Rasch, S. J. Vavrus, M. A. Taylor, W. D. Collins, M. Zhang, and S.-J.

- Lin. Description of the ncar community atmosphere model (cam 4.0) (ncar/tn-485+str). Technical report, National Center for Atmospheric Research, Boulder, Colorado, 2010.
- J. F. Nye. The flow of a glacier in a channel of rectangular, elliptical or parabolic cross-section. *J. Glaciol.*, 5:661–690, 1965.
- Sofia Palazzo Corner, Martin Siegert, Paulo Ceppi, Baylor Fox-Kemper, Thomas L. Frölicher, Angela Gallego-Sala, Joanna Haigh, Gabriele C. Hegerl, Chris D. Jones, Reto Knutti, Charles D. Koven, Andrew H. MacDougall, Malte Meinshausen, Zebedee Nicholls, Jean Baptiste Sallée, Benjamin M. Sanderson, Roland Séférian, Merritt Turetsky, Richard G. Williams, Sönke Zaehle, and Joeri Rogelj. The zero emissions commitment and climate stabilization. *Frontiers in Science*, 1, 2023. ISSN 2813-6330. doi: 10.3389/fsci.2023.1170744. URL <https://www.frontiersin.org/journals/science/articles/10.3389/fsci.2023.1170744>.
- H.L. Penman. Natural evaporation from open water, bare soil and grass. *Proc. Roy. Soc. London*, 193A:120–145, 1948.
- R. T. Pierrehumbert. Climate dynamics of a hard snowball earth. *J. Geophys. Res. Atmos.*, 110(D01111), 2005. doi: 10.1029/2004JD005162.
- D. Pollard and J.F. Kasting. Climate-ice sheet simulations of neoproterozoic glaciation before and after collapse to snowball earth. In Christopher P. McKay, Mark A.S. McMenamin, Linda Sohl, and Gregory S. Jenkins, editors, *The Extreme Proterozoic: Geology, Geochemistry, and Climate, Geophys. Monogr. Ser.*, vol. 146, pages 91–105. AGU, Washington, D.C., 2004.
- D. Pollard and J.F. Kasting. Snowball earth: A thin-ice solution with flowing sea glaciers. *J. Geophys. Res.*, 110(C07010), 2005. doi: 10.1029/2004JC002525.
- D. Pollard, J.F. Kasting, and M.E. Zugger. Snowball earth: Asynchronous coupling of sea-glacier flow with a global climate model. *J. Geophys. Res. Atmos.*, 122(5157-5171), 2017. doi: 10.1002/2017JD026621.

S.M. Porter. The fossil record of early eukaryotic diversification. *The Paleontological Society Papers*, 10:35–50, 2004.

G.J. Retallack. Neoproterozoic snowball earth extent inferred from paleosols in California. *J. Palaeosciences*, 72:9–28, 2023. doi: 10.54991/jop.2023.1851.

Joeri Rogelj, Piers M. Forster, Elmar Kriegler, Christopher J. Smith, and Roland Séférian. Estimating and tracking the remaining carbon budget for stringent climate targets. *Nature*, 571(7765):335–342, 2019. doi: 10.1038/s41586-019-1368-z. URL <https://doi.org/10.1038/s41586-019-1368-z>.

B. Sanderson. The role of prior assumptions in carbon budget calculations. *Earth System Dynamics*, 11(2):563–577, 2020. doi: 10.5194/esd-11-563-2020. URL <https://esd.copernicus.org/articles/11/563/2020/>.

T. J. O. Sanderson. Equilibrium profile of ice shelves. *J. Glaciol.*, 22:435–460, 1979.

J. Scheff and D.M.W. Frierson. Scaling potential evapotranspiration with greenhouse warming. *Journal of Climate*, 27(4):1539–1558, 2014.

D.P. Schrag, R.A. Berner, P.F. Hoffman, and G.P. Halverson. On the initiation of a snowball earth. *Geochemistry, Geophysics, Geosystems*, 3(6):1–21, 2002. doi: 10.1029/2001GC000219.

S.A. Sejas, P.C. Taylor, and M. Cai. Unmasking the negative greenhouse effect over the antarctic plateau. *npj Climate and Atmospheric Science*, 1(17), 2018.

W.D. Sellers. A global climatic model based on the energy balance of the earth-atmosphere system. *Journal of Applied Meteorology and Climatology*, 8(3):392–400, 1969.

Denis E. Sergeev, Thomas J. Fauchez, Martin Turbet, Ian A. Boutle, Kostas Tsigaridis, Michael J. Way, Eric T. Wolf, Shawn D. Domagal-Goldman, François Forget, Jacob Haqq-Misra, Ravi K. Kopparapu, F. Hugo Lambert, James Manners, and Nathan J. Mayne. The trappist-1 habitable atmosphere intercomparison (thai). ii. moist cases—the two wa-

- terworlds. *The Planetary Science Journal*, 3(9):212, sep 2022. doi: 10.3847/PSJ/ac6cf2.
URL <https://dx.doi.org/10.3847/PSJ/ac6cf2>.
- Greta E. M. Shum, Marysa M. Laguë, Stephanie S. Rushley, and Abigail L. S. Swann. Beautiful days in the neighborhood: Land–atmosphere interactions as drivers of forest expansion. *Earth Interactions*, 27(1):e220017, 2023. doi: 10.1175/EI-D-22-0017.1.
- M. Siddall, D. Smeed, S. Matthiesen, and E. Rohling. Modelling the seasonal cycle of the exchange flow in bab el mandab (red sea). *Deep Sea Research Part I*, 49(9):1551–1569, 2002.
- C. J. Smith, P. M. Forster, M. Allen, N. Leach, R. J. Millar, G. A. Passerello, and L. A. Regayre. Fair v1.3: a simple emissions-based impulse response and carbon cycle model. *Geoscientific Model Development*, 11(6):2273–2297, 2018.
- E.A. Smith. The structure of the arabian heat low. part i: Surface energy budget. *Monthly Weather Review*, 114(6):1067–1083, 1986.
- Abigail L. Swann, Inez Y. Fung, Samuel Levis, Gordon B. Bonan, and Scott C. Doney. Changes in arctic vegetation amplify high-latitude warming through the greenhouse effect. *Proceedings of the National Academy of Sciences*, 107(4):1295–1300, 2010. doi: 10.1073/pnas.0913846107.
- Abigail Lynn Segal Swann. *Ecoclimate: Variations, Interactions, and Teleconnections*. eScholarship, University of California, 2010.
- R. H. Thomas. The creep of ice shelves: Theory. *J. Glaciol.*, 12:45–53, 1973.
- J. R. Toggweiler. Variation of atmospheric co₂ by ventilation of the ocean’s deepest water. *Paleoceanography*, 14(5):571–588, 1999. doi: 10.1029/1999PA900033.
- W.F. Vincent and C. Howard-Williams. Life on snowball earth. *Science*, 287(5462):2421–2421, 2000.

- W.F. Vincent, J.A.E. Gibson, R. Pienitz, V. Villeneuve, P.A. Broady, P.B. Hamilton, and C. Howard-Williams. Ice shelf microbial ecosystems in the high arctic and implications for life on snowball earth. *Naturwissenschaften*, 87(3):137–141, 2000.
- A. Voigt and D.S. Abbot. Sea-ice dynamics strongly promote snowball earth initiation and destabilize tropical sea-ice margins. *Climate of the Past*, 8(6):2079–2092, 2012.
- A. Voigt and J. Marotzke. The transition from the present-day climate to a modern snowball earth. *Climate Dynamics*, 35(5):887–905, 2010.
- A. Walsh, T. Ball, and D.M. Schultz. Extreme sensitivity in snowball earth formation to mountains on paleoproterozoic supercontinents. *Scientific Reports*, 9(1):2349, 2019.
- S.G. Warren and R.E. Brandt. Comment on “snowball earth: A thin-ice solution with flowing sea glaciers” by david pollard and james f. kasting. *Journal of Geophysical Research*, 111(C09016), 2006.
- S.G. Warren, R.E. Brandt, T.C. Grenfell, and C.P. McKay. Snowball earth: Ice thickness on the tropical ocean. *J. Geophys. Res.*, 107(C10):3167, 2002.
- Andrew J. Watson and James E. Lovelock. Biological homeostasis of the global environment: the parable of daisyworld. *Tellus B*, 35B(4):284–289, 1983. doi: <https://doi.org/10.1111/j.1600-0889.1983.tb00031.x>.
- William R Wieder, Cory C Cleveland, David M Lawrence, and Gordon B Bonan. Effects of model structural uncertainty on carbon cycle projections: biological nitrogen fixation as a case study. *Environmental Research Letters*, 10(4):044016, apr 2015.
- Eric T. Wolf. Assessing the habitability of the trappist-1 system using a 3d climate model. *The Astrophysical Journal Letters*, 839(1):L1, apr 2017. doi: 10.3847/2041-8213/aa693a. URL <https://dx.doi.org/10.3847/2041-8213/aa693a>.
- Andrew J. Wood, Graeme J. Ackland, James G. Dyke, Hywel T. P. Williams, and Timothy M. Lenton. Daisyworld: A review. *Reviews of Geophysics*, 46(1), 2008. doi: <https://doi.org/10.1029/2006RG000217>.

J. Yang, W.R. Peltier, and Y. Hu. The initiation of modern soft and hard snowball earth climates in CCSM4. *Climate of the Past*, 8(3):907–918, 2012.